ANTENNA ELEMENT PATTERN RECONFIGURABILITY IN ADAPTIVE ARRAYS

BY

TYRONE LAVONNE ROACH

DISSERTATION

Submitted in partial fulfillment of the requirements
for the degree of Doctor of Philosophy in Electrical and Computer Engineering
in the Graduate College of the
University of Illinois at Urbana-Champaign, 2010

Urbana, Illinois

Doctoral Committee:

Professor Jennifer T. Bernhard, Chair
Professor Andreas C. Cangellaris
Professor José E. Schutt-Ainé
Professor Michael L. Oelze

ABSTRACT

This dissertation investigates the functional benefits of utilizing radiation reconfigurable antennas in an adaptive array setting. The work centers on arrays composed of a small number of widely spaced elements. Such array configurations (1) mitigate the effects of mutual coupling between reconfigurable elements, thereby maximizing their individual performance potential, and (2) establish a platform for applications seeking portability and requiring a small system package as a design priority. One aspect of the research extends the early work of R.T. Compton Jr. and others in adaptive arrays by going beyond utilizing ideal, traditional, fixed-pattern antenna element patterns to include element patterns more relevant to pattern reconfigurable antennas. The results demonstrate that a practical pattern reconfigurable element can produce results comparable to that of the ideal element and maintain good adaptive array performance in terms of output signal-to-interference-noise ratio (SINR).

Detailed analysis presents the limitations of Compton's approach, which only specifies the requirements of the additional reconfigurable element based on the original set of two elements in the array. This research overcomes these limitations by fully leveraging the capabilities of the available pattern reconfigurability. Therefore, using a systematic approach, the work integrates pattern variability directly into two different optimization routines, a convex and least mean square technique. The methodology expands the available solutions by allowing the algorithm itself to determine the range of possible antennas states. The developed framework incorporates an antenna pattern model with beam tilting characteristics, which is incorporated in each routine. The advantages and disadvantages of both methods are discussed in terms of pattern variability implementation through a number of adaptive array scenarios. Results establish a roadmap for the specification of pattern reconfigurable antenna capability that promises to improve small adaptive array performance. In particular, the research shows that designers should focus on an element's null steering capability rather than beam tilting capacity.

The journey of a thousand miles begins with the first step—even a slow walker will arrive.

ACKNOWLEDGMENTS

I would like to thank many people for their tremendous support, which has allowed me to reach this point in my life. Reaching this milestone has been a rewarding and humbling experience; what makes it even more special is the fact that it encompasses so many people who were there to help me along the way. Along this path, I have had the opportunity to meet so many gracious people who were true supporters and kept me going on a day-to-day basis. Thanks to all who have had a positive impact on my life. If I could reach out and personally thank each and every one of you, I would (I might end up trying to do so before it is all said and done).

A heartfelt thanks goes to my entire family, including my lovely and hardworking mother and father, my two wonderful big sisters, and my not-so-little-anymore nephew. To all my cousins who have always looked out for me and my uncles and aunts who have treated me like their own, thank you. The closeness and love our entire family breeds has given me the desire to pursue the goals I set forth.

I want to acknowledge the extraordinary amount of support from my advisor Jennifer Bernhard. I thank her for taking me under her guidance and offering me the kindness, patience, and mentorship over the years necessary to achieve my goals. I would like also thank my committee members Andreas Cangellaris, José Schutt-Ainé, and Michael Oelze for their guidance and invaluable insight. I would like to express my appreciation to Kathleen Melde and her colleagues for hosting me at the University of Arizona and sharing their thoughts on my work. It has also been a pleasure to share my time with my research group members, those of the past and the present. In many ways the group is like a family itself; they make the environment warm and fun. Having them around to share ideas and the laughter has been a once-in-a-lifetime experience. I also want to express my appreciation to all the wonderful people I have come to know within the Electromagnetics Laboratory, ECE department, and the University of Illinois at Urbana-Champaign. A number of lifetime friendships have been gained, for example, my "big brother" Jaime Alanis and the one-and-only Mister Jack.

To all my close friends back home from high school to my undergraduate years, thank you for your encouragement and all your support when I go back home to visit. I

must also pay homage to all my friends, co-workers, professors, and advisors from the Luxor Hotel and Casino, College of Southern Nevada, University of Nevada-Las Vegas, Environmental Protection Agency, and the various summer research/intern programs. They have had an impact on my life in more ways than you can imagine. The experience and encouragement I received during these stages of my life has opened the door of opportunity. Finally, I would like to acknowledge the agencies that have allowed me to pursue my research interests as a graduate student. These include the SURGE, DFI, GEM, and Vodafone-Illinois graduate fellowship programs and the various forms of support by the ECE department and MEP program at the University of Illinois at Urbana-Champaign.

TABLE OF CONTENTS

LIST OF FIGURES

LIST OF TABLES

CHAPTER 1
INTRODUCTION

1.1 Background

Early work and activity in phased array technology began in earnest in the 1940s, and a large literature exists on phased arrays from various perspectives. For example, the author in [1] provides a comprehensive discussion of all aspects of phased arrays, while [2] offers a collection of design data for radar and communication systems. Furthermore, in [3], the basics of antenna array theory are outlined with attention on pattern analysis and synthesis for periodic linear and planar arrays. In contrast, the author in [4] considers the array as a processor and thus analyzes a variety of characteristics from a signal processing perspective. Simply put, utilizing multiple *in situ* elements with variable magnitude, phase- or time-delay control at each element has had an enormous impact on wireless communications. The technology has developed from diverse military applications, but currently addresses a growing list of commercial requirements [5] as well, i.e., those desiring additional flexibility in more sophisticated radar and communications systems [6,7,8].

Traditional phased arrays typically incorporate antenna elements with identical, fixed characteristics. This in turn may be one of the factors that limit phased arrays from meeting the increasing demands posed by future wireless communications systems. Reconfigurable antennas, on the other hand, offer dynamic behavior by being able to modify one or more of their fundamental operating characteristics (e.g., pattern, frequency, and polarization) via electrical, mechanical, or other means [9]. As a result, pattern reconfigurable antennas—the focus of this dissertation—along with other reconfigurable antenna types, possess an added degree of freedom that may enhance or expand system performance when incorporated into phased arrays. Prior investigation, for example [10,11,12,13,14], has begun to examine the capabilities of pattern reconfigurable antennas with beam tilts. However, questions still remain about the true benefits these antennas can offer in an array setting. Therefore, the research presented in

this dissertation continues to explore the capabilities and limitations of radiation reconfigurable antennas in phased arrays—in particular, phased arrays utilized in the context of an adaptive array platform.

Adaptive antenna systems (e.g., self-adjusting, self-phasing) date back to the 1950s. Early advances in this field were well documented in a special issue of the *IEEE Transactions on Antennas and Propagation* for March 1964 [15] and subsequently another special issue for September 1976 [16]. In general, an adaptive array antenna system controls its pattern in response to the signal environment [17]. Such systems seek to automatically sense and suppress the presence of interference noise sources (friendly or hostile) while simultaneously enhancing desired signal reception without prior knowledge of the signal environment. Therefore, they offer more flexibility, reliability, and improved reception performance compared to those of conventional arrays [18].

1.2 Research Overview

As discussed in [9], one of the key requirements for pattern reconfigurable antennas is to maintain their frequency characteristics over the parameter of reconfiguration. In an array setting composed of closely spaced elements, mutual coupling usually diminishes element performance from its single-element behavior—an effect typically predicated upon the antenna's highly resonant nature. Thus, this research's focus includes utilizing radiation reconfigurable antennas not only with relatively large element spacing but also with a small number of antenna elements in the adaptive array. Employing relatively wide (or large) element spacing can positively impact performance by diminishing the effects of mutual coupling and allowing additional space between array elements for supplementary RF electronics (e.g., biasing networks, etc.). Likewise, a system package containing an adaptive array composed of a small number of pattern reconfigurable antenna elements could provide major benefits in military applications requiring a small footprint (minimal size and low weight for portability) while providing a tactical edge on the battlefield—a necessity in the Network Centric Warfare model [19]. Overall, the combination of wider element spacing with a

small number of array elements simplifies the design space and reduces the need for additional hardware.

The foundation of this research originates from early work in adaptive arrays spearheaded by R.T. Compton Jr. In [20], he develops an adaptive array technique that allows for relatively wide spacing between antenna elements while maintaining good performance. This aspect of having greater separation between reconfigurable antenna elements mitigates the effects of mutual coupling and falls well within the main objectives of the research. However, in adaptive arrays, wider element spacing introduces the undesired effect of "grating nulls," spurious nulls that degrade overall system performance. The work presented in [21] discusses the circumstances behind grating nulls and methods to mitigate them in a linear array comprised of antenna elements with unequal element patterns.

Pattern reconfigurable antennas offer the potential to improve performance in adaptive arrays since their fundamental capability satisfies the criteria needed to mitigate grating nulls: element pattern reconfigurability. The work presented in [20] indicates that grating null effects can be mitigated by using unequal element patterns. However, the work uses ideal, traditional, fixed-pattern antennas with artificial beam tilts. From a practical perspective, pattern reconfigurable antennas have an advantage since they can reconfigure their beam maximum in accordance to what the adaptive array requires to maintain and/or improve system performance. Therefore, one aspect of this dissertation goes beyond utilizing ideal element patterns and employs procedures that incorporate element patterns more relevant to pattern reconfigurable antennas. The results illustrate the functional benefits of utilizing radiation reconfigurable antennas in an adaptive array setting.

Another aspect of the research draws on the shortcomings of the aforementioned approach, which specifies the requirements for the additional reconfigurable element. The requirements are based on the original set of array elements, which in turn do not fully leverage the capabilities of the available pattern reconfigurability. Thus the work presented in this dissertation reveals how to overcome this limitation in the following ways: (1) utilizing radiation reconfigurable antennas in an adaptive array setting not only

in terms of their beam tilting capability but their null-forming ability as well, and (2) determining the characteristics of the reconfigurable element patterns in a reverse fashion by integrating pattern variability into an adaptive algorithm. This method presents a more systematic approach in which the algorithm itself then determines the range of possible solutions.

The algorithm approach consists of adopting two optimization routines, a convex optimization routine developed in [22,23] and the least mean square (LMS) algorithm (a commonly used method in adaptive arrays [17]). Each routine differs by the array pattern objectives they seek to satisfy. The convex routine aspires to minimize sidelobe levels across the spatial range, while the LMS approach aims to directly satisfy the requirements of the signal environment. Due to the flexibility of the optimization methods, the present work develops an antenna pattern model with beam tilting characteristics that are incorporated in each routine. The advantages and disadvantages of both will be demonstrated in terms of pattern variability implementation. Even though the convex routine gives great insight into the model's implementation, it turns out its objectives over-constrain the problem and do not meet the desired performance results.

However, the LMS approach does not over-constrain the minimization problem, and thus this research utilizes the LMS algorithm for further analysis and evaluation. The performance evaluation is done in concert with a variety of qualifying adaptive array scenarios; here, the different scenarios provide the means to compare and contrast the results due to the varying parameters. Applying the pattern reconfigurable model, the results will bring to fruition the underlying objective of this research, which is to characterize the necessary elements of reconfigurability and demonstrate the impact pattern variability in adaptive arrays can have in wireless communications.

This research establishes a platform for applications seeking portable system designs containing a small number of antenna elements with relatively wide element spacing. By extending the early work of Compton in adaptive arrays by going beyond utilizing ideal antenna elements, the results of this research demonstrate that a practical pattern reconfigurable element can produce results comparable to that of the ideal element. After ascertaining the limitations brought on by this approach (e.g., not fully

utilizing the available reconfigurability), the procedure integrates pattern variability directly into an optimization routine—allowing the algorithm to fully leverage the capabilities of the available reconfigurability. The implementation of this approach is based on the development of a pattern reconfigurable element model that uses a two-element subarray topology in conjunction with the appropriate element weight constraints. As a result, this work establishes a pathway specifying the design requirements for pattern reconfigurable antennas to improve small adaptive array performance, demonstrating that designers should focus on an element's null steering capability rather than just its beam tilting capacity.

1.3 Dissertation Outline

This dissertation proceeds as follows: The first section of Chapter 2 first exemplifies two pattern reconfigurable antennas, designed by past researchers in the Electromagnetics Lab at the University of Illinois at Urbana-Champaign. The next section continues up with a brief investigation regarding the mutual coupling effects of these two pattern reconfigurable antennas in a small array setting. Next, Chapter 3 gives an overview of adaptive arrays and then discusses the analytical relationships used in this research. In addition to an alternate way to consider grating nulls, the chapter gives more detail behind the adopted technique. The last section in this chapter outlines the steps taken in the analysis to explore the functional benefits of utilizing pattern variability in adaptive arrays. Chapter 4 implements the technique and displays a number of graphical results related to several adaptive array scenarios, including those incorporating a practical pattern reconfigurable antenna element into the methodology. An analysis of the overall limitations of the approach follows.

Chapter 5 expands the potential use for radiation reconfigurable antennas by fully leveraging the capabilities of the available pattern reconfigurability. The chapter demonstrates that the advantages gained in pattern variability not only stem from the antenna's beam tilting capability but also from its null-forming ability through simple, but illustrative examples utilizing the adaptive array platform. Next, Chapter 6 follows along the task of fully leveraging the available reconfigurability and discusses a model

and method which integrates pattern variability into the algorithm, in this case the convex routine. This method presents a more systematic approach in which the algorithm itself then determines the range of possible solutions. The chapter includes the configuration details for each example operational scenario involved in the analysis, followed by graphical results pertaining to each scenario.

Making use of the knowledge gained from implementing the convex optimization routine, Chapter 7 utilizes the LMS technique with a solver that has more flexibility in terms of implementing the pattern reconfigurable model. Various qualifying adaptive array scenarios are analyzed using LMS. The different scenarios provide the means to compare and contrast the results due to the varying parameters. Evaluation of the individual element patterns will reveal the types of reconfigurability necessary to uphold the performance offered by adaptive arrays. Chapter 8 concludes the dissertation with a summary and directions for future work.

CHAPTER 2
EXAMPLE RECONFIGURABLE ANTENNAS AND MUTUAL COUPLING EFFECTS

2.1 Example Reconfigurable Designs

Since this dissertation's research centers on pattern reconfigurable antennas, this section provides further insight into the basic operation of pattern reconfigurable antennas. First, two example pattern reconfigurable antennas, designed by past researchers in the Electromagnetics Lab at the University of Illinois at Urbana-Champaign, are discussed. The first one is a broadside-to-endfire reconfigurable antenna (BERA), and the second one is reconfigurable microstrip parasitic array (RMPA). Each is explained briefly, with more in-depth discussion and analysis of the antennas found in [14,24] and [12,13], respectively.

2.1.1 Broadside-to-Endfire Reconfigurable Antenna (BERA)

The BERA operates as a bi-state, linearly polarized pattern reconfiguring radiator capable of switching its radiation patterns between a broadside (BS) state and an endfire (EF) state over a common impedance bandwidth. The broadside and endfire patterns are produced through switching elements located on the antenna structure. Figure 2-1 displays a layout of the antenna's design, including the location of the two switches.

In order to attain pattern reconfigurability, the inline switching elements alter the current distributions to produce the desired far-field pattern. In reference to Figure 2-1, with switch 1 closed and switch 2 open, the antenna operates in endfire mode. Conversely, with switch 1 open and switch 2 closed, the antenna operates in broadside mode. Figure 2-2 shows the resulting measured radiation patterns for both configuration states in the E_θ and E_ϕ polarizations. The broadside/endfire radiation characteristics of the antenna is shown in the antenna's primary polarization and plane of interest (E_θ and the $\phi = 0°$ plane, respectively). In this work, the switching elements are hardwired for

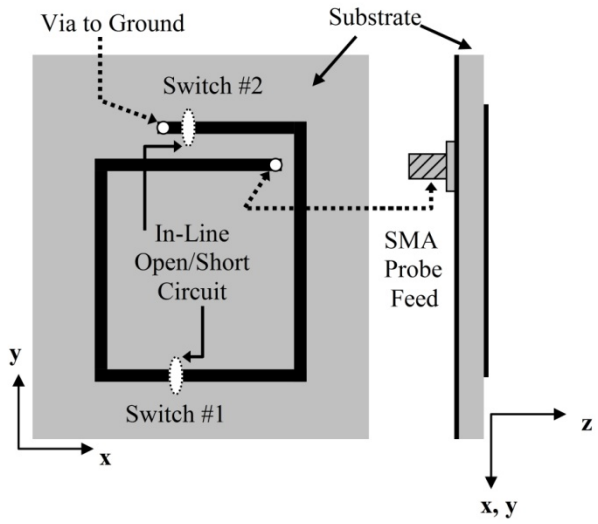

Figure 2-1: Reconfigurable antenna's physical layout including switch position [24].

proof of concept. The authors in [14] analyze the process of integrating RF MEMS (microelectromechanical systems) switches on the antenna; their experimental results show radiation characteristics similar to the switches being hardwired.

2.1.2 Reconfigurable Microstrip Parasitic Array (RMPA)

The RMPA, in its single-element form, consists of three parallel conducting strips (a probe fed center strip and two parasitics on both sides) set on a grounded dielectric substrate [12]. Each parasitic strip contains two gaps near the ends for switch placement. Figure 2-3 illustrates a physical layout of the antenna structure, including the location of the gaps for the switches. The linearly polarized antenna is capable of reconfiguring its radiation pattern in the *y*-*z* plane (the H-plane) in three different modes: RD, DD, and DR, where R and D stand for "reflector" and "director," respectively, in reference to the configuration of the two outer parasitic elements. Changing the electrical length of the parasitic elements via the switches creates the beam tilts.

The antenna operates similar to that of a Yagi-Uda antenna [25]. Leaving all gaps on the parasitic structure open configures the antenna in broadside mode (DD). Closing the two gaps on the left parasitic element in conjunction with opening the two gaps on the right parasitic element produces a tilted pattern toward the positive *y* axis (RD mode). Conversely, opening the two gaps on the left parasitic element while closing the two gaps

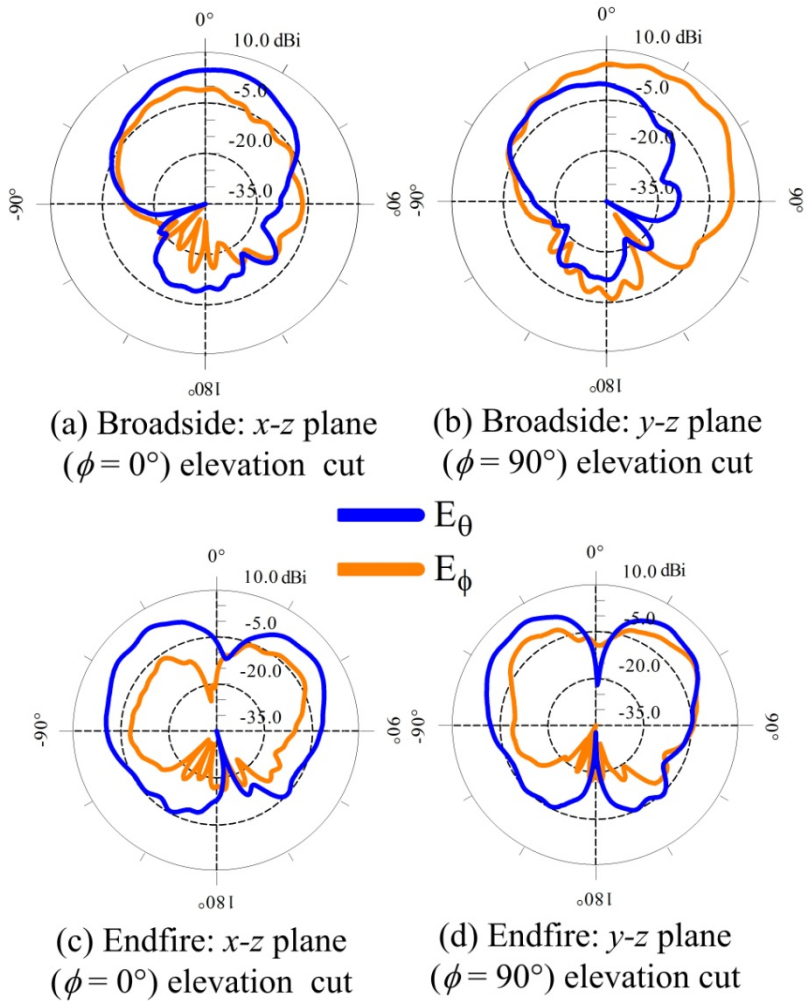

Figure 2-2: Radiation pattern of the reconfigurable antennas in the elevation planes for the two configuration states: (a) and (b) broadside mode, (c) and (d) endfire mode [14].

on the right parasitic element provides a tilted pattern toward the negative *y* axis (DR mode). All three pattern modes operate over a common impedance bandwidth.

Figure 2-4 shows a polar plot of the radiation patterns produced by the RMPA. The data traces represent the normalized magnitude co-polar electric field versus elevation angle (θ) for each of the three modes: a broadside pattern (DD mode), +25° tilted pattern (RD mode), and a –25° tilted pattern (DR mode). These particular radiation patterns result from using electromagnetic simulation software, utilizing the design parameters indicated in [12].

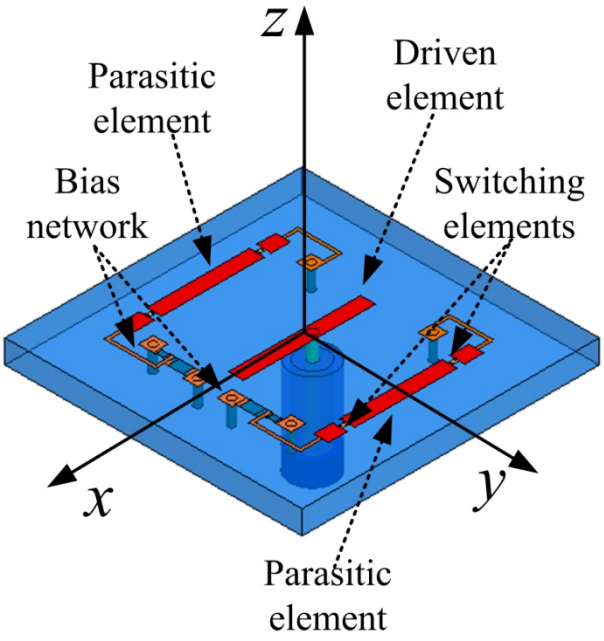

Figure 2-3: Layout of the reconfigurable microstrip parasitic array (RMPA). The antenna is capable of reconfiguring its radiation pattern in the *y*-*z* plane by means of the indicated switching elements [13].

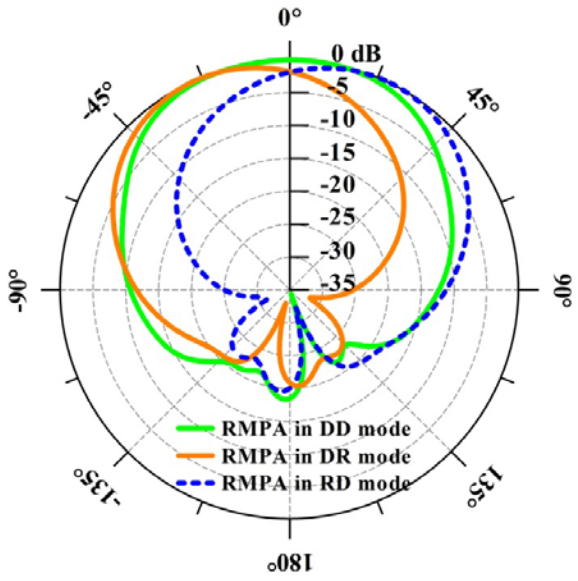

Figure 2-4: Normalized radiation patterns for the co-polar field (in dB) produced by a single RMPA element. The curves represent the DD mode (broadside), DR mode (−25° tilt), and RD mode (+25° tilt).

2.2 Mutual Coupling Analysis

These pattern reconfigurable antennas operate under highly resonant conditions, and, as a result, their performance can suffer in an array setting with large amounts of mutual coupling, an effect primarily due to element proximity. Given that one aspect of this research centers on implementing a small number of pattern reconfigurable elements in a linear array with relatively wide elemental spacing to help mitigate mutual coupling, it is instructive to evaluate these effects for the elements discussed in the previous chapter.

In order to illustrate the effects of mutual coupling on the two model antennas, each is placed in a uniform, linear, equally spaced array composed of two elements spaced a distance d_2 apart. Figure 2-5 displays an example array setup composed of BERAs (left graphic) and RMPAs (right graphic). Since the transmission coefficients, i.e., S_{ij} ($i \neq j$) parameters, give a good indication of the amount of mutual coupling between array elements, Ansoft Corporation's HFSS [26] is used to simulate the two-element array and calculate S_{21} for a range of element spacing: $0.6\lambda_0 \leq d_2 \leq 2.0\lambda_0$, where λ_0 is the free space wavelength at an operational frequency of 5.8 GHz. Note, both antenna designs have been scaled from their nominal base frequency design to operate at the wireless local area network (WLAN) band of 5.8 GHz, and the overall operational behavior of each individual antenna remains the same. Figure 2-6 displays the S_{21} results.

As seen in Figure 2-6, the simulation results show the spacing effects for the two-element array for all reconfigurable modes (uniform mode combinations only, no mixed-mode scenarios). Mutual coupling plays a more significant role for smaller element spacing. For element spacing in this range, the variations in S_{21} are more pronounced, showing the highest values in some cases. At the smallest spacing, the RMPA in DD mode has the highest coupling, while another mode of configuration, DR, has the least. Note, the RMPA in the RD mode is not shown because it matches that of the DR mode due to symmetry. Nevertheless, as the spacing increases, the curves stabilize and decrease in S_{21}. This indicates more isolation between the elements, and, as a result, the

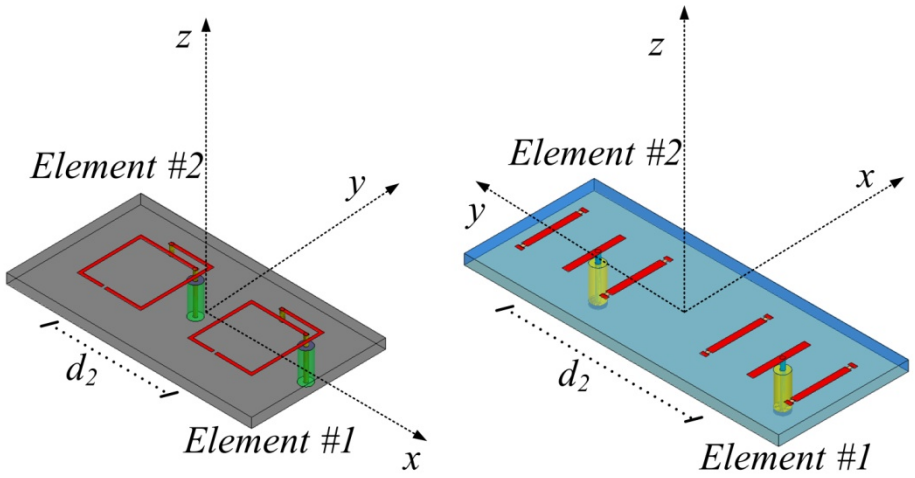

Figure 2-5: Example array setup for the 2-element array mutual coupling analysis. In the graph on the left, the array is composed of two BERA elements, while the array on the right is composed of two RMPA elements. The graph shows the relative position of the elements and d_2, the spacing between them.

antenna's operating characteristics will tend to more closely match their single-element behavior.

While Figure 2-6 captures mutual coupling effects via the S_{21} parameters, it does not indicate what effect coupling has on the individual element patterns. Consider the RMPA element in its DR and DD mode configurations, a scenario that would require switching the element patterns from a –25° tilt to a 0° tilt, respectively. Figure 2-7 shows a combination of simulated co-polar radiation patterns for two-element spacings: $d_2 = 0.6\lambda_0$ and $d_2 = 2.0\lambda_0$, for both the DR mode and DD mode configurations. Within each of the four plots are three curves: the radiation pattern of the single element by itself (dark curve), the active element pattern (AEP) of antenna element 1 in the two-element array scenario (dotted curve), and the AEP of antenna element 2 in the two-element array scenario (gray curve). Recall, the AEP of an array element means that particular antenna is actively fed, while all others are terminated in a matched load. Cases (a) and (b) represent the RMPA in DR mode with $d_2 = 0.6\lambda_0$ in (a) and $d_2 = 2.0\lambda_0$ in (b). Likewise, cases (c) and (d) represent the RMPA in DD mode with $d_2 = 0.6\lambda_0$ in (c) and $d_2 = 2.0\lambda_0$ in (d).

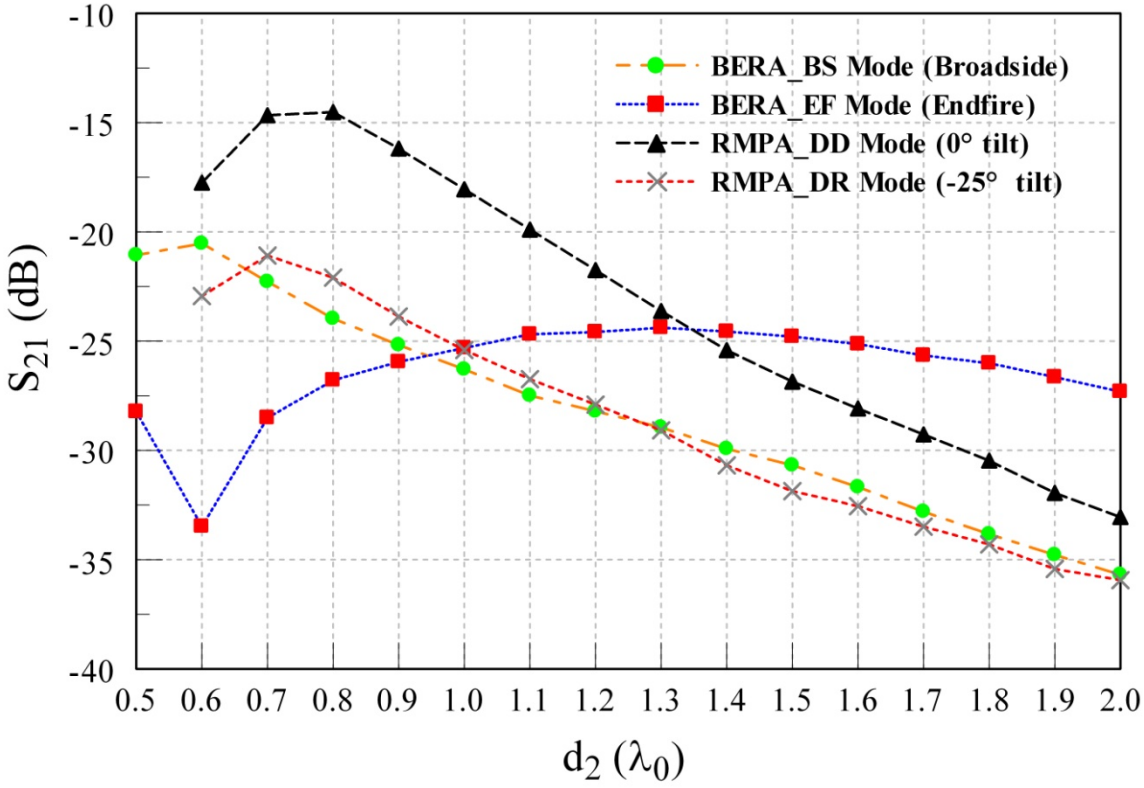

Figure 2-6: S_{21} (dB) vs. element separation d_2 (λ_0) for a 2-element array composed of identical pattern reconfigurable elements. The curves are plotted at the center frequency of operation of 5.8 GHz.

The results in Figure 2-7 illustrate how mutual coupling can affect the individual antenna elements in the array. In case (a), the AEP of element 1 tends to follow the single element, but mutual coupling effects distort the AEP of element 2, to the extent that it is radiating in a broadside mode rather than in a tilted mode. However, for wider element spacing, as in case (b), the AEP of element 2 returns to its tilted form. The effects are even more pronounced for the DD mode scenario. In case (c), mutual coupling effects distort both AEPs 1 and 2; both patterns seem to tilt away from their single-element form. On the other hand, increasing the element spacing to $d_2 = 2.0\lambda_0$, (case (d)), brings both patterns back to a broadside radiation pattern, thereby mitigating the effects of mutual coupling.

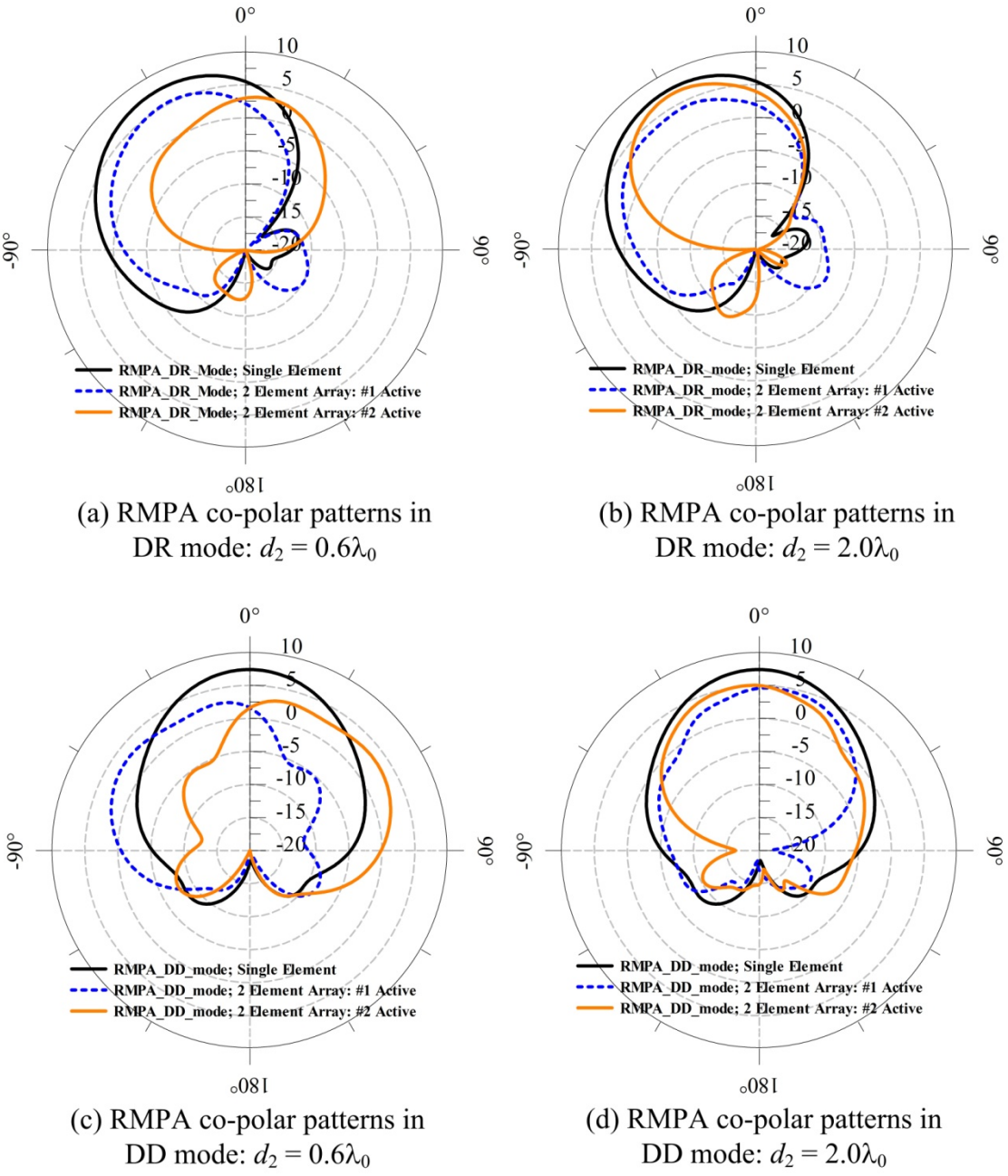

(a) RMPA co-polar patterns in DR mode: $d_2 = 0.6\lambda_0$

(b) RMPA co-polar patterns in DR mode: $d_2 = 2.0\lambda_0$

(c) RMPA co-polar patterns in DD mode: $d_2 = 0.6\lambda_0$

(d) RMPA co-polar patterns in DD mode: $d_2 = 2.0\lambda_0$

Figure 2-7: Co-polar simulated radiation patterns of the RMPA in DR mode, cases (a) and (b), and in DD mode, cases (c) and (d); the mode pertains to select array states and element separations. In all plots the single-element (black [or dark] curve), active element pattern of element 1 (dotted curve), and active element pattern of element 2 (orange [or light] curve) are shown. In cases (a) and (c), $d_2 = 0.6\lambda_0$; in cases (b) and (d), $d_2 = 2.0\lambda_0$.

While these two pattern reconfigurable designs certainly do not represent all pattern reconfigurable antennas, they do provide insight into the complications that could arise if they were implemented in a half-wavelength-spaced linear array. By examining the mutual coupling effects through S_{21} and the active element patterns, insight is gained into how the spacing should be set for the general study in the following chapters. The spacing also plays a role in constraining the number of pattern reconfigurable elements on an adaptive array system package. For example, consider the RMPA previously discussed. In a military scenario, the system package could be mounted on a platform attached to the soldier's back (e.g., a wearable vest). In terms of physical size, the human body model in [27] gives the width and height dimensions of the upper back platform area of about 46 cm by 60 cm, respectively. As discussed in [28], many engineering applications in this area have much interest in operating in the 2.45 GHz band. Thus, an example spacing of $1.5\lambda_0$ between RMPA elements operating at this frequency would allow two elements along the width and three along the height of the prescribed platform, which is a small footprint such as needed for portability.

CHAPTER 3
ADAPTIVE ARRAY FUNDAMENTALS

This chapter gives an overview of adaptive arrays, first discussing some of the fundamental concepts and then the analytical relationships utilized in this research. Afterwards, a detailed account on the adopted grating null mitigation method by R.T. Compton Jr. is discussed. The next sections present a flow chart illustrating how grating nulls occur, followed by an alternate, more intuitive, way to consider how they form. The last section details the methodology that is used in this dissertation and which will be used in later chapters for analysis and results.

3.1 Overview

The multidisciplinary aspects of adaptive arrays closely correlate with the advancing interactions between electromagnetics and digital signal processing [29]. This is why they are the subject of great interest in a wide range of technological areas, e.g., radar and communication applications [30]. Fundamentally, an adaptive antenna system controls its pattern in response to the signal environment. A performance index (PI) gauges the system's ability to accomplish the task of enhancing the desired signal and rejecting the undesired interference signals (e.g., jammers). Some example PIs include signal-to-interference plus noise ratio (SINR), mean square error, output noise power, and minimal signal distortion [18]. These PIs, as opposed to conventional antenna characteristics, lead to more convenient forms of feedback for control of the array pattern [17]. In this work, the PI of interest is the SINR.

Figure 3-1 illustrates a general layout of a linear N-element adaptive array, including the geometric layout and its principal components. These components consist of the antenna or sensor array, the beam former, and a real-time adaptive processor. Suppose desired and interference signals impinge upon on the array (shown in Figure 3-1). First, the signal processor collects two forms of data: (1) the signal information from each antenna before entering the beam former and (2) the output $s(t)$ that feeds back

into the signal processor. Then, the processor's job is to distinguish between the desired and interference signals using either *a priori* or learned knowledge about the signals. Next, the adaptive control algorithm adjusts the complex weight of each antenna, which determines how the radiation pattern receives the desired and interference signals. In effect, the array output $s(t)$ changes through feedback until the system reaches steady state.

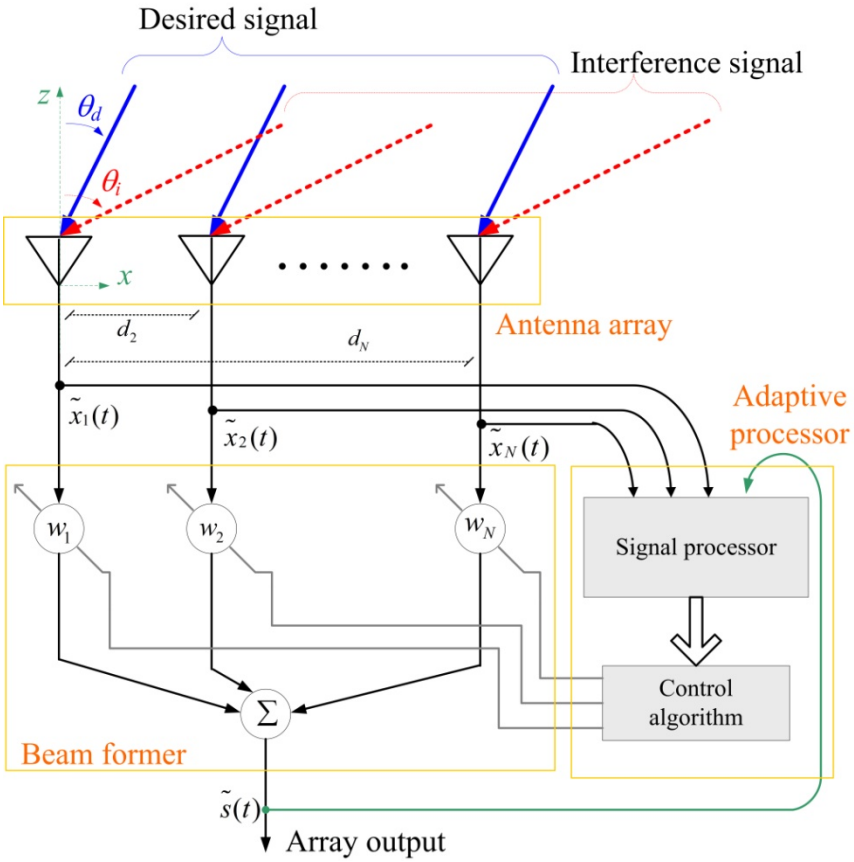

Figure 3-1: Adaptive array block diagram illustrating the geometrical layout and the primary system components: antenna array, beam former, and adaptive processor.

A number of factors affect the performance of an adaptive array; these include array topology (the number of elements and element spacing) and the antenna elements themselves [17]. An *N*-element array has *N* minus 1 degrees of freedom to null out the interfering signals, and element location determines array resolution and interferometer effects. In terms of the antenna element, its individual pattern, along with the complex

weights within the beam former, and the aforementioned element spacing dictate overall beam pattern sensitivity. These dynamic factors determine how well the specified requirements can be met for a given signal environment [18]. The fact that the individual element patterns play a major role in adaptive array performance lends itself well to the utility of pattern reconfigurable antennas in such a setting.

3.2 Analytical Relationships

This section presents the analytical concepts outlining the framework used in future calculations. In reference to Figure 3-1, assume a single desired and interference signal are incident on the *N*-element array—both continuous wave and time harmonic in nature. Also, the spacing between element 1 (the zero-phase, reference element) and element N is given by d_N (in wavelengths). Then the summation of the desired, interference, and thermal noise vectors ($\vec{X}_d$, $\vec{X}_i$, $\vec{X}_n$, respectively) generates the total signal vector $\vec{X}$ [17] given as $\vec{X} = \vec{X}_d + \vec{X}_i + \vec{X}_n$. Thus, thus the array output yields

$$\tilde{s}(t) = \sum_{j=1}^{N} w_j \tilde{x}_j(t) = \vec{w}^T \vec{X}\,, \tag{3.1}$$

where $\vec{w}$ is the weight vector with matrix element w_j, and superscript T indicates transpose.

The adaptive processing unit takes on the task of computing the weight vector via an inversion of the covariance matrix, i.e., $\vec{w} = \Phi^{-1}\vec{S}$, where Φ (given by the expectation of the total signal vector and its complex conjugate) is the covariance matrix and $\vec{S}$ relates to the reference correlation vector. The covariance matrix refers to a matrix containing the averaged cross-products of all the element signals. Moreover, the weight vector is typically computed via an algorithm that aims to satisfy some criteria. Two common techniques exist for computing the weight vector: (1) the least mean square (LMS) algorithm, which minimizes the error in the signal, and (2) the Applebaum approach, which maximizes the desired-to-undesired signal ratios at the array output [17].

It is known that the LMS weights in an array yield the maximum SINR that can be obtained from a given set of signals [20].

The array signal vector $\vec{U}(\theta)$ contains the element pattern and phase shift information for each antenna element, given by

$$\vec{U}(\theta)=\begin{pmatrix} f_1(\theta) \\ f_2(\theta)\, e^{j\frac{2\pi}{\lambda}d_2\sin\theta} \\ \vdots \\ f_N(\theta)\, e^{j\frac{2\pi}{\lambda}d_N\sin\theta} \end{pmatrix}. \tag{3.2}$$

This array signal vector can be evaluated in two ways: (a) as the desired signal vector $\vec{U}_d=\vec{U}(\theta=\theta_d)$, where θ_d is the angle of arrival of the desired signal, and (b) as the interference signal vector $\vec{U}_i=\vec{U}(\theta=\theta_i)$, where θ_i is the angle of arrival of the interference signal. Note, $f_N(\theta)$ is the amplitude pattern function of the N^{th} element. Additionally, for the PI of interest, SINR is given by the ratio of the received signal power in the desired signal to that of the power in the interference and noise signal. In general, it can be expressed as indicated in (3.3):

$$SINR=\frac{\vec{w}^H\ \Phi_d\ \vec{w}}{\vec{w}^H\ \Phi_u\ \vec{w}}. \tag{3.3}$$

In this expression, $\vec{w}^H$ represents the Hermitian of $\vec{w}$, Φ_d is the desired signal covariance matrix, and Φ_u is the undesired signal covariance matrix. Physically, the form of (3.3) represents a energy/power ratio ($\vec{w}$ and $\vec{w}^2$) in relation to the ratio of the desired and undesired covariance matrix. Compton [17] presents the SINR in a simpler form, i.e., in terms of the array signal vectors:

$$SINR=\xi_d\left[\vec{U}_d{}^T\vec{U}_d{}^* - \frac{\left|\vec{U}_d{}^T\vec{U}_i{}^*\right|^2}{\xi_i^{-1}+\vec{U}_i{}^T\vec{U}_i{}^*}\right]. \tag{3.4}$$

In (3.4), ξ_d translates to the desired signal-to-noise ratio (SNR), and ξ_i translates to the interference signal-to-noise ratio (INR) per element, which are assumed equal for each element [17]. Finally, the array voltage pattern, another parameter of significance, is given by the dot product of the weight vector and the array signal vector, i.e.,

$$p(\theta) = \left| \vec{w}^T \vec{U}(\theta) \right|. \tag{3.5}$$

3.3 Applied Technique

The present work adopts a technique realized by Compton [20], in which he derives a set of conditions required for the N^{th} + 1 element in an N-element linear adaptive array. Given a set of signal parameters, the conditions yield maximum SINR. The additional auxiliary element's purpose is to enhance SINR performance compared to that of the original N-element array. In fact, the auxiliary element functions to mitigate an undesirable effect in the SINR that occurs due to the arrangement of element pattern types and elemental spacing: grating nulls.

Grating nulls, as discussed by Ishide and Compton [21], occur when the desired and interference signal vectors are parallel, i.e., $\vec{U}_d = k\vec{U}_i$, where k is a constant. Effectively, the two signal vectors are electrically indistinguishable, and a weight vector chosen to null the interference signal will also null the desired signal. Two types of grating nulls exist: (a) conventional grating nulls (CGN), which can arise for equal element patterns, and (b) sign reversal grating nulls (SRGN), which can take place for unequal element patterns. The occurrence of CGNs parallels that of grating lobes in a standard array, and SRGNs occur when one element's pattern changes its sign between θ_d and θ_i while another maintains the same sign at θ_d and θ_i. In keeping with the research objective of using a small number of antenna elements, a two-element array with the addition of a third auxiliary element is evaluated as part of the initial investigation. Figure 3-2 clarifies the grating null adaptive process in a cause-and-effect type

relationship for this particular array topology. For a two-element array, the grating null condition simplifies into the following form:

$$\frac{f_1(\theta_d)}{f_2(\theta_d)} = \pm \frac{f_1(\theta_i)}{f_2(\theta_i)} \tag{3.6}$$

and

$$e^{j\frac{2\pi}{\lambda_0} d_2 \sin\theta_d} = \pm e^{j\frac{2\pi}{\lambda_0} d_2 \sin\theta_i}. \tag{3.7}$$

The "+" sign in (3.6) and (3.7) corresponds to CGNs and the "–" sign corresponds to SRGNs; both relationships must be satisfied for grating nulls to occur.

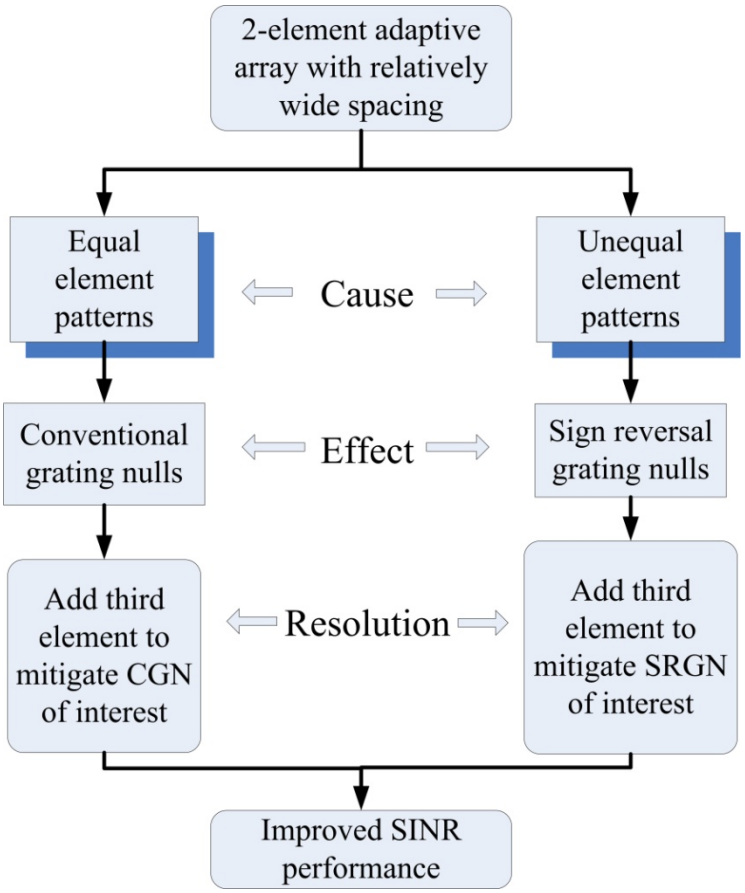

Figure 3-2: Example flow chart diagram illustrating the grating null process.

3.4 Grating Nulls: Further Discussion

The grating null relationship expressed in (3.6) and (3.7) can be interpreted graphically using a traditional phasor-vector diagram, which in essence gives another perspective on how grating nulls formulate. As an example, consider the CGN case that specifies equal element patterns in the array. This result satisfies the amplitude condition in (3.6). Also, let the arguments in the exponentials translate from θ space to ψ space. For CGN, (3.7) becomes

$$e^{j\psi_d} = e^{j\psi_i}, \tag{3.8}$$

where $\psi_x = {}^{2\pi}\!/_{\lambda_0}\, d_2 \sin(\theta_x)$. Instead of the traditional phasor diagram in a circular complex plane, Figure 3-3 shows an *unwrapped* rectangular complex phasor diagram with the horizontal axis representing ψ_i (in degrees) and the vertical axis representing the phasor amplitude.

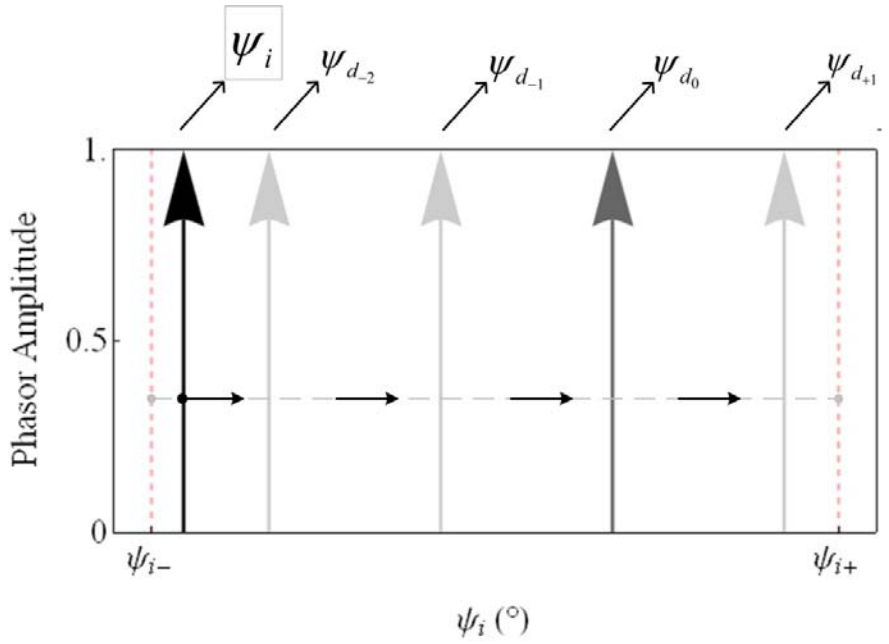

Figure 3-3: Illustration of the grating null occurrence using an unwrapped phasor diagram in rectangular format.

In the figure, ψ_{i+} and ψ_{i-} are the limits in ψ space within the desired viewable space (a correspondence to θ = ±90°, respectively). Depending on the value of ψ_d, n number of ψ_{d_n} phasors will exist within the ψ_i limits (n is an integer). Envision the ψ_i phasor starting at the ψ_{i-} limit ($\theta_i = -90°$). As θ_i increases, ψ_i traverses the horizontal axis until it reaches ψ_{i+}. Every time it aligns itself with a ψ_{d_n} phasor, a CGN event occurs, which happens at every instance except for the case when n = 0. For n = 0, the desired and interference signals are coming from the same direction (i.e., $\theta_i = \theta_d$). A null does occur, but this is an expected result, since the adaptive array's objective requires a null in the interference direction. Also, for a grating null to occur, not only must the ψ_i and ψ_{d_n} phasors line up in angle space, but they must match in amplitude as well. This condition makes it more difficult for SRGNs to occur, because now the amplitude values of the patterns factor play a role.

3.5 Methodology

This section outlines the steps taken in the analysis that explores the functional benefits of utilizing pattern variability adaptive arrays. As a first step, consider the element patterns to be in functional form—those resembling tilted dipole patterns [20,21]. They are given by

$$f_j(\theta) = \cos\left(\theta - \theta_{n\,j}\right), \tag{3.9}$$

where the main beam maximum resides at $\theta_{n\,j}$ with $\theta_{n\,j} = 0^\circ$ corresponding to broadside. The basic constituents of the analysis involve evaluating the N = 2 array performance for a select number of beam tilts and then determining the third element (auxiliary element) parameters (θ_{n3}, d_3) that improve SINR performance.

For this study, a pool of potential beam tilts, chosen from –60° to +60° in 15° increments (forming a $\{\theta_{n1}, \theta_{n2}\}$ pair) representing the reconfigurations in a conceivable

pattern reconfigurable antenna. Selecting from this pool, along with a set (θ_d, d_2) in (3.6) and (3.7), determines what type of grating nulls exist and where they are located in terms of θ_i. Utilizing these parameters further, the next step in the methodology involves finding the third element properties, (θ_{n3}, d_3). They can be found using the following relations given in [20]:

$$\left| f_3(\theta_d)\ f_3(\theta_i) \right| = \left| \vec{U}_d{}^T \vec{U}_i^* \right| \tag{3.10}$$

and

$$\measuredangle f_3(\theta_d)\, e^{j\frac{2\pi}{\lambda_0} d_3 \sin\theta_d} - \measuredangle f_3(\theta_i)\, e^{j\frac{2\pi}{\lambda_0} d_3 \sin\theta_i} = \measuredangle \vec{U}_d{}^T \vec{U}_i^{\,*} - \pi\,. \tag{3.11}$$

A program written in Mathematica® calculates and displays the results, which include two key figures of merit for a given scenario: (1) the SINR versus interferer incident angle θ_i and (2) the voltage radiation pattern, $p(\theta)$ versus spatial angle θ, both on a dB scale. Note that all cases assume a signal environment encompassing strong interferers (i.e., ξ_i = 40 dB with ξ_d = 0 dB).

3.6 Chapter Summary

This chapter first presented some of the fundamentals behind an adaptive array system, including the geometrical layout and the key analytical relationships involved. Subsequent sections discussed the occurrence of grating nulls and the overall methodology utilized in determining the necessary parameters required for grating null mitigation. In essence, the antenna array in conjunction with the real-time adaptive processor's algorithm adjusts the weights toward optimizing the SINR output. The system adapts to the total signal environment "seen" by the array of sensors, using all available degrees of freedom available to the algorithm in an optimum sense. Utilizing radiation reconfigurable antennas in this setting potentially increases the number of degrees of freedom even further. The next chapter includes graphical results that demonstrate this concept.

CHAPTER 4
ADAPTIVE ARRAY IMPLEMENTATION

The previous chapter explained a number of analytical relationships pertaining to the adaptive array process. It also outlined the adaptive array technique developed in [20,21] and the proceeding methodology to mitigate grating nulls with antenna elements via their beam tilting capabilities. This chapter implements the technique and presents several graphical results related to a number of adaptive array scenarios. First, the different types of grating nulls are analyzed (e.g., conventional and sign reversal); then a brief discussion about an undesirable solution scenario follows. Finally, the last section moves away from using ideal elements in the solution set and incorporates a practical pattern reconfigurable antenna element into the methodology. The analysis and results are presented similarly to the ideal element case.

4.1 Conventional Grating Nulls

Recall that CGNs particularly arise for equal element patterns. Consider Figure 4-1, which shows an interpretation of (3.6) and (3.7) in graphical form [21]. The θ_i-θ_d axes scale from –90° to +90°, and in this case d_2 equals $2\lambda_0$, which is a favorable distance since it satisfies the goal of having a wider spacing between antenna elements to decrease mutual coupling. A number of *n*-curves present themselves in the graphic, six within the spatial range. Along these curves, a grating null takes place. Thus, for a particular θ_d, intersection with an *n*-curve gives the corresponding grating null (θ_{CGN}) located at θ_i. The labeled example in Figure 4-1 details this. When $\theta_d = -60°$ along the $n = 1$ curve, $\theta_{CGN} = -22°$ due to the interference signal coming from that direction. The number of *n*-curves depends on d_2. As d_2 increases, more curves come into the spatial region of interest, thus increasing the opportunity for more grating nulls to occur.

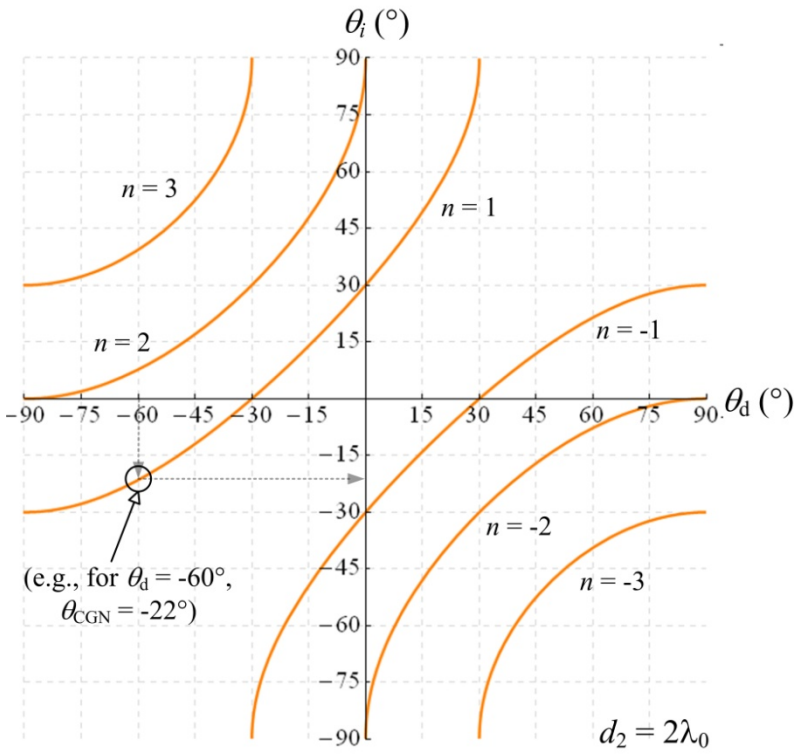

Figure 4-1: Plot illustrating when CGNs occur for an element spacing of $2\lambda_0$. The intersection of a specified θ_d and an *n*-curve results in a grating null at θ_i.

Even within the constraints of this initial investigation, numerous scenarios still present themselves. Thus, Table 4-1 displays the case results for a few example scenarios. In the table, the first three columns represent the specified parameter data (θ_d, d_2, and the $\{\theta_{n1} = \theta_{n2}\}$ pair). The fourth column corresponds to the resulting interferer incident angle at which a grating null occurs (i.e., $\theta_i = \theta_{CGN}$), and the last two columns list the parameters required of the third antenna element to mitigate the grating null and improve SINR performance, θ_{n3} and d_3. The resultant third element parameters in the last two rows of Table 4-1 warrant further discussion. In one case, d_3 does not equal $4\lambda_0$; i.e., the three elements are not equally spaced. In the other case, a no solution (NS) result exists for the third element parameters under the given signal characteristics. The required beam tilt for grating null mitigation is not within the visible range. These types of events do happen for various scenarios and thus require further detailed analysis in order to

Table 4-1: Calculated CGN results based on specified parameters for select cases.

θ_d (°)	d_2 (λ_0)	$\{\theta_{n1} = \theta_{n2}\}$ (°) pair	$\theta_i = \theta_{CGN}$ (°)	θ_{n3} (°)	d_3 (λ_0)
−15	2.0	−60	47.8	**−16.5**	**4.0**
		−45		**36.9**	**4.0**
		−30		**−18.1**	**3.5**
		−15		**NS**	**-**

enhance the possibility of integrating pattern variability in adaptive arrays. In particular, the NS result will be further discussed later in this dissertation.

Figure 4-2 provides the results of the data in the first row of Table 4-1 in graphical form (i.e., $\theta_d = -15°$, $d_2 = 2\lambda_0$, $\theta_{n1} = \theta_{n2} = -60°$, $\theta_i = \theta_{CGN} = 47.8°$, $\theta_{n3} = -16.5°$, and $d_3 = 4\lambda_0$). The plot on the left depicts the SINR (dB) as a function of interferer incident angle θ_i, while the plot on the right shows the array voltage pattern (dB) as a function of spatial angle θ. Within each plot, two curves represent the "before" and "after" conditions, i.e., before the addition of the third element and after the addition of the third element, respectively. It is important to recognize here that the SINR varies with θ_i, and the voltage pattern is plotted for one particular θ_i, $\theta_i = \theta_{CGN}$. Recall that the pattern depends on the element weights, which change as the signal environment changes.

The SINR plot details how, with only two antenna elements in the array, adaptive array performance degrades due to the presence of grating nulls. With the addition of the third element (i.e., the appropriate beam tilt and element spacing) SINR performance improves at the target grating null location (i.e., $\theta_i = 47.8°$). Not only is the SINR maximized at $\theta_i = 47.8°$, but it improves at other grating null locations as well. The SINR results correlate with the before- and after-voltage pattern plots. Since the voltage patterns are plotted for the target grating null, the pattern values suffer in the before case (indicated by the low dB values). After mitigating the grating null, the overall values in the after case curve increase substantially. Note that a null still exists in the pattern at

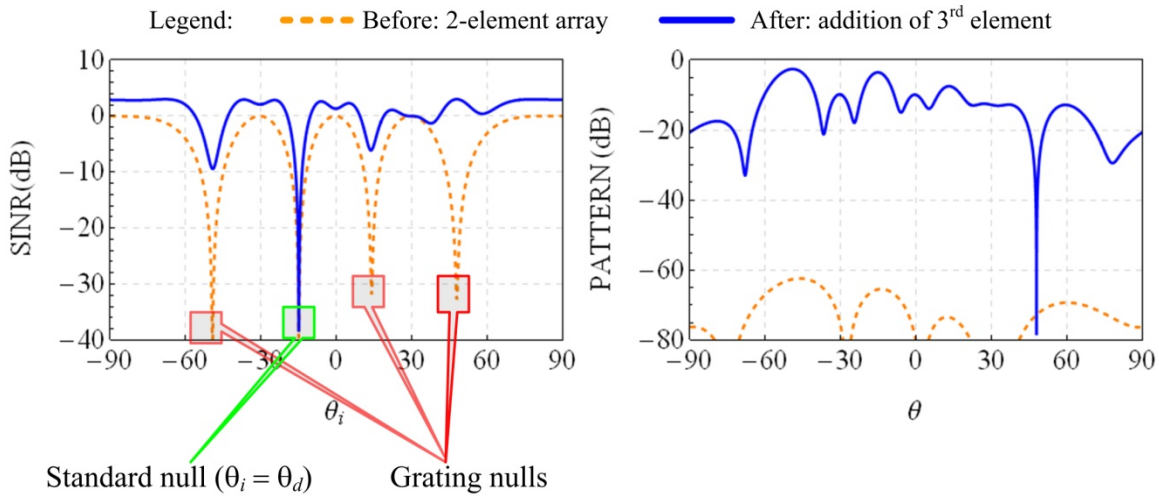

Figure 4-2: Resulting SINR (left) and voltage pattern plot (right) in a CGN scenario with the following parameters: $\theta_d = -15°$, $d_2 = 2\lambda_0$, $\theta_{n1} = \theta_{n2} = -60°$, $\theta_i = \theta_{CGN} = 47.8°$, $\theta_{n3} = -16.5°$, and $d_3 = 4\lambda_0$. The dashed light curve represents the 2-element array and the solid dark curve represents the addition of the third element. SINR and pattern performance (at $\theta_i = 47.8°$) improve with the addition of the beam tilted third element.

θ = 47.8°, an expected result since the interferer is coming from that direction. Altogether, the results show how adaptive array performance improves with the inclusion of pattern variability.

4.2 Sign Reversal Grating Nulls

This section presents the SRGN results in a fashion parallel to the preceding subsection on CGNs. Figure 4-3 shows another interpretation of (3.6) and (3.7), this time for SRGNs. For the same element spacing, a total of seven n curves characterize the plot, as compared to six in the CGN plot. In this case, the n = 0 curve qualifies. Since SRGNs take place for unequal antenna element patterns, they occur less frequently than CGNs. In addition to the n curves (solid), two auxiliary curves (one rectangular-dotted curve and one circle-dotted curve) overlay the plot, with each of these representing two solutions satisfying the relationship in (3.6). These curves represent a specific two-element beam tilt scenario, $\{\theta_{n1}, \theta_{n2}\} = \{60°, 0°\}$ for this plot. An SRGN occurs at the intersection of an auxiliary curve and an n curve. The intersection point specifies θ_d and the grating null location at θ_i required to produce the grating null, θ_{SRGN}.

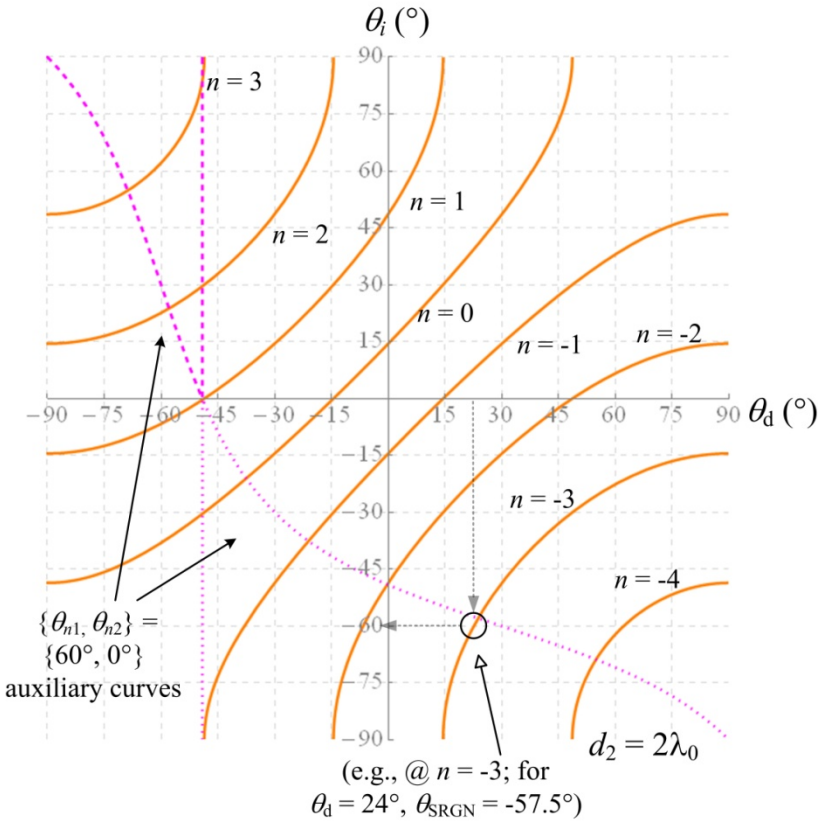

Figure 4-3: Plot illustrating when SRGNs occur for an element spacing of $2\lambda_0$. The intersection of an auxiliary curve and an *n* curve specifies θ_d and the grating null at θ_i.

Again, the labeled example in Figure 4-3 details this. At the intersection of the lower auxiliary curve and the $n = -3$ curve, $\theta_d = 24°$ and $\theta_{SRGN} = -57.5°$.

The auxiliary curves represent a specific $\{\theta_{n1}, \theta_{n2}\}$ configuration, in this case {60°, 0°}. Even though the auxiliary curves for only one $\{\theta_{n1}, \theta_{n2}\}$ pair are shown in Figure 4-3, the behavior of the curves tends to follow a trend as the beam tilt angle changes. Due to the nature of the cosine functions used in (3.7), the auxiliary curves exhibit a sharp discontinuity. For both solutions, the discontinuity occurs near $\theta_d = -48°$ in Figure 4-3. As the separation between θ_{n1} and θ_{n2} increases, the curves change in appearance (e.g., become wider at the base) and shift along the horizontal axis. The closer they come together, the gap between the discontinuity line and the continuous line becomes closer. On the other hand, when both θ_{n1} and θ_{n2} shift their beam tilts by the same amount, the auxiliary curves tend to maintain their shape and shift along the

horizontal axis. Irregular as it may seem, the discontinuous nature of the curves does provide useful insight into potential SRGN behavior.

For SRGNs, Table 4-2 shows the case results for several different $\{\theta_{n1}, \theta_{n2}\}$ pairs; the format parallels Table 4-1. As in Table 4-1, NS results still occur when determining the third-element parameters for select cases. However, d_3 typically equals $4\lambda_0$ for non-NS results. Similarly to Figure 4-2, Figure 4-4 illustrates the results for an SRGN scenario in graphical form, wherein the SINR and voltage pattern plots are displayed. The data curves in the plot result from the parameters listed in the last row of Table 4-2 (i.e., $\theta_d = 0°$, $d_2 = 2\lambda_0$, $\theta_{n1} = 60°$, $\theta_{n2} = 0°$, $\theta_i = \theta_{SRGN} = -48.6°$, $\theta_{n3} = -18.6°$, and $d_3 = 4\lambda_0$). Unlike CGNs, only one SRGN occurs for a set $\{\theta_{n1}, \theta_{n2}\}$ pair.

Table 4-2: Calculated SRGN results based on specified parameters for select cases.

θ_d (°)	d_2 (λ_0)	$\{\theta_{n1}, \theta_{n2}\}$ (°) pair	$\theta_i = \theta_{SRGN}$ (°)	θ_{n3} (°)	d_3 (λ_0)
–60	2.0	{–45, –15}	62.1	**–54.2**	**4.0**
–60		{60, –45}	–6.7	**NS**	**-**
–45		{30, –45}	–73.2	**–58.2**	**4.0**
0		{60, 0}	–48.6	**–18.6**	**4.0**

As expected, the grating null degrades performance in the before-SINR curve (dashed gray) in Figure 4-4. Adding the element with a beam tilt at –18.6° and a spacing of $4\lambda_0$ maximizes SINR at θ_i = -48.6°, as dictated by the after-SINR curve (solid black). Once more, performance improves not just at the grating null location but overall. A few interesting characteristics lie within the pattern plots as well. In the pattern curve of the before case, two distinct nulls stand out: one at $\theta = \theta_i = -48.6°$ and the other in the desired signal direction, $\theta = \theta_d$. As discussed before, the null at $\theta = -48.6°$ is expected because of the interferer. However, with the appropriate third-element parameters, the null at broadside is alleviated and the pattern in the after case along that direction reaches its maximum value. In reality, this in effect maximizes the SINR at $\theta_i = \theta_{SRGN}$.

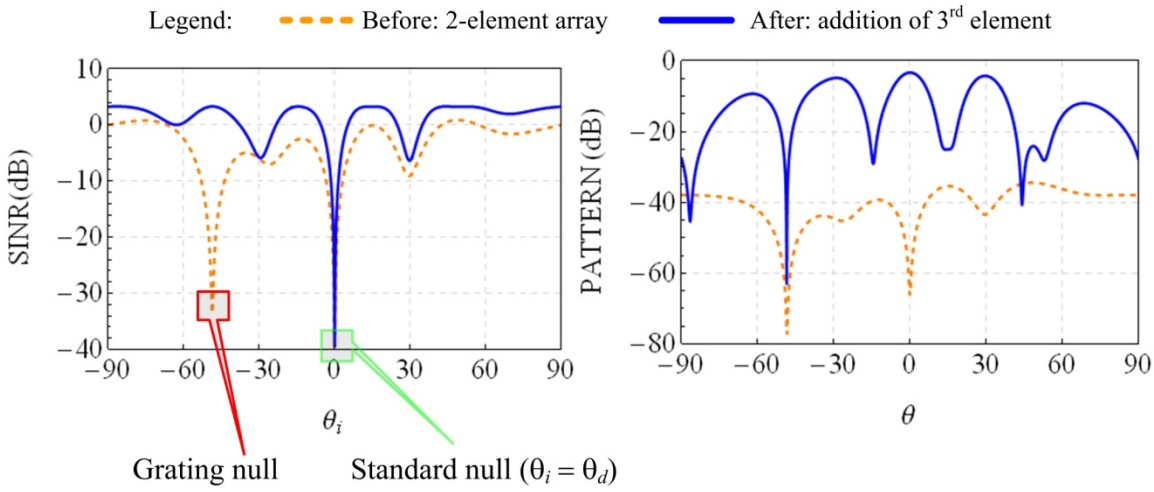

Figure 4-4: Resulting SINR (left) and voltage pattern plot (right) in an SRGN scenario with the following parameters: $\theta_d = 0°$, $d_2 = 2\lambda_0$, $\theta_{n1} = 60°$, $\theta_{n2} = 0°$, $\theta_{SRGN} = -48.6°$, $\theta_{n3} = -18.6°$, and $d_3 = 4\lambda_0$. The dashed light curve represents the 2-element array and the solid dark curve represents the addition of the 3rd element. Clearly, SINR and pattern performance improve with pattern variability.

4.3 Reconfigurable Pattern Implementation

In this section, the process of implementing patterns from radiation reconfigurable antennas into this work begins. The analysis and methodology will parallel that of the preceding sections, thus utilizing the relationships discussed in Chapter 3. As an initial step, we will start by taking a simulated pattern of the RMPA and fit it into a functional form. Next, the occurrences of grating nulls are examined with the reconfigurable antenna's pattern in mind. Finally, the adaptive array metrics of interest, namely the SINR and the voltage pattern, are illustrated making use of this pattern type. Throughout, comparisons to the case when the adaptive array antenna elements are tilted dipoles are made when appropriate.

4.3.1 Reconfigurable Pattern

Despite their simple form, the dipole patterns belonging to the cosine variety used in this work thus far do not represent practical antenna patterns. In this example, the work implements the simulated patterns of the RMPA in DD mode. In order to take advantage of the adaptive array principles in the same manner as previously explained, the RMPA's pattern must be cast into a functional form. One way of doing this involves

curve fitting the pattern with some common analytical functions. Using MATLAB®'s curve fitting toolbox, three candidate fits of various orders were considered for both the magnitude and phase of the pattern: Gaussian, polynomial, and Fourier. The relationship in (3.12) expresses the chosen magnitude fit (third-order Fourier series) and (3.13) conveys the chosen phase fit (fifth-order Fourier series):

$$\begin{aligned} DDMag(\theta,\theta_n) = {} & 6.545 + 7.043\cos\left[w_m(\theta-\theta_n)\right] + 0.187\sin\left[w_m(\theta-\theta_n)\right] + \\ & 2.237\cos\left[2w_m(\theta-\theta_n)\right] - 0.080\sin\left[2w_m(\theta-\theta_n)\right] + \\ & 0.908\cos\left[3w_m(\theta-\theta_n)\right] - 0.182\sin\left[3w_m(\theta-\theta_n)\right], \end{aligned} \tag{3.12}$$

where $w_m = 0.01781$, and

$$\begin{aligned} DDPhase(\theta,\theta_n) = {} & -31.56 + 53.97\cos\left[\frac{w_p}{SF}(\theta-\theta_n)\right] + 3.366\sin\left[\frac{w_p}{SF}(\theta-\theta_n)\right] - \\ & 38.51\cos\left[2\frac{w_p}{SF}(\theta-\theta_n)\right] - 4.816\sin\left[2\frac{w_p}{SF}(\theta-\theta_n)\right] + 21.74\cos\left[3\frac{w_p}{SF}(\theta-\theta_n)\right] + \\ & 3.958\sin\left[3\frac{w_p}{SF}(\theta-\theta_n)\right] - 8.901\cos\left[4\frac{w_p}{SF}(\theta-\theta_n)\right] - 1.961\sin\left[4\frac{w_p}{SF}(\theta-\theta_n)\right] + \\ & 1.706\cos\left[5\frac{w_p}{SF}(\theta-\theta_n)\right] + 0.4705\sin\left[5\frac{w_p}{SF}(\theta-\theta_n)\right], \end{aligned} \tag{3.13}$$

where $w_p = 0.9535$ and $SF = 104.4$, all being factors belonging to the fit.

In both expressions, note the functional dependence on not only the spatial variable θ but also the parametric variable θ_n. Inclusion of this beam tilting parameter allows for rotation of the pattern from broadside to the angle θ_n. So with this in mind, assume that the magnitude and phase of the individual antenna element tilt in parallel and that a practical reconfigurable antenna can produce the associated magnitude and phase in its radiation pattern. Figure 4-5 compares the magnitude fit (dashed curve) while Figure 4-6 compares the phase fit (dashed curves) to the actual simulated pattern (solid curves). The dipole pattern (dot-dashed curves) is included for reference; and for a fair

comparison, its magnitude has been scaled up to the maximum of the DD mode pattern. In all plots, $\theta_n = 0°$ (standard broadside mode), so there is no beam tilting depicted.

The results show that the fitted curves match well with the simulated patterns of the RMPA in DD mode. Note that since the simulations present the magnitude pattern in terms of the rE (radial electric) field, the adopted units of measure are in dBV. In reality the actual values do not matter as much as the curves' relative differences. Nevertheless, the results also show the pattern differences compared to the ideal dipole pattern in (3.9), particularly in regard to its step-like phase behavior. Here the magnitude and phase have been separated, whereas before they were grouped solely within the single cosine function described in (3.9).

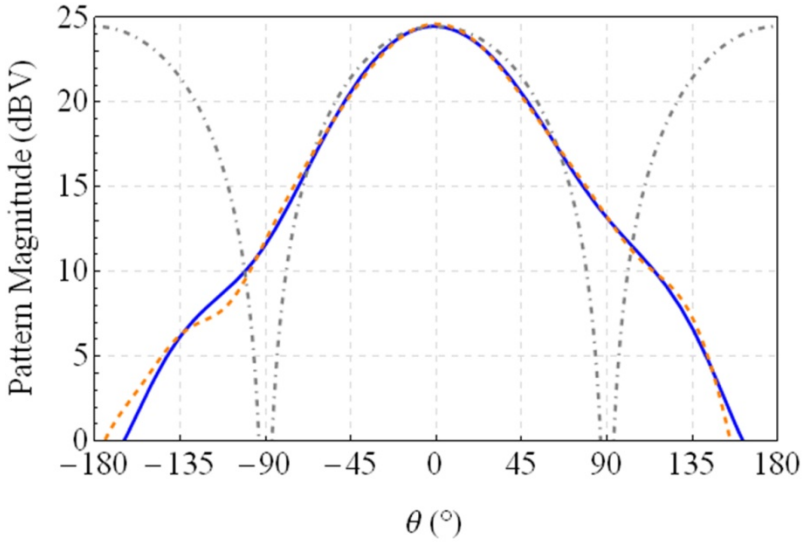

Figure 4-5: Graph comparing the magnitude of the curve-fitted radiation pattern (dashed orange curve) to the RMPA magnitude pattern in DD mode (solid blue line). The dot-dashed curve represents the magnitude of the previously implemented dipole pattern scaled to the maximum of the fitted RMPA pattern. The fitted pattern stems from the expression in (3.12).

So in particular, why the chosen fits expressed in (3.12) and (3.13)? As mentioned, a large number of different fit types of various orders were analyzed. The main criterion used to select the best fit related to statistical parameters specifying the goodness of the fit (i.e., SSE and R-squared value) and the number of terms and parameters in the fit expression. The SSE value measures the sum of the squares due to error, and the R-squared value measures how successful the fit is in explaining the

variation in the data [31]. For comparison purposes, a low SSE and an R-squared value close to 1 is best. The third-order Fourier series (comprised of eight parameters) representing the magnitude fit has a SSE = 12.04 and an R-squared value equal to 0.9988. Comparing this result to a third-order Gaussian series (comprised of nine parameters), for example—which has an SSE = 14.78 and R-squared equal to 0.9985—the Fourier fit has a better SSE value and one less parameter in the fit function. Similar conclusions hold for the phase fit. As a side note, the ability of the Fourier functions (positive and negative functions) to best represent the non-negative data of the RMPA dictates the functions' effectiveness. Intuition might lead to thinking that a fit composed of non-negative functions would work best (e.g., polynomials); however, such is not the case as the polynomial fit performed worse. Later work detailed in Chapter 7 indicates that implementing curve fitting to characterize reconfigurable patterns will not be necessary.

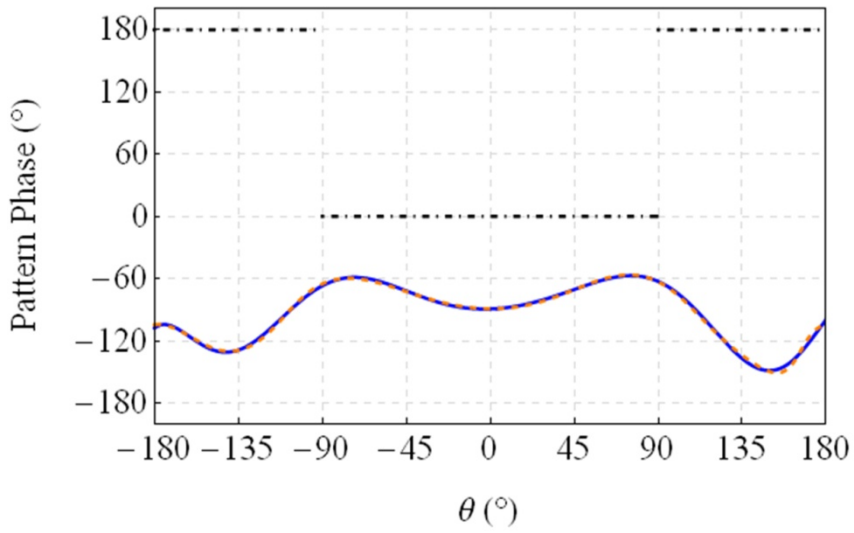

Figure 4-6: Graph comparing the phase of the curve-fitted radiation pattern (dashed orange curve) to the phase of the RMPA pattern in DD mode (solid blue line), in degrees. The dot-dashed curve represents the step-like phase of the previously implemented dipole pattern. The fitted phase stems from the expression in (3.13).

4.3.2 Grating Nulls

Next, the focus of this work turns to examining the effects of implementing the curve-fitted radiation pattern on grating nulls. Before presenting the graphic results, this section discusses the changes to the grating null condition as applied to this

implementation—changes with respect to the definitions outlined with the dipole pattern representing the antenna elements.

Recall that the expressions given in (3.6) and (3.7) portray the grating null condition for the two-element array. Due to the nature of the cosine (dipole-like) function used to represent the antenna element's radiation patterns, a separate pair of expressions exists for the CGNs and SRGNs. Given the fact that the simulated pattern has a separate magnitude and phase, the condition for grating nulls to occur can now be written as

$$\frac{|f_1(\theta_d)|}{|f_2(\theta_d)|} = \frac{|f_1(\theta_i)|}{|f_2(\theta_i)|} \tag{3.14}$$

and

$$e^{j\left[\psi_d - \angle f_1(\theta_d) + \angle f_2(\theta_d)\right]} = e^{j\left[\psi_i - \angle f_1(\theta_i) + \angle f_2(\theta_i)\right]}. \tag{3.15}$$

Equation (3.14) represents the magnitude relationship and (3.15) characterizes the phase relationship. Note the additional phase terms in the argument of the exponential in (3.15). Moreover, since (3.14) and (3.15) present just one pair of conditions that must hold for grating nulls to occur, a different nomenclature will be devised when it comes to deciphering grating null types: Type I grating nulls (θ_{gn1}), for identical element patterns in the array (i.e., $\theta_{n1} = \theta_{n2}$); and Type II grating nulls (θ_{gn2}), for non-identical element patterns in the array (i.e., $\theta_{n1} \neq \theta_{n2}$). In fact, an SRGN, taken by its literal meaning, does not make sense here, because the magnitude of one of the element's patterns will never change sign when going from θ_d to θ_i.

Finally, one more comment in regard to the overall approach taken to determine the results using the simulated radiation patterns. Before, the simple cosine relationship representing the dipole patterns manufactured nice, solvable, analytical forms when it came to determining grating nulls and the properties of the third element. With the more complicated fit expressions, those detailed in (3.12) and (3.13), such is not the case. Therefore, the relationships used to determine the grating nulls and third-element parameters are solved numerically by comparing both sides of the equality to within a

tolerance value. In determining the grating nulls, the error used in the phase expression of (3.15) is less than 0.05 and that of (3.14), the magnitude expression, is less than 0.25. To determine the third-element parameters described in (3.10) and (3.11), an error less than 1 is used to find θ_{n3}, and an error less than 0.1 is used to find d_3.

Figure 4-7 illustrates the Type I grating null range plot that dictates the occurrence of grating nulls for equal element patterns in the two-element array (the "before" condition). The plot parallels the CGN plot in Figure 4-1. Since the plot characterizes θ_i versus θ_d (θ_d ranging from –90° to +90° in 5° increments), every large dot along the vertical line represents a Type I grating null, i.e., $\theta_i = \theta_{gn1}$, for the corresponding θ_d. Interestingly, tracing these dots out reveals the n curves from before, thus the plot is more or less a discretized version of the one in Figure 4-1. Therefore, the locations of the grating nulls are the same for both the CGN and Type I GN scenarios, an expected result due to the two array elements having equal beam tilts.

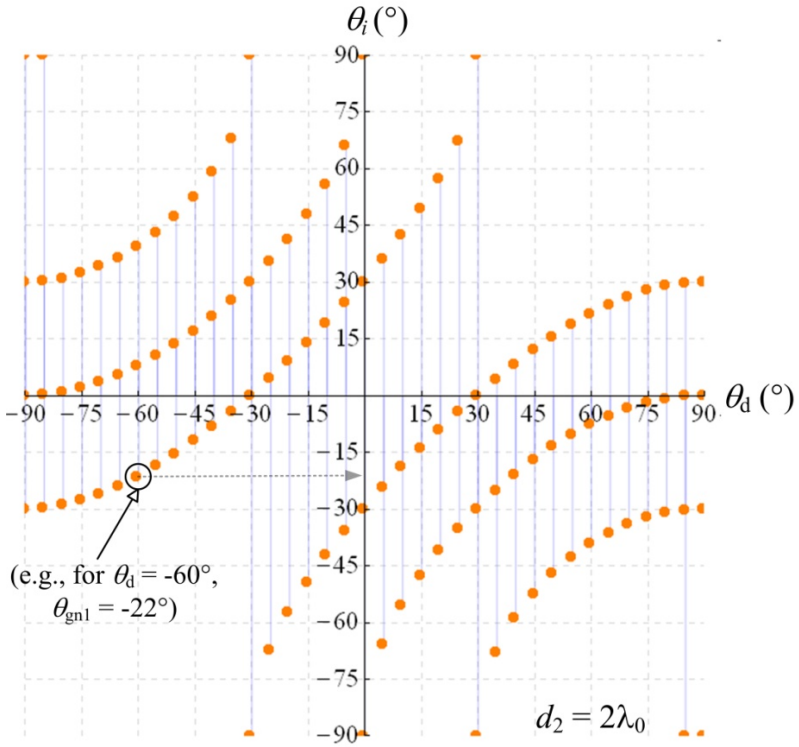

Figure 4-7: Plot illustrating the occurrence of Type 1 GNs for an element spacing of $2\lambda_0$. The graph resembles the CGN plot in Figure 4-1, in this case simulated element patterns are incorporated into the methodology. For discrete values of θ_d, Type I GNs occur at the corresponding $\theta_i = \theta_{gn1}$, located at the points along each stem.

Next, consider the two example plots in Figure 4-8. They illustrate a Type II GN scenario, in the same format as Figure 4-7 but somewhat different in presentation from the SRGN plot in Figure 4-3. Since the Type II GNs correspond to the array elements having different beam tilts (i.e., $\theta_{n1} \neq \theta_{n2}$), each graph corresponds to a different $\{\theta_{n1}, \theta_{n2}\}$ pair. In plot (a), $\{\theta_{n1}, \theta_{n2}\} = \{60°, 0°\}$; and in plot (b), $\{\theta_{n1}, \theta_{n2}\} = \{50°, 60°\}$. Once again, in each plot the dot(s) along the vertical line represent a Type II GN for the corresponding θ_d (i.e., at that point $\theta_i = \theta_{gn2}$). Once again, the graphs illustrate the formation of *n* curves along the grating null locations.

The results in Figure 4-8 show some interesting findings with regard to grating null occurrence for unequal element patterns. When the beam tilts of the two array elements are identical, the Type I GNs results equate to CGN results (i.e., utilizing the dipole element patterns). However, such is not the case when the array element's beam tilts are not equal; the Type II GNs results do not equate to the SRGN results. This effect is due to the radiation reconfigurable antenna's pattern magnitude and phase. For example, plot (a) of Figure 4-8 utilizes the same beam tilt combination utilized to display the results presented in the SRGN plot of Figure 4-3. Recall, in Figure 4-3, the SRGNs occurred at the intersection of the $\{\theta_{n1}, \theta_{n2}\} = \{60°, 0°\}$ auxiliary curve and an *n* curve. These points do not match in location and in number when compared to the Type II GNs displayed in Figure 4-8.

Next, consider plot (b) of Figure 4-8. Recall that using the dipole patterns in the study revealed the fact that only *one* SRGN occurred for a θ_d and a $\{\theta_{n1}, \theta_{n2}\}$ pair. Apart from the fact that a large number of Type II GNs exist, the results in Figure 4-8 (b) stray from this occurrence by having at times *three* grating null events for a single θ_d and a set $\{\theta_{n1}, \theta_{n2}\}$pair. True, this does give more chances for interference signals to degrade adaptive array performance; but at the same time, it also gives more opportunities to utilize pattern variability to mitigate the grating null effect.

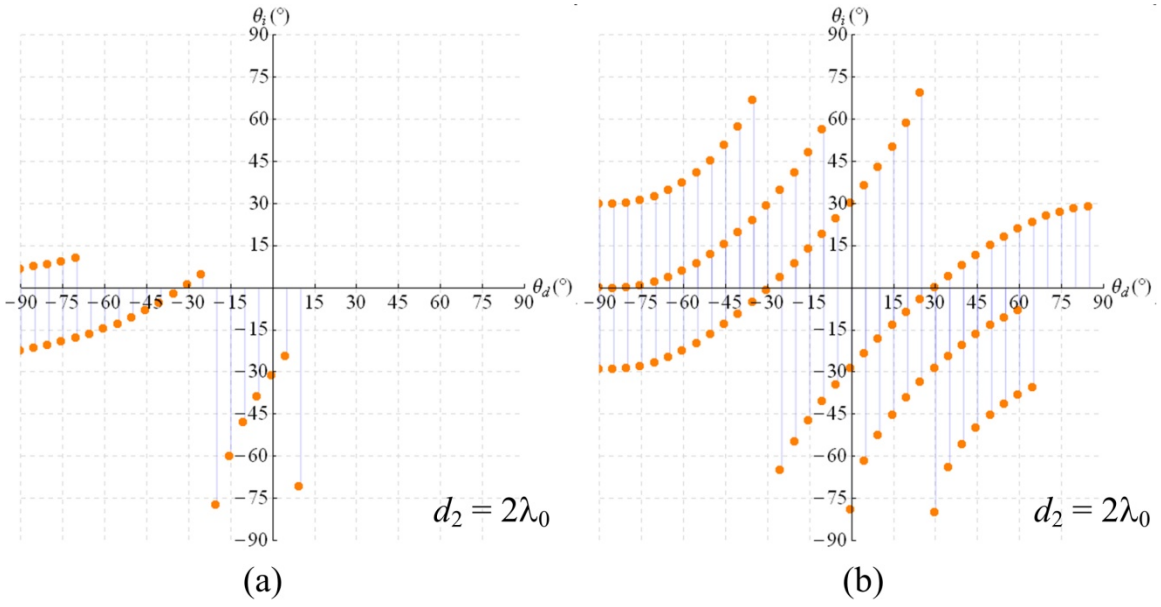

Figure 4-8: Plots illustrating the occurrence of Type II GNs for an element spacing of $2\lambda_0$. The format of the plots parallels the Type I scenario in Figure 4-7. For discrete values of θ_d, Type II GNs occur at the corresponding $\theta_i = \theta_{gn2}$, located at the points along each stem. In plot (a), $\{\theta_{n1},\theta_{n2}\} = \{60°, 0°\}$; and in (b), $\{\theta_{n1},\theta_{n2}\} = \{50°, 60°\}$.

4.3.3 Signal to Interference Noise Ratio and Pattern Plots

This subsection discusses the effects of the grating nulls through the SINR and voltage pattern plots for several different parameter scenarios. The plots will once again compare the "before" condition (the two-element array) with the "after" condition (addition of the third element). When applicable, results will include the data plots pertaining to when the adaptive array antenna element's patterns belong to the ideal dipole class. The results will show the differences in performance when using more realistic antenna patterns and continue to demonstrate the usefulness of pattern reconfigurable antennas with beam tilts in this particular setting.

Figure 4-9 shows the SINR versus interference angle θ_i and the voltage pattern versus spatial angle θ for the two-element array, the graph compares the dipole pattern results (solid line) and the RMPA in DD mode results (dotted curve). In this scenario, the element patterns are equal, and thus the results present a CGN versus Type I GN comparison with the following common parameters: $\theta_d = -15°$, $\theta_i = \theta_{CGN} = \theta_{gn1} = -49.4°$, $\theta_{n1} = \theta_{n2} = 45°$, and $d_2 = 2\lambda_0$. In the SINR plot, the grating nulls match for both pattern

types, an expected result. The spike in the SINR dipole curve at around $\theta_i = -45°$ is due to the cosine function causing a null in the element patterns. Also, the voltage pattern results show that when plotted at a grating null angle, the DD mode-based patterns do not bottom out as does the dipole-based pattern. Nevertheless, the patterns still suffer due to the effects of the grating null.

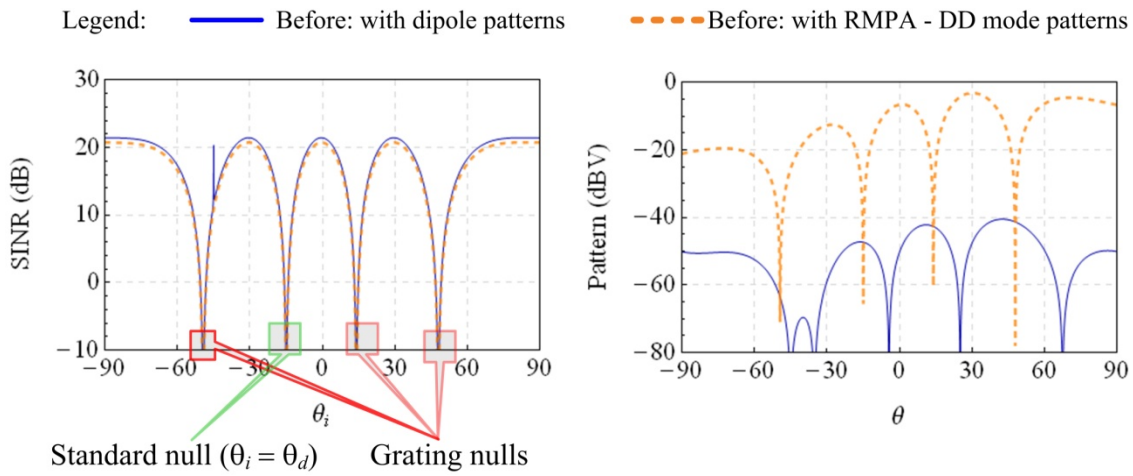

Figure 4-9: Resulting SINR (left) and voltage pattern plot (right) in an equivalent CGN, Type 1 GN scenario with the following parameters: $\theta_d = -15°$, $\theta_i = \theta_{CGN} = \theta_{gn1} = -49.4°$, $\theta_{n1} = \theta_{n2} = 45°$, and $d_2 = 2\lambda_0$. Both cases represent the "before" condition (i.e., only the 2-element array). Utilizing the dipole patterns results in the solid curve, and using the RMPA in DD mode patterns give the dashed curve.

Figure 4-10 shows the results for the same two-element array parameters given for Figure 4-9, but with the addition of the third element whose tilted pattern aims to mitigate the target grating null at $\theta_i = -49.4°$. The third-element parameters for each case are as follows: when using dipole patterns, $\theta_{n3} = 34.0°$ and $d_3 = 4.0\ \lambda_0$, and when using the RMPA in DD mode patterns, $\theta_{n3} = 28.5°$, and $d_3 = 3.1\lambda_0$. The SINR plot demonstrates that with the calculated beam tilt, the target grating null at $\theta_i = -49.4°$ in Figure 4-9 is now mitigated in Figure 4-10. Note the increase in performance at other grating nulls with the DD mode patterns compared to using the dipole patterns in the adaptive array. In the voltage pattern plot, the two curves differ in distributing their energy across the spatial domain; both aim to null the interferer at $\theta = -49.4°$and maximize the pattern in the desired signal direction, $\theta_d = -15°$.

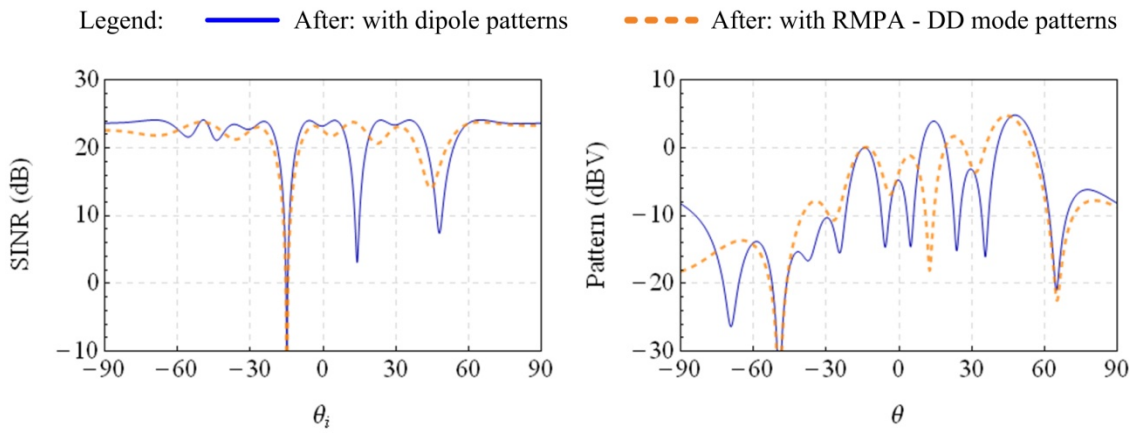

Figure 4-10: Resulting SINR (left) and voltage pattern plot (right) in an equivalent CGN, Type 1 GN scenario with the following parameters: $\theta_d = -15°$, $\theta_i = \theta_{CGN} = \theta_{gn1} = -49.4°$, $\theta_{n1} = \theta_{n2} = 45°$, and $d_2 = 2\lambda_0$. Now both cases represent the "after" condition (i.e., with the addition of the third element). Again, the solid curve represents using the dipole patterns (with $\theta_{n3} = 34.0°$ and $d_3 = 4.0\ \lambda_0$) and the dashed curve represents using the RMPA in DD mode patterns (with $\theta_{n3} = 28.5°$, and $d_3 = 3.1\lambda_0$).

Lastly, the SINR and voltage pattern plots displayed in Figure 4-11 show the "before" and "after" scenario for a Type II GN case—this time with no comparison to using dipole element patterns in the array. The parameters of interest in this case are $\theta_d = 0°$, $d_2 = 2\lambda_0$, $\theta_{n1} = -45°$, $\theta_{n2} = -30°$, $\theta_i = \theta_{gn2} = -71.8°$, $\theta_{n3} = -9.6°$, and $d_3 = 3.5\ \lambda_0$. The SINR plots show that the before-curve (dashed) results exhibit three potential grating nulls, an unlikely result when the beam tilts of the two array elements were unequal for the dipole pattern-based study. Nevertheless, utilizing pattern variability, the third element's beam tilting capability mitigates the target grating null at $\theta_i = 71.8°$. The after-curve (solid line) result illustrates this effect. Apart from maximizing the null in the desired signal direction, the voltage pattern in the "after" case has lower relative gain on average compared to the "before" case. This is an interesting result, since previous scenarios (e.g., using dipole element patters) have illustrated poor overall pattern performance when evaluated at the grating null angle.

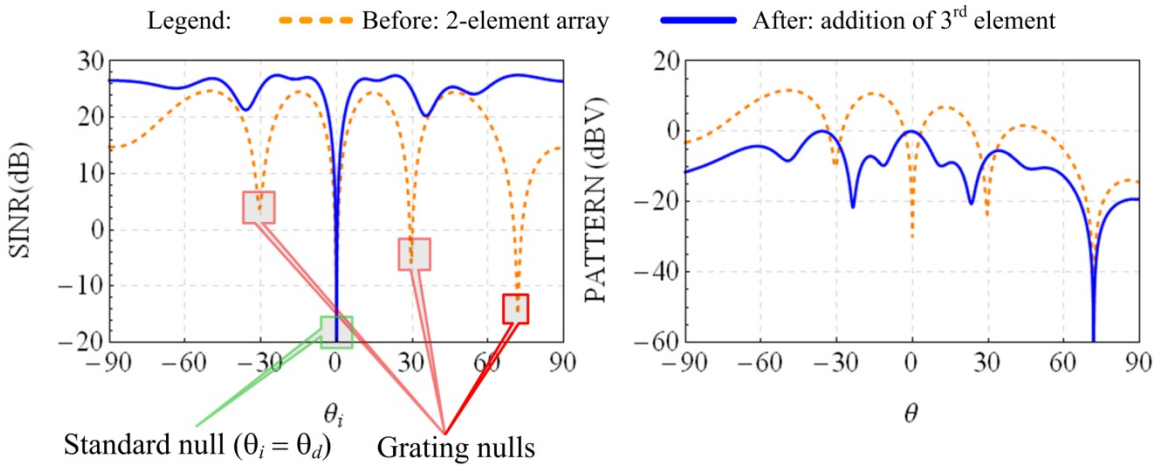

Figure 4-11: Resulting SINR (left) and voltage pattern plot (right) in a Type II GN scenario with the following parameters: $\theta_d = 0°$, $d_2 = 2\lambda_0$, $\theta_{n1} = -45°$, $\theta_{n2} = -30°$, $\theta_i = \theta_{gn2} = -71.8°$, $\theta_{n3} = -9.6°$, and $d_3 = 3.5\lambda_0$. The dashed light curve represents the two-element array and the solid dark curve represents the addition of the third element. The graphs show how SINR performance improves with pattern variability.

4.4 The No Solution Case: Further Discussion

The NS (no solution) results listed in Table 4-1 and Table 4-2 warrant further discussion. Recall that they occur when the beam tilt required for the third element to mitigate the grating null effect is outside the visible range and thus does not exist. Examining the condition that determines θ_{n3} from another perspective can perhaps give more insight into the matter. Take, for example, the relationship in (3.10). Incorporating the dipole pattern given in (3.9), it can be expressed algebraically in a form described by $\theta_{n3} = \cos^{-1}(x)$. The argument x functionally represents the following variables: θ_d, θ_i, θ_{n1}, θ_{n2}, and d_2. The full θ_{n3} expression can be written in two similar general forms, each given as

$$\theta_{n3} = \pm\cos^{-1}\left[\pm\sqrt{\frac{X^2 + 2(B-A)(B+Y) \pm \sqrt{X^2\left[X^2 - 4(A+Y)(Y+B)\right]}}{2\left[(A-B)^2 + X^2\right]}}\right] \qquad (3.16)$$

and

$$\theta_{n3} = \pm\cos^{-1}\left[\pm\sqrt{\frac{X^2 + 2(B-A)(B-Y) \pm \sqrt{X^2\left[X^2 - 4(A+Y)(Y-B)\right]}}{2\left[(A-B)^2 + X^2\right]}}\right], \quad (3.17)$$

where in each expression $A = \cos\theta_d \cos\theta_i$, $B = \sin\theta_d \sin\theta_i$, X=$\sin\theta_d \sin\theta_i$, and $Y = \left|\cos(\theta_d - \theta_n)\cos(\theta_i - \theta_n)\left(1 + \exp\left[\, j2\pi d_2(\sin(\theta_d - \theta_i)\right]\right)\right|$ for $\theta_{n1} = \theta_{n2} = \theta_n$ (i.e., elements one and two having identical beam tilts). The expressions in (3.16) and (3.17) offer 16 possible solutions for θ_{n3} (most of which are extraneous) that can cause the NS results. Restricting the observation and solution space makes deciphering the results easier.

Consider the pair of plots in Figure 4-12. Each graphic plots the real (solid blue curve) and imaginary part (dashed orange curve) of the relationship described by (3.16) and (3.17) in degrees versus θ_{n1} and θ_{n2}, the beam tilt of the first and second elements, which are here assumed equal (i.e., a CGN scenario). Both θ_{n1} and θ_{n2} are designated as just θ_n (horizontal axis). Reducing the observation space in order to simplify the analysis, let θ_n vary from –60° to 60° in each plot. In (a), let θ_d = –15°, $\theta_i = \theta_{CGN}$ = 14.0°, and $d_2 = 2\lambda_0$, while in (b) let θ_d = –45°, $\theta_i = \theta_{CGN}$ = 52.46°, and $d_2 = 2\lambda_0$. The curves illustrate the regions of NS that exist for the given parameters as a function of beam tilt angle. When the imaginary part of θ_{n3} equates to 0, a real-valued beam tilt exists. As the plot dictates, within this region, the value of θ_{n3} varies.

To gain further insight from another point of view, take note of Figure 4-13, which shows once again θ_{n3} vs. θ_n. The plots display the real values of θ_{n3} that only exist when θ_d = –15° and $d_2 = 2\lambda_0$ for all three grating nulls that exist. Each curve within the plot corresponds to the θ_{n3} value for each individual grating null (see the legend within the plot). The gaps between like curves dictate beamsteering angles where a NS result occurs. Moreover, each curve carries with it directional arrows and/or vertical hash marks. The arrows along with the numerical value signify the corresponding distance of the third element, d_3, for all points indicated by the arrow directions. The curves bring to light not only the NS regions but also, for the solutions that do exist, regions of continuity

for d_3. In some cases, (e.g., $\theta_{CGN} = -49.4°$), an inflection point exists where the value of d_3 goes from $3.0\lambda_0$ to $4.0\lambda_0$. The next subsection discusses this particular result in further detail. Overall, the analysis demonstrates the behavioral existence of the third-element parameters, (θ_{n3}, d_3), required to mitigate grating nulls. The results provide valuable information regarding array design considerations and suggest steps toward alleviating the grating null effect.

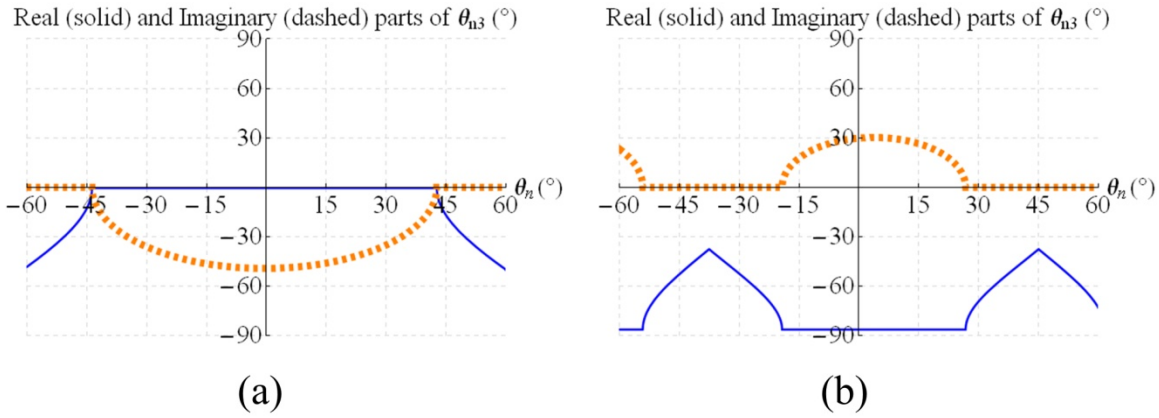

Figure 4-12: Graphs illustrating the real part (solid blue curve) and imaginary part (dashed orange curve) of the θ_{n3} needed to mitigate the grating null vs. θ_n, the beam tilts of both elements in the 2-element array (CGN scenario). Regional areas of NS exist only when the imaginary part is not equal to 0. In case (a), $\theta_d = -15°$, $\theta_i = \theta_{CGN} = 14.0°$, and $d_2 = 2\lambda_0$. In (b), $\theta_d = -45°$, $\theta_i = \theta_{CGN} = 52.46°$, and $d_2 = 2\lambda_0$.

4.5 Non-Uniformity in Spacing: Further Discussion

As with the NS result, the spacing of the third element (d_3) also necessitates further discussion. Throughout the calculated results, there were examples in which the spacing of the third element departed from a uniformly spaced array (i.e., $d_3 \neq 4.0\lambda_0$). Figure 4-13 clearly demonstrates this fact by displaying solution curves in regions where $d_3 \neq 4.0\lambda_0$. Thus, it seems as though the applied technique pushes for a solution in which the array geometry is nonuniformly spaced. As indicated in [18], employing non-uniform spacing does indeed present an alternative method to GN mitigation, essentially disrupting the periodicity of the array structure. Thus, the question of interest lies in how

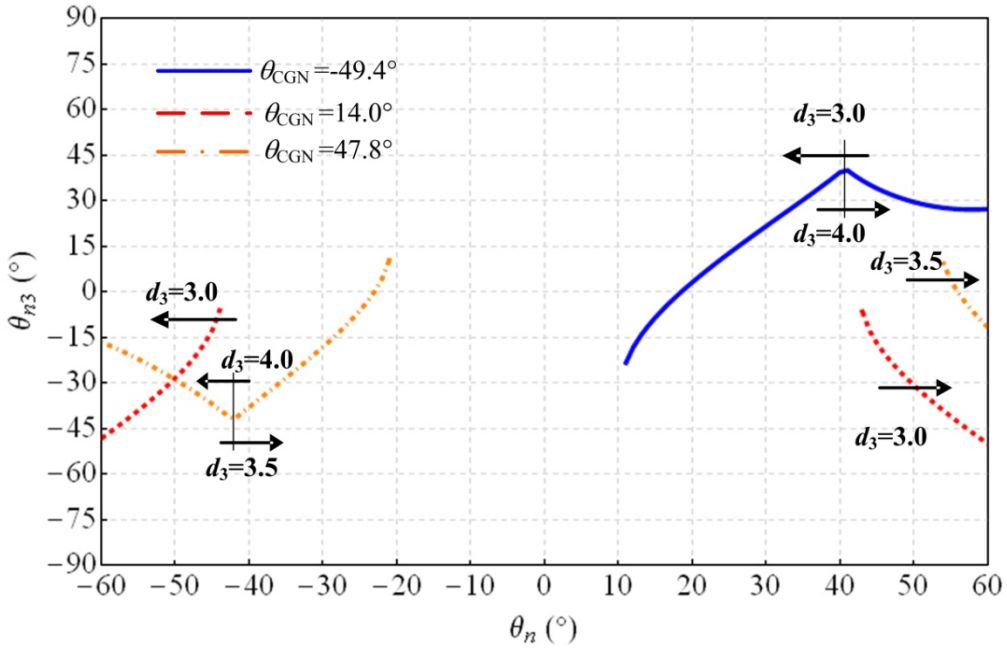

Figure 4-13: Graph illustrating θ_{n3} vs. θ_n; the solution regions that exist for a CGN scenario in which θ_d = –15°, and $d_2 = 2\lambda_0$. The corresponding grating nulls exist at θ_{CGN} = –49.4°, –14.0°, and 47.8°, as indicated by the plot legend. Apart from the NS regions, the directional arrows indicate regions of continuity for d_3 in units of wavelengths.

this type of structure (i.e., a subset of aperiodic arrays) matches the current methodology of utilizing the pattern only to mitigate GNs. However, there exist some practical disadvantages with this line of thinking in the context of this work.

Due to their aperiodic spacing functions, aperiodic arrays with a large number of elements in general have no grating lobes (i.e., grating nulls). They are mostly utilized in array thinning, beamwidth narrowing, and element-interaction reduction applications [32]. One of the main objectives in this type of array synthesis problem is to find an optimum set of element spacings and excitations that would minimize the highest sidelobe level in the entire visible region. However, [32] reports that the difficulty in solving the problem lies in the fact the sidelobe levels depend on the element spacings in a highly nonlinear manner. Therefore, non-uniformly spaced arrays would not be applicable to adaptive arrays because (1) overall low sidelobe levels are not the priority and (2) it is impractical to physically change element positions in order to adapt to an ever-changing signal environment. Pattern reconfigurability offers a solution to the

grating null solution in a more practical way by employing a uniformly spaced array structure.

4.6 Chapter Summary

This chapter presented a variety of graphic analyses involving numerous adaptive array scenarios. The results were based on the analytical adaptive array methodologies outlined in Chapter 3. After graphically illustrating the occurrence of different types of grating nulls, SINR and pattern plots displayed the effectiveness of pattern reconfigurability to mitigate grating nulls. Section 4.3 implemented the RMPA radiation patterns into the adaptive array methodologies. The outcome of this implementation confirms that a practical pattern reconfigurable element can produce results comparable to those of the model dipole element. The final two sections discussed some of the byproducts of this implementation, namely the NS result and emerging cases of non-uniform element spacing. The analysis provided further insight into the behavior of solution parameters for the third element.

CHAPTER 5
NULL RECONFIGURABILITY

Thus far, this research has illustrated one aspect of the functional benefits of utilizing radiation reconfigurable antennas with beam tilts in an adaptive array setting. The results demonstrate how performance potential increases with the inclusion of pattern variability using the adopted array technique. However, the methodology only specifies the requirements of the additional third reconfigurable element's properties based on prior knowledge of the original array elements. This in turn can lead to a limited possible solution space; the discussion in Section 4.4 explains this point in terms of the no solution result. Therefore, the focus of the dissertation turns to fully leveraging the capabilities of the available pattern reconfigurability by integrating pattern variability directly into an algorithm. In this way, the methodology is more systematic in its approach by allowing the algorithm itself to determine the range of possible solutions and antenna configurations.

A previous study [33] explored the performance benefits and tradeoffs in utilizing a linear equally spaced array composed of radiation reconfigurable antennas. The premise of the work focused on the effects of reconfigurability on sidelobe level, gain, and excitation dynamic range of amplitude-tapered linear phased arrays. Array pattern comparisons were made between fixed-pattern broadside antenna elements and elements with tilted radiation patterns (e.g., those represented by the RMPA). The results demonstrate that tilting all the pattern reconfigurable antenna elements in the direction of the steered main beam's direction adds additional array pattern gain compared to an array composed of fixed-pattern elements. A tradeoff in gain can then be applied in reducing the excitation dynamic range of an applied amplitude taper [33].

This chapter considers the potential use for radiation reconfigurable antennas in a way such that the benefits addressed in [33] are applicable in an adaptive array setting. The results will demonstrate that the advantages gained in pattern variability can stem not only from the antenna's beam tilting capability but also from its null-forming ability as

well. These simple, but illustrative examples lay the foundation for the algorithm integration and continue along the line of this dissertation's research objectives.

5.1 Overview and Methodology

Thus far, the implementation of pattern reconfigurable antennas has focused on tilting the maximum of the main beam in a specified direction. Certainly this characteristic of the antenna's element pattern can be of great importance to the functionality of the system. However, just as important may be the null (or depression) the pattern reconfigurable antenna can offer in a specified direction apart from the pattern's maximum. Hence, the notion of pattern variability includes all the distinct features within the antenna element's capabilities.

In order to illustrate some of the advantages, consider a scenario that has an adaptive array composed of isotropic elements (such benchmark elements are commonly used in the literature [17]) and an array composed of pattern reconfigurable antennas that have a specified maximum and null. To simplify the analysis, model these elements using a tilted dipole element of the cosine variety, essentially those represented by (3.9) in Section 3.5, where the main beam maximum resides at θ_{nj}, with $\theta_{nj} = 0^{\circ}$ corresponding to broadside and a pair of nulls residing at $\theta_{nj} \pm 90°$.

The basic constituents of the analysis involve evaluating the adaptive array specific parameters in a static state utilizing the general adaptive array concepts presented by Compton in [17]. Comparisons between results are made for the isotropic array and the model reconfigurable antenna (RCFG) array for three different cases. In each case, the constants consist of the arrays having $N = 5$ elements spaced $d = 1\lambda_0$ apart, a strong interference environment (i.e., interference-to-noise ratio (INR) equal to 40 dB), and the signal-to-interference ratio (SNR) equal to 0 dB. Also, in the reconfigurable antenna array, let all element beam tilts, θ_{nj}, be identical (i.e., all the elements tilt their main beam maximum according to a single parameter, θ_n; the element pattern null tilts accordingly). The varying parameters in each case include the signal environment (θ_d and θ_i) and the pattern reconfigurable antenna beam/null tilting parameter, θ_n. Finally, the SINR (dB),

voltage pattern (dB), and element weight profile (magnitude and phase) plots are given for each case in the next section.

5.2 Case Study Results

Table 5-1 lists the parameters involved with the two case scenarios. In Case 1 the beam tilts are not directed toward the desired signal ($\theta_n \neq \theta_d$) and the interference signal falls into the null of the model RCFG pattern ($\theta_n = \theta_i + 90°$). In Case 2, the characteristics resembles Case 1, but now the interference signal falls into a grating null (GN) ($\theta_n \neq \theta_d$, $\theta_n = \theta_i + 90°$, and $\theta_i = \theta_{GN}$). Case 1, represents a scenario when the RCFG can steer its pattern null into the direction of the interference source but may not necessarily be able to line up the main beam of the pattern along the desired signal direction. Case 2 presents a similar situation such that the RCFG's element pattern nulls out the interference signal; but at this occurrence, the interference signal happens to be coming from the grating null direction. Again, the isotropic array, which solely relies on its array factor, serves as a comparison basis.

Table 5-1: Listing of the signal environment parameters and direction of the beam tilts for the model pattern reconfigurable element. Note, the element null lies at $\theta_n - 90^\circ$.

Case	θ_d (°)	θ_n (°)	θ_i (°)	θ_{GN} (°)
1	**25**	45	–45	**–35**
2	45	**73**	**–17**	–17

Figure 5-1 and Figure 5-2 depict the results of the case studies listed in Table 5-1. In each case, the first column of plots represents once again the SINR versus θ_i, and the radiation pattern versus θ, using isotropic elements. Similarly, the second column presents the same but utilizing the model RCFG elements. The third column shows a magnitude and phase weight profile computed by the adaptive array LMS algorithm for both types of antenna elements.

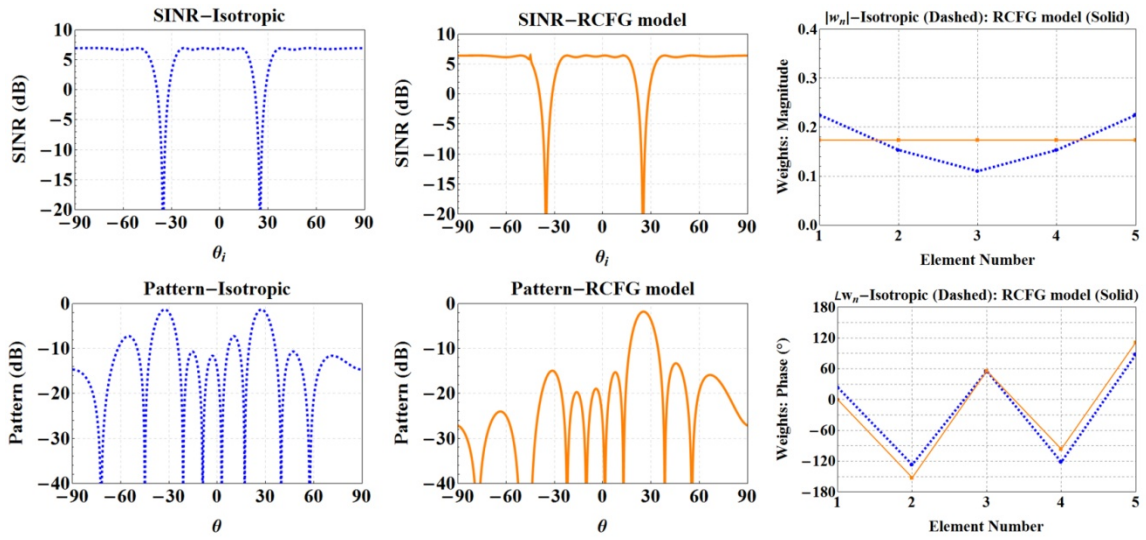

Figure 5-1: Adaptive array results (SINR, pattern, and weight profile) comparing an array composed of isotropic elements (dashed curves) to an array of model pattern reconfigurable elements (solid curves). The parameters of operation are indicated for Case 1 in Table 5-1.

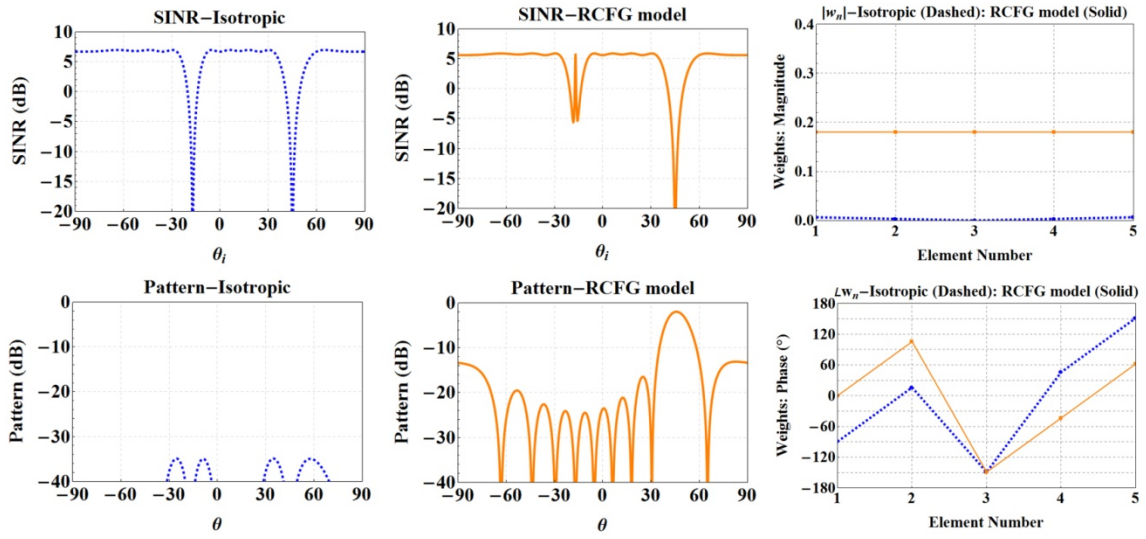

Figure 5-2: Adaptive array results (SINR, pattern, and weight profile) comparing an array composed of isotropic elements (dashed curves) to an array of model pattern reconfigurable elements (solid curves). The parameters of operation are indicated for Case 2 in Table 5-1.

The results for Case 1 (Figure 5-1) show how the adaptive algorithm adjusts the weights to place a null in the pattern at $\theta = -45°$ and steers the overall pattern main beam to $\theta = 25°$, the incoming direction of the desired signal. However, the individual beam

tilts of the reconfigurable antenna elements are not directed toward the desired signal. The effect amounts to about 1 dB of loss in maximum SINR of the RCFG plot in comparison to the isotropic plot, essentially a scan loss effect from the beam tilt directions. Due to the null in the element factor, the RCFG array depicts an overall pattern with lower sidelobe levels compared to the isotropic array results. Unlike the isotropic array, having the interferer fall into the null of the element pattern allows the adaptive processor to manufacture weights with a uniform amplitude distribution and progressive phase—a result predicated upon being able to direct the nulls of the elements in the direction of the interferer.

Case 2 (Figure 5-2) considers the situation when the interference signal falls into the grating null (θ_{GN} at $\theta_i = -17°$), which is no doubt an undesirable result as shown by the isotropic array pattern and weight plots. Since the interference signal falls into the grating null, the pattern suffers with values less than –30 dB. The source of the problem lies in the magnitude of the weights, which are effectively zero for each element. The adaptive algorithm in conjunction with the isotropic elements has no way of dealing with the interference signal coming from this direction, thus it resorts to basically shutting down the array by zeroing out the weights. One way to deal with this problem is to configure the null of the reconfigurable antenna patterns along the same direction as the grating null (i.e., $\theta_n = \theta_{GN} + 90° = 73°$). Doing this allows grating null alleviation in the SINR plot and again produces a desirable weight profile: a uniform amplitude and a progressive phase distribution.

5.3 Discussion

The work presented in Chapter 3 and Chapter 4 centered on using pattern variability in conjunction with elements that can reconfigure their main beam to a prescribed spatial direction. In this chapter, the analysis evaluated pattern variability in terms of null reconfiguration, which, as seen in Case 2, provides an alternative approach for grating null mitigation. Overall, the results demonstrate the potential of null reconfigurability when used in an adaptive array setting. Despite the fact that the dipole model represents an ideal element, it presents a starting point and provides an indication

of what characteristics practical radiation reconfigurable antennas must possess in small adaptive array scenarios.

In practice, the method could have significant implications in reducing constraints on the adaptive hardware components. For example, by effectively capturing the null at the front end via the antenna's nulling capability, the analog-to-digital converters inside the adaptive array processor do not have to work as hard. Depending on the threat, an impinging jamming signal can have a very large INR, which could surpass the dynamic range of the analog-to-digital converters. This in turn makes it difficult for the adaptive processor to null out the interferer at the array output since it accomplishes this task by subtracting two or more of these signals from each other. Null reconfigurability effectively alleviates this issue because the pattern null minimizes the unwanted signal at the front end, independent of the interference signal's amplitude.

CHAPTER 6
PATTERN VARIABILITY INTEGRATION

The preceding analysis in Chapter 5 set forth the concept and potential benefits in utilizing null reconfigurability in an adaptive array setting. However, the method requires the reconfigurable solutions in a forward manner—forward in the sense that the beam tilt and null directions of the reconfigurable array elements are selected *a priori* based on the signal environment. A more powerful approach would involve determining the characteristics of the reconfigurable element patterns in a reverse manner (i.e., inherently synthesizing the patterns). Therefore, in continuing with the idea to fully leverage the capabilities of the available reconfigurability, this chapter discusses a method that integrates pattern variability into the adaptive array algorithm. This method presents a more systematic approach in which the algorithm itself then determines the range of possible solutions and, hence, specifies antenna element reconfigurability.

This chapter first presents the salient points behind the adopted routine and then discusses the framework behind incorporating the reconfigurable antenna (RCFG) element into the routine. The next section discusses the configuration details behind each of the example operational scenarios involved in the analysis followed by graphs pertaining to each scenario and a discussion of the findings. A thorough discussion summarizing the results will conclude this chapter.

6.1 Convex Optimization Routine Description

This section gives a general overview of the optimization routine utilized in this work. The discussion outlines the technical details that will be applied in future sections to the pattern variability problem. In [22,23], the authors present a method of finding the optimum sidelobe-minimizing weights for an arbitrary linear array that holds for any scan direction, beamwidth, set of pattern nulls, and type of antenna element used. The array problem is presented in convex form and thus can be cast into a convex optimization problem with various constraints. In this form, the algorithm does not have to search

through the entire weight space, making the problem rapidly solvable in a straightforward manner. Additionally, due to the characteristics of the convex functions, the solutions are guaranteed to be globally optimum [22]. Apart from these features, the routine is of interest to the research because of its ability to incorporate additional weight constraints. Utilizing this degree of freedom gives the research the means to integrate pattern variability directly into the optimization process.

The principal components of the convex routine include the following (see [22,23] for further details). For the total radiation pattern of an *N*-element linear array along the *z*-axis, the relationship can be expressed in typical form as a function of the element weight vector ($\mathbf{w}$) and spatial angle θ given by

$$T(\mathbf{w},\theta) = \sum_{n=1}^{N} w_n f_n(\theta) \exp[j \frac{2\pi}{\lambda_0} d_n \cos\theta], \tag{5.1}$$

where w_n are the weights attached to *n*th element, $f_n(\theta)$ is the each element's radiation pattern, d_n is the linear distance of each element from the reference location, and λ_0 is the free space wavelength at the operational frequency. Note that in this case the array geometry is set up such that broadside is at $\theta = 90°$. In the analysis, the element spacing is kept uniform, even though the routine allows for arbitrary element spacing. The reason for this stems from the original array topology objectives and some of the impracticalities involved with non-uniform spacing in adaptive array applications that were discussed earlier.

The task of finding the optimum sidelobe-level minimizing weights is a solution to the optimization problem given by

$$\min_{\mathbf{w} \in C^N} \left\{ \max_{\theta \in \Theta} \left| T(\mathbf{w},\theta) \right| \right\}$$
$$\text{subject to} \left\{ \begin{array}{c} T(\mathbf{w},\theta_d) = 1 \\ \frac{d}{d\theta} \mathrm{Re}\{T(\mathbf{w},\theta_d)\} = 0 \\ T(\mathbf{w},\theta_i) = 0, \;\; i = 1,2,....,K \end{array} \right\}. \tag{5.2}$$

The components of (5.2) require further detailed discussion. The objective function is the sidelobe level (SLL), since it represents the spatial region of the radiation pattern outside the main beam. It is desired to minimize the maximum value of this function in that spatial region outside the main beam (denoted by Θ) subject to the listed constraints. As a result, the problem becomes a minimax optimization problem and the task amounts to determining the set of all N-element weight vectors with complex components, denoted by C^N, that suppress the SLL region. Furthermore, the constraints at θ_d require that the normalized radiation pattern be equal to unity and that the magnitude of the total radiation pattern is maximum; K specifies the number of nulls at an angle θ_i [22].

In order to formulate the problem into convex form, [22] writes the element weights and total radiation pattern given by (5.1) in terms of their real and imaginary parts, i.e.,

$$\begin{aligned} w_n &= w_n^{RE} + jw_n^{IM} \\ T(\mathbf{w},\theta) &= \mathrm{Re}\{T(\mathbf{w},\theta)\} + j\,\mathrm{Im}\{T(\mathbf{w},\theta)\}, \end{aligned} \tag{5.3}$$

respectively. To minimize the SLL, the next step requires partitioning Θ into M discrete sample points ($1 \le m \le M$, m is an integer), each of which is called a suppression point. Thus, a suppression point will minimize the magnitude of the total radiation pattern at a fixed position θ_m. Taking into account all suppression points, the multi-objective optimization problem can be written in compact minimax form given by

$$\begin{aligned} &\min \max_{m=1,\ldots,M} \quad t_m^2 + s_m^2 \\ &\text{subject to } \begin{Bmatrix} AX \le 0 \\ BX = 0 \end{Bmatrix}. \end{aligned} \tag{5.4}$$

In (5.4), there exist a total M objective functions, $t_m^2 + s_m^2$, one corresponding to each suppression point. They act like dummy variables and represent the radiation pattern in conjunction with the constraints. Matrices A and B contain the linear inequality and linear equality constraints, respectively, and 0 is a vector of zeros. Finally, the vector X

contains the unknowns variables: the weight variables and all the dummy variables. Specifically, the variable components of *X* resemble the listing given by

$$X^T = \left[w_1^{RE} \; w_1^{IM} \; w_2^{RE} \; w_2^{IM} \; ..... \; w_N^{RE} \; w_N^{IM} \; t_1 \; s_1 \; t_2 \; s_2 \; ..... \; t_M \; s_M \right]. \tag{5.5}$$

The convex nature of the routine stems from the form of the objective functions, $t_m^2 + s_m^2$, and thus it minimizes the array factor at all desired suppression points. Since the constraints are written as a matrix set of linear equalities and inequalities, the *fminimax* function in MATLAB® offers one of many ways to solve the problem. Note that the adaptive array concept still applies here because the goal of placing a maximum along the desired signal direction and placing a null along the interference direction does not change, which effectively enhances the SINR.

6.2 Reconfigurable Model Integration

With a much better understanding of technical details driving the convex optimization routine, this work next turns to implementing model reconfigurable antennas into the procedure. Utilizing this approach allows the optimization process to select the best set of solutions, giving insight into the needed elements of reconfigurability for small adaptive array scenarios.

6.2.1 Subarray Model Description

Given the fact that the routine sets forth the weight vector $\vec{w}$ as the unknown solution vector (its real and imaginary parts), the method of interest models each individual pattern RCFG element as a subarray of isotropic elements for the full *N*-element array. In particular, a single reconfigurable element is modeled as a two-element array. As discussed in [2], subarrays exist as an array architecture design technique, residing at the aperture level, which dictates how array elements are to be grouped and fed. Due to cost concerns, their primary use resides in applications utilizing a uniform illumination. Apart from these implementation benefits, this model is chosen because each individual subarray can carry its own unique pattern in terms of the location of its

main beam maximum and null location(s). These are the two main radiation reconfigurable pattern characteristics the research seeks to characterize. The goal is to integrate the subarray model into the optimization routine and have the routine output solutions portraying these individual pattern traits—traits that can then be used as specifications for pattern reconfigurable antennas.

Figure 6-1 illustrates an example array geometry that includes a group of two-element subarrays; each two-element subarray will represent each individual pattern RCFG element (a discussion on why two elements were chosen follows toward the end of this section). In reference to Figure 6-1, d_{sub} represents the distance between each subarray element and d_{Main} represents the distance between each subarray (i.e., RCFG element). In this work, d_{sub} is identical for all subarrays. Note that the complex weight w_n is attached to each individual element in the array.

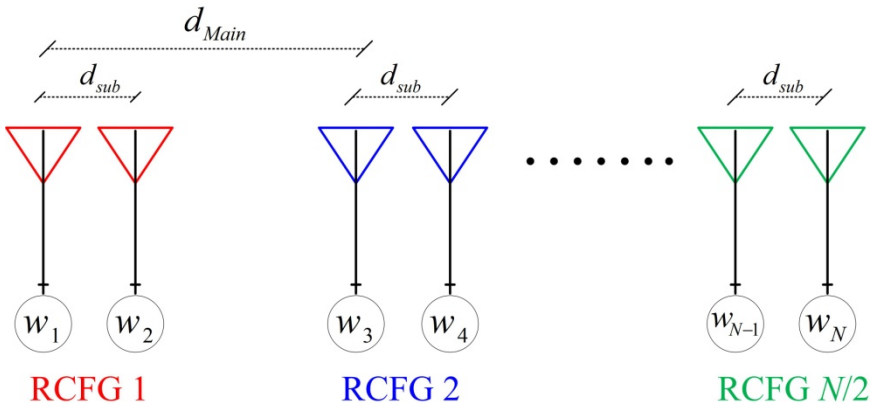

Figure 6-1: Diagram showing the array geometries utilized in the optimization routine. The array consists of $N/2$ subarrays (spaced d_{Main} apart); each models a pattern RCFG element and contains two isotropic elements, spaced d_{sub} apart.

For reasons that will become apparent later, a simple analysis on an individual subarray element is in order. Figure 6-2 shows a single subarray in a two-dimensional geometry configured in a symmetrical fashion. Note how element 1 (the first element in the subarray) is deemed the n^{th} element with weight w_n while element 2 is labeled the n^{th} +1 element with weight w_{n+1}; references to the first element of the subarray with w_n will be used throughout the rest of this work. Assuming that the first and second model

element in each subarray is isotropic, then (5.1) prescribes the radiation pattern for a single subarray as

$$T_{sub}(\theta) = w_n e^{-jk\frac{d}{2}\cos\theta} + w_{n+1} e^{jk\frac{d}{2}\cos\theta}. \tag{5.6}$$

Given the optimized weights, the total pattern can be recovered in terms of subarrays (RCFG elements) utilizing array theory. In this case, the subarray patterns become effectively single elements; summing each with the appropriate spatial phase shift gives the total pattern of the full array. In reference to Figure 6-1, the total pattern can be expressed as

$$T_{total}(\theta) = \sum_{n=1}^{N/2} T_{sub_n}(\theta) e^{jk(n-1)d_{Main}}, \tag{5.7}$$

where T_{sub_n} is the n^{th} subarray pattern denoted by (5.6). Also, note the summation goes from $n = 1$ to $N/2$ (the number of RCFG elements).

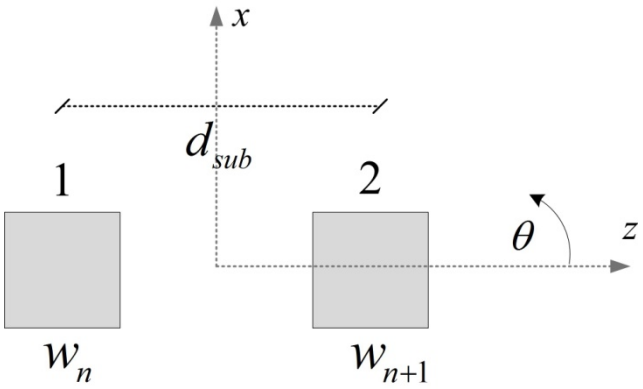

Figure 6-2: Geometry of a single 2-element subarray spaced d_{sub} apart.

6.2.2 Additional Constraint Implementation

Due to the flexibility of implementing constraints within the convex optimization routine, the next step involves applying additional constraints on the weights of each subarray. The constraints should address practical implementation concerns when associating the subarray elements to pattern reconfigurable antenna elements. In addition

to the constraints imposed on the element weights via the optimization routine, as indicated in (5.4), the methodology imposes two additional linear constraints on the weights: (1) a complex conjugate constraint and (2) a beam tilt (beamsteer) constraint. The following subsections describe each constraint in more detail.

6.2.2.1 Complex conjugate constraint

The complex conjugate (CC) constraint forces the pair of weights in each subarray to be complex conjugates of each other. Mathematically, this equates to each individual subarray having $w_{n+1} = w_n^*$. Furthermore, in terms of the full *N*-element array, the conditions applies for n = 1, 3, 5, …, N-1 (i.e., odd numbered elements). An alternative and more relevant translation equates to having $w_{n+1}^{RE} = w_n^{RE}$ and $w_{n+1}^{IM} = -w_n^{IM}$, i.e., identical real parts and opposite (in sign) imaginary parts of the subarrray weight pair. The routine's flexibility allows for implementation of these constraints; they can be added into the equality matrix in (5.4) along with those imposed by the routine by itself. For example, for the weights of a single subarray element, the equality can be expressed in matrix form as

$$\begin{pmatrix} 1 & 0 & -1 & 0 \\ 0 & 1 & 0 & 1 \end{pmatrix} \begin{pmatrix} w_n^{RE} \\ w_n^{IM} \\ w_{n+1}^{RE} \\ w_{n+1}^{IM} \end{pmatrix} = \begin{pmatrix} 0 \\ 0 \end{pmatrix}. \tag{5.8}$$

The importance for imposing this constraint stems from modeling the pattern RCFG elements as individual subarrays. In addition to the previous discussion, the constraint also forces the weights in each subarray to have identical magnitudes and opposite phases. It would be complicated to model the RCFG element in terms of beam tilts (main beam maximums) without having identical weight magnitudes. In the opposite case, main beam maximums are not well defined. As previously discussed, subarrays are primarily used when utilizing a uniform illumination; the complex conjugate constraint realizes this characteristic and thus will assist in associating the subarray model patterns to the RCFG elements' patterns.

On the other hand, incorporating this type of constraint limits the number of array elements in the subarray to two. Adding more elements reduces the subarray pattern's beam width (increasing directivity) and increases the number of pattern nulls. A more directive beam may or may not better represent a practical reconfigurable antenna's radiation pattern. However, as discussed, a well-defined beam tilt exists when all the elements in the subarray have identical magnitudes and some sort of progressive phasing. Under the guidelines, it becomes more difficult to institute a linear constraint relationship (i.e., a linear equality) in the routine with more than two elements. The functionality of the routine thrives on the constrain matrices being written in linear equality/inequality form. Without this attribute, the routine will not be able to freely select the desired pattern characteristics (e.g., beam tilt angle) based on the weight constraints.

6.2.2.2 Beamsteering constraint

The beamsteering (BS) constraint, in conjunction with the complex conjugate constraint, addresses practical limitations on a pattern reconfigurable antenna's beamsteering range. Analogous to the difficulties phased arrays encounter when steering toward endfire (e.g., scan loss, beam broadening, etc.), pattern reconfigurable antennas also encounter pattern degrading effects when trying to tilt the pattern close to endfire. Trying to cover a large scan range makes the design very difficult, if not impossible, for a single radiating element. Therefore, the beamsteering constraint places a limitation on the spatial location of the allowable main beam maximum (beam tilt angle) for each subarray. Defining the beamsteering angle for each subarray as $\theta_{substeer}$, then let the upper limit be θ_{upper} and the lower limit as θ_{lower}. For convenience, with broadside at $\theta = 90°$, restrict the upper and lower limits to $0° \le \theta_{lower} \le 90°$ and $90° \le \theta_{upper} \le 180°$. Then, the beamsteering constraint essentially restricts $\theta_{substeer}$ to $\theta_{lower} \le \theta_{substeer} \le \theta_{upper}$. A detailed derivation describing how this constraint is invoked into the optimization routine follows.

Utilizing (5.6) in conjunction with the underlying conditions, the beamsteering constraints can be formulated in a way adaptable to the optimization program. With the complex conjugate constraint (5.6) can be expressed as

$$
\begin{aligned}
T_{sub}(\theta) &= w_n e^{-jk\frac{d_{sub}}{2}\cos\theta} + w_n^* e^{jk\frac{d_{sub}}{2}\cos\theta} \\
&= |w_n| \left(e^{-j\left(k\frac{d_{sub}}{2}\cos\theta - \angle w_n\right)} + e^{j\left(k\frac{d_{sub}}{2}\cos\theta - \angle w_n\right)} \right) \\
&= 2|w_n| \cos\left(k\frac{d_{sub}}{2}\cos\theta - \angle w_n \right).
\end{aligned}
\tag{5.9}
$$

From the expression, let the maximum (i.e., the beam tilt) of $T_{sub}(\theta)$ occur at $|T_{sub}(\theta = \theta_{\max})|$, where $\theta_{\max} = \theta_{substeer}$. This happens when

$$
\begin{aligned}
& k\frac{d_{sub}}{2}\cos\theta_{substeer} - \angle w_n = m\pi, \quad m \in \text{Integer} \\
\Rightarrow \qquad & \cos\theta_{substeer} = \frac{2\left(\angle w_n + m\pi\right)}{kd_{sub}}.
\end{aligned}
\tag{5.10}
$$

Using the bound restriction, $\theta_{lower} \le \theta_{substeer} \le \theta_{upper}$, the constraint limits in terms of the weights can be derived as

$$
\begin{aligned}
& \cos\theta_{lower} \le \frac{2\left(\angle w_n + m\pi\right)}{kd_{sub}} \le \cos\theta_{upper} \\
& \frac{kd_{sub}}{2}\cos\theta_{lower} - m\pi \le \angle w_n \le \frac{kd_{sub}}{2}\cos\theta_{upper} \\
& \frac{kd_{sub}}{2}\cos\theta_{lower} - m\pi \le \tan^{-1}\left(\frac{w_n^{IM}}{w_n^{RE}}\right) \le \frac{kd_{sub}}{2}\cos\theta_{upper} \\
& w_n^{RE}\tan\left(\frac{kd_{sub}}{2}\cos\theta_{lower}\right) \le w_n^{IM} \le w_n^{RE}\tan\left(\frac{kd_{sub}}{2}\cos\theta_{upper}\right).
\end{aligned}
$$

Given the restrictions on the upper and lower limits themselves, the pair of linear inequality constraints exist as

$$
\begin{aligned}
&1. \quad w_n^{IM} \le -w_n^{RE} \tan\left(\frac{kd_{sub}}{2}\left|\cos\theta_{upper}\right|\right) \\
&2. \quad w_n^{IM} \ge w_n^{RE} \tan\left(\frac{kd_{sub}}{2}\cos\theta_{lower}\right).
\end{aligned}
\tag{5.11}
$$

As in the equality constraint cases, they are incorporated into the routine in matrix inequality form.

It is instructive to graphically analyze the constraints given by (5.11). Consider Figure 6-3, which shows the region of constraint in terms of the w_n plane (the real and imaginary parts of w_n). For demonstration purposes, let $\theta_{lower} = 60°$ and $\theta_{upper} = 120°$. The figure shows the regions satisfied by Constraint 1 in (5.11), indicated by the dark-tiled grey shade, and the constraint region satisfied by Constraint 2 by bright orange. The dark orange region on the left, bounded by the red triangle, represents the overall constraint region as the intersection of the two individual equalities, marked by the direction of the larger arrows. As θ_{upper} increases and θ_{lower} decreases, the overlap region grows larger, thus giving the optimization routine a wider pool of beam tilts from which to choose when solving the array problem.

The linear equalities in (5.11) prescribes a scenario in which $w_n^{RE} \le 0$; Figure 6-3 illustrates this scenario graphically. It turns out the region occupied by the white triangle on the right is also a valid beamsteering solution due to the result in (5.10). Since this triangular region also serves as a potential beamsteering solution, the imposed constraints can be determined by inspection. They become

$$
\begin{aligned}
&3. \quad w_n^{IM} \ge -w_n^{RE} \tan\left(\frac{kd_{sub}}{2}\left|\cos\theta_{upper}\right|\right) \\
&4. \quad w_n^{IM} \le w_n^{RE} \tan\left(\frac{kd_{sub}}{2}\cos\theta_{lower}\right).
\end{aligned}
\tag{5.12}
$$

The result in (5.12) corresponds to when $w_n^{RE} \ge 0$, and the inequality pair differs from the pair in (5.11) by essentially an inequality sign flip. Figure 6-4 shows the two solution regions, the $w_n^{RE} \le 0$ case (orange) and the $w_n^{RE} \ge 0$ case (blue), together in graphical

form. Again, to serve as an example, $\theta_{lower} = 60°$ and $\theta_{upper} = 120°$, i.e., the spatial region is set such that the individual beam tilts fall within $\pm 30°$ of broadside $(\theta = 90°)$.

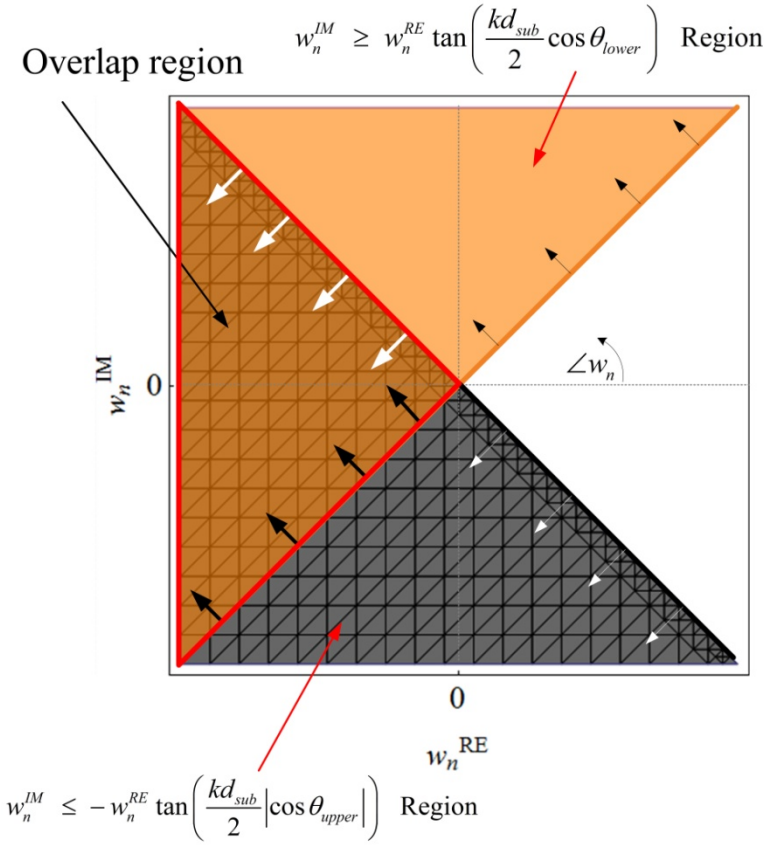

Figure 6-3: Graphic representation of the beamsteering constraint region in the w_n plane. In this case, the two inequalities described by (5.11) are evaluated for $60° \leq \theta_{substeer} \leq 120°$. The optimization routine chooses the solution from the overlap region on the left.

6.3 Convex Optimization Routine: Configuration Details

Before presenting the results, this section outlines the parameters involved in the analysis and discusses the different operational scenarios used in determining the upcoming results. First, it is important to set out the different weight constraints involved for further clarification.

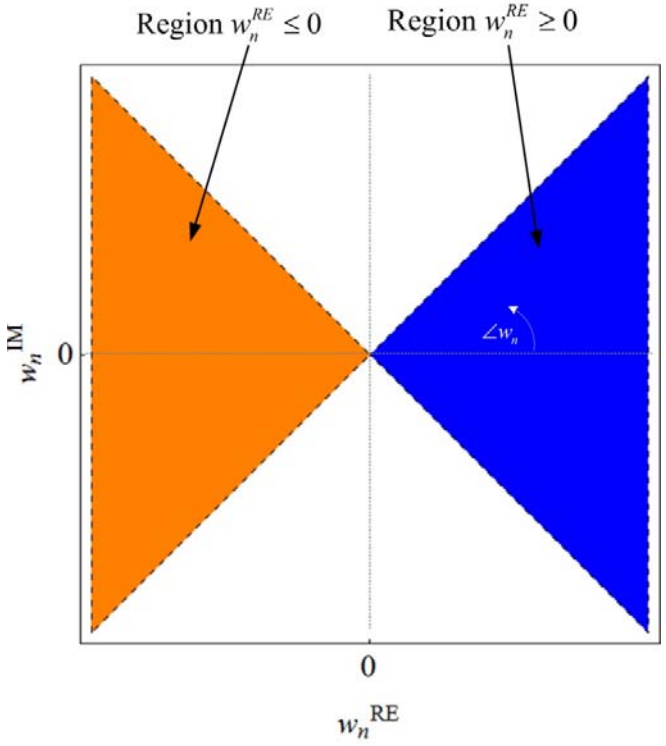

Figure 6-4: Graphic representation of the two beamsteering constraint regions when evaluated for $60° \le \theta_{substeer} \le 120°$ in the w_n plane. The darker blue region on the right restricts solutions such that $w_n^{RE} \ge 0$, and the lighter orange region on the left applies to $w_n^{RE} \le 0$.###

- Weight constraint Case 1: No additional weight constraint. The only constraints imposed on the weights are those prescribed originally by the optimization routine.
- Weight constraint Case 2: Complex conjugate (CC) constraint. The w_n and w_{n+1} weight of each element in each subarray are complex conjugates of each other, i.e., $w_{n+1} = w_n^*$.
- Weight constraint Case 3: Beamsteering constraint (BS) with $w_n^{RE} \le 0$. The allowable beam tilt for each model pattern RCFG element lies between $\pm 30°$ of broadside, i.e., $60° \le \theta_{substeer} \le 120°$.
- Weight constraint Case 4: Beamsteering constraint (BS) with $w_n^{RE} \ge 0$. The allowable beam tilt for each model pattern RCFG element lies between $\pm 30°$ of broadside, i.e., $60° \le \theta_{substeer} \le 120°$.

#

Note how Case 3 and Case 4 characterize the weight constraint in terms of whether the real part of w_n is greater than or less than 0. The ideal situation would be if both constraints were applied simultaneously in a Boolean OR type fashion. However, it turns out that the solving routine, the *fminimax* function in MATLAB, can only apply these constraints in a Boolean AND type configuration, thereby leaving a null solution. Therefore, each of the two constraint cases will be analyzed independently, as indicarted in the last two items in the list. Unfortunately, this will reduce the solution space available to the optimization routine. However, it is informative to analyze the results to gain insight into the potential limiting effects of these contraints.

Each of the constraint cases discussed above will apply to a several operational scenarios, i.e., parameter variation in the signal environment and in the array topology. The goal here is to determine how well the convex optimization routine performs on a case-by-case constraint basis for a prescribed signal environment. The different operational environments include

Scenario 1. The desired signal impinges upon on the array at broadside.

Scenario 2. The desired signal impinges upon on the array off broadside but **within** the beamsteer constraint region.

Scenario 3. The desired signal impinges upon on the array off broadside but **outside** the beamsteer constraint region.

In each scenario, the number of RCFG (subarray) elements equals 5, thus making $N = 10$, $d_{sub} = 0.5\lambda_0$, and $d_{Main} = 1.0\lambda_0$. The parameter definitions of N and d_{Main} comply with the initial goal of having a small number of array elements, each being spaced relatively far apart from each other; the significance of d_{sub} will be discussed shortly. Also, three clustered interference signals at $\theta_i = \{120°, 121°, \text{and } 122°\}$ impinge on the array, and the null-to-null beamwidth is set to 30° (as a comparison, the null-to-null beamwidth of a uniform amplitude broadside array with 10 elements spaced a half-wavelength apart is about 25°). One last note: the m suppression points utilized by the convex optimization

routine to suppress the sidelobe levels will be evenly distributed in 5° increments across the spatial range outside the main beam (denoted by Θ in (5.2)). Recall that the number of suppression points gives the number of objective functions the routine must try and minimize, as discussed in Section 6.1.

The spacing between each subarray element plays an important role in how accurately the subarray models the reconfigurable antenna's element pattern. Tradeoffs ensue in the subarray patterns as the distance between the elements d_{sub} changes. For example, as d_{sub} increases, more nulls and main lobes (grating lobes) come into the subarray's visible region. These pattern characteristics may not accurately represent what a practical pattern reconfigurable antenna can offer. In this work, d_{sub} is chosen to be a half-wavelength. At this distance, one main beam maximum exists within the observation region, and the main beam carries a wide, broad beamwidth—similar to a microstrip patch antenna. These radiation characteristics closely resemble the patterns a single planar microstrip reconfigurable antenna can produce (e.g., the RMPA discussed in Chapter 2).

6.4 Convex Optimization Routine: Results and Preliminary Analysis

In conjunction with the different weight constraint cases, this section graphically presents the preliminary results pertaining to the different scenarios outlined in the previous section. Figure 6-5 and Figure 6-6 present results applied to Scenario 1 (when $\theta_d = 90°$), Figure 6-7 and Figure 6-8 show results applied to Scenario 2 (when $\theta_d = 75°$), and Figure 6-9 and Figure 6-10 show results applied to Scenario 3 (when $\theta_d = 45°$). In each operational scenario, the first figure of the pair compares the magnitude of the radiation pattern per weight constraint case, and the second compares the calculated beam tilting angles of each model RCFG element in the array for each of the cases.

In Figure 6-5, all curves (constraint cases) handle the signal environment well; i.e., the routine places a pattern maximum along the desired signal direction and nulls out the interferers along the specified direction. Compared to the constrained cases, Case 1 does a better job in establishing the required beamwidth and a lower average sidelobe

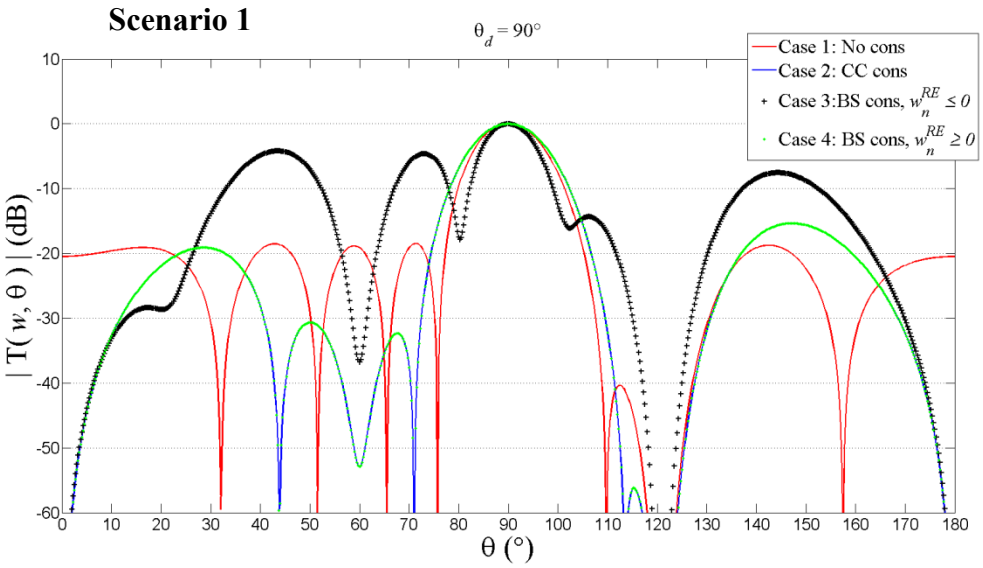

Figure 6-5: Scenario 1. Magnitude of the radiation pattern vs. θ for a 5-element model RCFG array spaced 1.0 λ_0 apart; $\theta_d = 90°$ and $\theta_i = \{120°, 121°, \text{and } 122°\}$. In concert with the convex optimization routine, Case 1: no additional constraints, Case 2: subarray complex conjugate constraint, Case 3: beamsteer constraint with $w_n^{RE} \leq 0$, Case 4: beamsteer constraint with $w_n^{RE} \geq 0$.

level (SLL). Overall, the discrepancies between the cases stem from the additional constraints, namely the magnitude and phases of the weights. Such constraints can make it difficult for the optimization routine to meet all the desired pattern characteristics.

Note, how the Case 2 (CC constraint) and Case 4 (BS constraint with $w_n^{RE} \geq 0$) curves are identical, while the comparative performance of Case 3 (BS constraint with $w_n^{RE} \leq 0$) degrades. The reasons for the similarity and degradation arise because the optimization routine chooses solution weights with $w_n^{RE} \geq 0$ when the CC is applied. This complies with the constraint region described by Case 4, thereby making the curves of Case 2 and Case 4 match. On the other hand, the specified region of Case 3 does not comply with having $w_n^{RE} \geq 0$, resulting in degradation in overall pattern performance. In Figure 6-6, the beemsteer profile for Case 2 and Case 4 centers at about 90°, which is an expected result due to the desired signal's angle of arrival. The profile varies greatly for Case 3 for the reasons previously discussed.

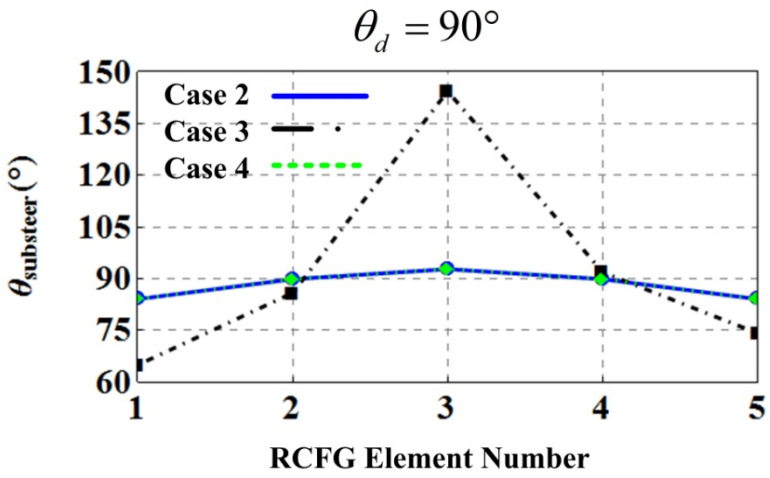

Figure 6-6: Associated beamsteer angles $\theta_{substeer}$ for each RCFG (subarray) element due to results from operational Scenario 1 (when θ_d = 90°, which is at broadside and within the beamsteer constraint). Only Cases 2 to 4 are shown because they apply to the subarray model concept.

When the desired signal arrives from 75°, the routine handles the problem somewhat differently compared to the previous broadside scenario, as shown in Figure 6-7. Again, the desired signal and null requirements are met, but the constrained cases exhibit regions of high sidelobe levels across the observation region compared to the unconstrained case. Since the desired signal is off broadside, the complex conjugate constraint makes it more difficult for the routine to progressively phase the elements to meet the low SLL constraint and signal parameter requirements simultaneously. As a result, variations in all three constrained cases (Cases 2–4) exist. This scenario's beamsteer profile, shown in Figure 6-8, varies more compared to the on-broadside results in Figure 6-6. The graphics show the beamsteering angles of a set of pattern reconfigurable antennas that would be required to realize this scenario's pattern performance. Due to the beamsteer constraint, a majority of the data points representing the profiles of Case 3 and Case 4 lie within 60° and 120°.

In the last operational scenario (when θ_d = 45°), pattern performance changes for all constraint cases. Figure 6-9 shows the results. The routine meets the requirement of having the main beam equal to 0 dB at θ_d and nulls along the specified interference direction in each constraint case. However, the constrained cases suffer more in overall pattern performance. In Case 1, the main beam maximum at θ_d represents the overall

pattern maximum. Such is not the outcome in Cases 2–4, where in certain instances the routine pushes the pattern far over the 0 dB mark. This signifies the inability of the routine to minimize the pattern's objective functions in these spatial regions. The routine relies on element-to-element phasing to meet the desired goal of steering the overall main beam toward θ_d. Unfortunately, the constraints make it more difficult for the optimization routine to accomplish this task concurrently with the others.

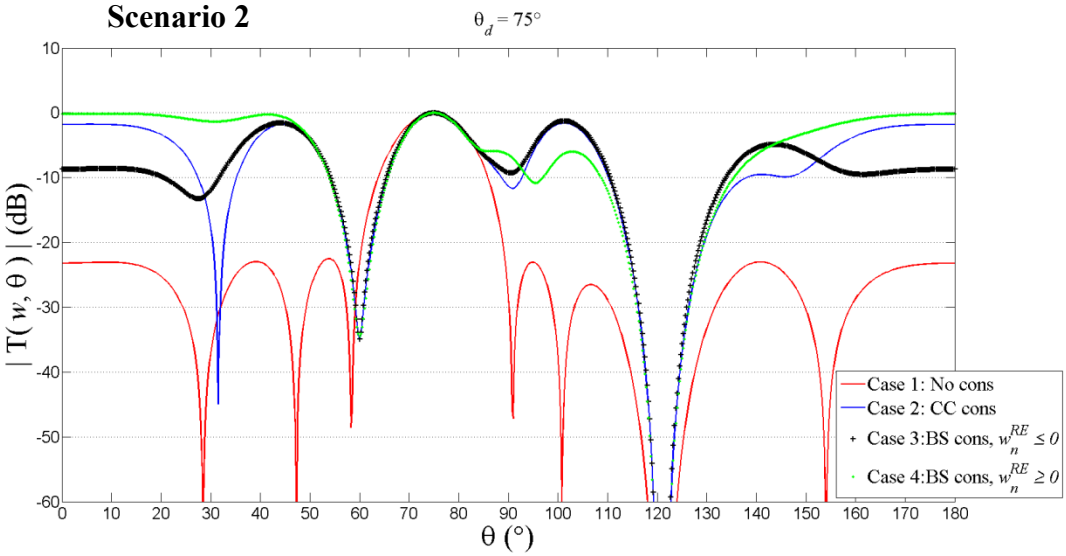

Figure 6-7: Scenario 2. Magnitude of the radiation pattern vs. θ for a 5-element model RCFG array spaced 1.0 λ_0 apart; θ_d = 75° and θ_i = {120°, 121°, and 122°}. In concert with the convex optimization routine, Case 1: no additional constraints, Case 2: subarray complex conjugate constraint, Case 3: beamsteer constraint with $w_n^{RE} \leq 0$, Case 4: beamsteer constraint with $w_n^{RE} \geq 0$.

Analogous to Figure 6-6 and Figure 6-8, Figure 6-10 displays the beamsteer profile for the model RCFG element. Note the variation in the beam tilt values across the RCFG elements in Case 2. In spite of their individual pattern performance, the beamsteer constraint visibly becomes more evident in Cases 3 and 4. The values are restricted to within ±30° of broadside (i.e., between 60° and 120°); unfortunately, overall pattern performance is the tradeoff.

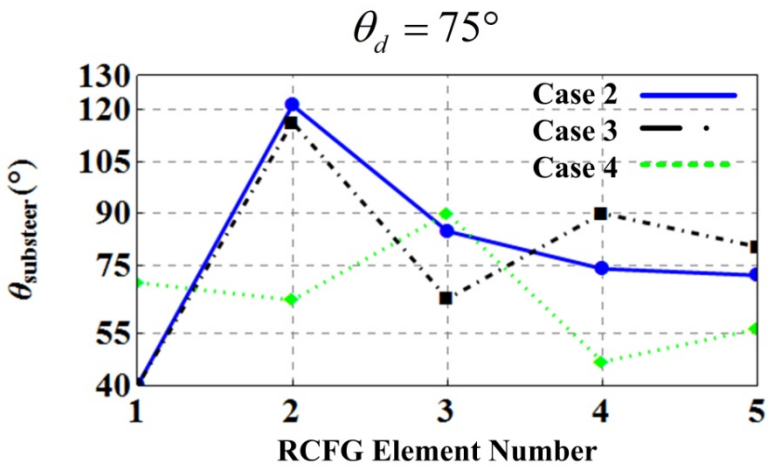

Figure 6-8: Associated beamsteer angles $\theta_{substeer}$ for each RCFG (subarray) element due to results from operational Scenario 2 (when θ_d = 75°, which is within the beamsteer constraint). Only Cases 2 to 4 are shown because they apply to the subarray model concept.

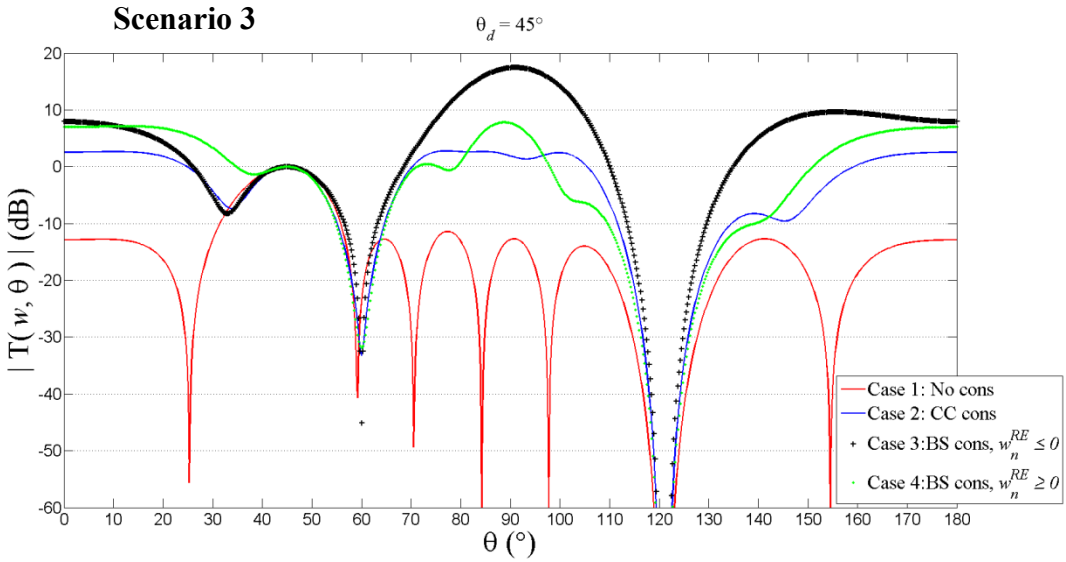

Figure 6-9: Scenario 3. Magnitude of the radiation pattern vs. θ for a 5-element model RCFG array spaced 1.0 λ_0 apart; θ_d = 45° and θ_i = {120°, 121°, and 122°}. In concert with the convex optimization routine, Case 1: no additional constraints, Case 2: subarray complex conjugate constraint, Case 3: beamsteer constraint with $w_n^{RE} \le 0$, Case 4: beamsteer constraint with $w_n^{RE} \ge 0$.

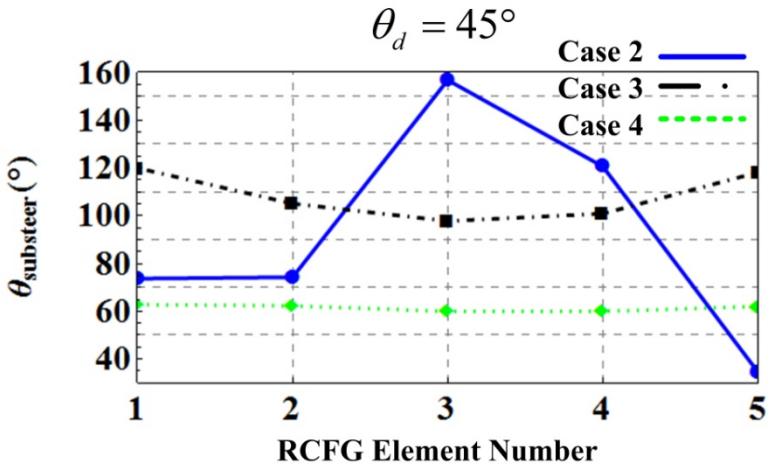

Figure 6-10: Associated beamsteer angles $\theta_{substeer}$ for each RCFG (subarray) element due to results from operational Scenario 3 (when θ_d = 45°, which is outside tbe beamsteer constraint). Only Cases 2 to 4 are shown because they apply to the subarray model concept.

6.5 Discussion

The analysis presented in Section 7.4 merits further discussion. One of the primary goals of the section was to illuminate the performance capability of the convex optimization routine in an adaptive array scenario, with and without the inclusion of the pattern reconfigurable beam tilt model. For the three example signal environments chosen, overall pattern performance with the unconstrained case exceeds that of the constrained cases, i.e., those that seek to incorporate pattern reconfigurability. Even though the desired signal and interference requirements are met, the results vary according to how well the optimization routine can satisfy the imposed constraints.

Under the constraints applicable to the pattern RCFG model, the resulting pattern of the subarray is a purely real cosine function, as seen from the two-element subarray expression derived in (5.9). Without appropriate phasing, it is more difficult for the optimization routine to satisfy not only the complex conjugate and beamsteering constraints but also the general problem constraints (e.g., low SLL). This result indicates one of the caveats when utilizing this model. Nevertheless, the pattern results, in conjunction with the beam tilt profiles, clearly demonstrate the need for a mixture of main beam tilts to meet the specified requirements. Pattern reconfigurable elements with

beamsteering capabilities provide a solution to meet these requirements in an adaptive environment.

Given the results in the previous section, it appears that the convex optimization routine can at times encounter difficulties in meeting the requirements of the signal environment under the imposed constraints. As a result, pattern performance degrades. For example, the off-broadside scenario produced regions of high sidelobe level in the array radiation pattern—in some instances, greater than the pattern in the direction of the desired signal. Thus, it has been determined that two main factors contribute to the routine's limitations in performance under the imposed constrains: (1) the inability of the solving engine to encompass the full range of beamsteering solutions and (2) over-constraining the problem in terms of the suppression points. A discussion of each factor follows.

Subsection 6.2.2 presented the beamsteering constraint as a subdivided pair of inequalities, one imposing $w_n^{RE} \leq 0$ and the other $w_n^{RE} \geq 0$, which are the expressions in (5.11) and (5.12), respectively. As discussed earlier in this chapter, the solver in MATLAB takes in the constraints in matrix inequality form. Unfortunately, the solver cannot satisfy both sets of constraints in an OR like fashion, i.e., the routine can only choose element weights with either $w_n^{RE} \leq 0$ OR $w_n^{RE} \geq 0$. Instead, the solver evaluates them in an AND type fashion, and then when implementing them simultaneously, the solution is null; hence, the reason they must be analyzed individually. While this approach has given much insight into weight and pattern behavior, the limited solution space does inhibit the optimization routine's potential.

The success of the convex optimization routine to meet the low sidelobe requirements stems from a spatial periodic set of suppression points outside the main beam. Each suppression point requires an objective function making this a multi-objective optimization problem. Again, within the additional specified constraints, trying to minimize the sidelobe levels across the spatial region seemingly over-constrains the problem. Recall, an adaptive array enhances a performance index, in this case, the SINR. As a matter of fact, [17] points out that conventional characteristics such as antenna gain, beamwidth, or sidelobe levels, are not useful as performance indicies in the adaptive

array problem. Having low sidelobe levels would be an additional benefit—which could very well improve adaptive array implementation on some levels, but one can only expect tradeoffs in performance when trying to meet such requirements.

Thus, the impact on the output results imposed by two factors discussed above gives reason to seek out methods to alleviate the difficulties associated with them. These include relaxing the sidelobe level criteria and specifying the optimization criteria as the minimum mean square error between the actual array output and the ideal array output. Such difficulties lead back to the least mean square (LMS) technique, which was implemented in the early chapters of this dissertation. In conjunction with this step, the approach suggests moving away from MATLAB as the programming routine and implementing the LMS technique in Mathematica®. Mathematica has greater flexibility in terms of Boolean constraints; and thus the beamsteering constraints can be implemented in the desired OR fashion. The invaluable insight gained by utilizing the convex optimization routine with MATLAB can now be applied using the LMS technique in Mathematica. This approach will lead to more favorable pattern reconfigurable antenna solutions.

CHAPTER 7
PATTERN VARIABILITY: LMS IMPLEMENTATION

This chapter makes use of the knowledge gained from implementing the convex optimization routine with MATLAB as the solver. Instead of seeking to minimize the sidelobe level across the spatial range with MATLAB as the solver, the focus turns to utilizing the least mean square (LMS) technique with Mathematica. In this way, the optimization problem is not overly constrained, and this solver has more flexibility in terms of fulfilling the imposed constraints. Nevertheless, the objective remains the same: allowing the optimization routine to select the best solution set. After the routine returns the solution weights, the task is to analyze the resulting pattern for each subarray and link it to the patterns of the pattern reconfigurable element. In this way, element pattern reconfigurability will be specified.

This chapter will first put into form an assortment of LMS analytical relationships. Each is described in the context of applying them in a minimization routine. The next section analyzes and evaluates the performance of the LMS approach with a variety of qualifying adaptive array scenarios. Here, the different scenarios provide the means to compare and contrast the results due to the varying parameters. The last section takes some of the preceding examples and examines them in further detail to determine what requirements are necessary for the pattern reconfigurable element design.

7.1 Least Mean Square Technique: Algorithm Details

Chapter 3 discussed some of the fundamentals of adaptive arrays, which included details involving the least mean square technique. Recall, the LMS algorithm aims to minimize the error in the signal at the array output by finding the array weights that yield maximum SINR from a given set of signals. In that chapter, a variety of analytical relationships were given; this chapter draws from those relationships and applies them in the context of having the LMS algorithm select the required beam tilts in each model pattern reconfigurable element. This section reintroduces the analytical relations, but

does so in terms of applying them to a minimization routine. Prior to analyzing and displaying future results using the LMS technique, a cross-check of the results using the LMS technique with convex method is made.

7.1.1 Objective Function Realization

As mentioned, an adaptive array using the LMS technique, as reported by Compton [17], is based on the minimum mean square error concept. An error signal $\varepsilon(t)$ is obtained by subtracting the array output $s(t)$ from another signal called the reference signal $r(t)$. In reference to Figure 3-1, the array output contains a desired signal, interference, and thermal noise: $d(t)$, $i(t)$, and $n(t)$, respectively. The minimum mean square error criterion adjusts the weights in the array to maximize the desired signal and minimize the interference and thermal noise at the array output. Let the reference signal $r(t)$ be a replica of the desired signal. (This is a suspicious result from an information theory point of view, but Compton [17] states that $r(t)$ does not have to be a perfect replica of $d(t)$; it is only necessary that $r(t)$ be correlated with $d(t)$. A suitable $r(t)$ can be obtained from processing at the array output [17]). Also, as before assume the desired signal, interference, and thermal noise are all zero-mean processes uncorrelated with each other. This implies cross-product terms in subsequent calculations are zero.

Note that relationships governing the adaptive array fundamentals, those presented in Section 3.2, are given in complex form. Following the same ideology as in previous chapters, the LMS expression presented in this section will be kept in terms of real-valued weights and signals. Compton defines the weights and signals in terms of an in-phase and quadrature component (I and Q); the following definitions will adhere to this nomenclature. When it comes to determining the final result, the unknown weight vector in I–Q form easily equates to its equivalent complex form. Compton defines the complex weight in term of I–Q components as $w_n = w_{I_n} - jw_{Q_n}$ [17].

The objective function now becomes the mean square error, $E\left[\varepsilon^2(t)\right] = E\left[\left(r(t) - s(t)\right)^2\right]$ which can be written in compact matrix form given by [17] as

$$E\left[\varepsilon^2(t)\right] = E\left[r^2(t)\right] - 2\mathbf{W}_r^T\mathbf{S}_r + \mathbf{W}_r^T\mathbf{\Phi}_r\mathbf{W}_r, \tag{6.1}$$

where $E[\ ]$ is the expectation operator and $\mathbf{W}_r$ is the unknown weight vector of size $2N \times 1$, i.e.,

$$\mathbf{W}_r = \left[w_{I_1}\ w_{Q_1}\ w_{I_2}\ w_{Q_2} \ldots..\ w_{I_N}\ w_{Q_N} \right]^T. \tag{6.2}$$

The reference correlations vector $\mathbf{S}_r$ is also of size $2N \times 1$ and is expressed as

$$\mathbf{S}_r = E\begin{bmatrix} x_{I_1}(t)\, r(t) \\ x_{Q_1}(t)\, r(t) \\ x_{I_2}(t)\, r(t) \\ x_{Q_2}(t)\, r(t) \\ \vdots \end{bmatrix}. \tag{6.3}$$

Lastly, the total covariance matrix $\mathbf{\Phi}_r$ is of size $2N \times 2N$ and accounts for the correlations between the signal components from each of the *N* elements in the linear array. The relationship in (6.4) expresses an expanded version of the matrix.

$$\mathbf{\Phi}_r = E\begin{bmatrix} x_{I_1}(t)\,x_{I_1}(t) & x_{I_1}(t)\,x_{Q_1}(t) & x_{I_1}(t)\,x_{I_2}(t) & x_{I_1}(t)\,x_{Q_2}(t)... \\ x_{Q_1}(t)\,x_{I_1}(t) & x_{Q_1}(t)\,x_{Q_1}(t) & x_{Q_1}(t)\,x_{I_2}(t) & x_{Q_1}(t)\,x_{Q_2}(t)... \\ x_{I_2}(t)\,x_{I_1}(t) & x_{I_2}(t)\,x_{Q_1}(t) & x_{I_2}(t)\,x_{I_2}(t) & x_{I_2}(t)\,x_{Q_2}(t)... \\ x_{Q_2}(t)\,x_{I_1}(t) & x_{Q_2}(t)\,x_{Q_1}(t) & x_{Q_2}(t)\,x_{I_2}(t) & x_{Q_2}(t)\,x_{Q_2}(t)... \\ \vdots & \vdots & \vdots & \vdots \end{bmatrix}. \tag{6.4}$$

In the above definitions, $x(t)$ is the signal from the array element composed of a linear combination of the desired signal, interference, and thermal noise components (i.e., $d(t)$, $i(t)$, and $n(t)$, respectively). Utilizing this relationship and the statistical assumptions, the total covariance matrix in (6.4) equates to a sum of individual covariance matrices; i.e., $\mathbf{\Phi}_r = \mathbf{\Phi}_{r_d} + \mathbf{\Phi}_{r_i} + \mathbf{\Phi}_{r_n}$, one for the desired, interference, and noise components of the signal. Each individual matrix takes on the same form as in (6.4) but with the either the variables $d(t)$, $i(t)$, or $n(t)$ replacing $x(t)$.

To give further insight into the components of these matrices, take the desired signal covariance matrix as an example. It follows from (6.4) and can be expressed as (without the time dependence)

$$\mathbf{\Phi}_{r_d} = E\begin{bmatrix} d_{I_1} d_{I_1} & d_{I_1} d_{Q_1} & d_{I_1} d_{I_2} & d_{I_1} d_{Q_2} \ldots \\ d_{Q_1} d_{I_1} & d_{Q_1} d_{Q_1} & d_{Q_1} d_{I_2} & d_{Q_1} d_{Q_2} \ldots \\ d_{I_2} d_{I_1} & d_{I_2} d_{Q_1} & d_{I_2} d_{I_2} & d_{I_2} d_{Q_2} \ldots \\ d_{Q_2} d_{I_1} & d_{Q_2} x_{Q_1} & d_{Q_2} d_{I_2} & d_{Q_2} d_{Q_2} \ldots \\ \vdots & \vdots & \vdots & \vdots \end{bmatrix}, \tag{6.5}$$

where $d_{I_j} = A_d \cos\left(\omega t + \psi_d + \phi_{d_j}\right)$ and $d_{Q_k} = A_d \sin\left(\omega t + \psi_d + \phi_{d_k}\right)$ [17]. In these expressions, A_d is the desired signal amplitude, ψ_d is the carrier phase angle at the antenna element (assumed to be a uniformly distributed random variable) and $\phi_{d_{j,k}}$ is the inter-element phase shift. For the given array topology, define $\phi_{d_n} = (n-1)\frac{2\pi}{\lambda} d \cos\theta_d$ analogously to the relationship in (3.2). With these definitions, the matrix elements of $\mathbf{\Phi}_{r_d}$ contain the following:

$$\begin{aligned} E\left[d_{I_j} d_{I_k}\right] &= E\left[d_{Q_j} d_{Q_k}\right] = A_d^2 \cos\left(\phi_{d_j} - \phi_{d_k}\right) \\ E\left[d_{I_j} d_{Q_k}\right] &= -A_d^2 \sin\left(\phi_{d_j} - \phi_{d_k}\right) \\ E\left[d_{Q_j} d_{I_k}\right] &= A_d^2 \sin\left(\phi_{d_j} - \phi_{d_k}\right) \end{aligned} \quad . \tag{6.6}$$

The makeup of the interference covariance matrix follows suit; the elements of $\mathbf{\Phi}_{r_i}$ thus contain

$$\begin{aligned} E\left[i_{I_j} i_{I_k}\right] &= E\left[i_{Q_j} i_{Q_k}\right] = A_i^2 \cos\left(\phi_{i_j} - \phi_{i_k}\right) \\ E\left[i_{I_j} i_{Q_k}\right] &= -A_i^2 \sin\left(\phi_{i_j} - \phi_{i_k}\right) \\ E\left[i_{Q_j} i_{I_k}\right] &= A_i^2 \sin\left(\phi_{i_j} - \phi_{i_k}\right) \end{aligned} \quad , \tag{6.7}$$

where A_i is the interference signal amplitude and $\phi_{i_n} = (n-1)\frac{2\pi}{\lambda} d\cos\theta_i$ is the inter-element phase shift. In the case of multiple interferers, multiple $\mathbf{\Phi}_{r_i}$ matrices will exist—one for each interference signal—and the sum of them represents the total $\mathbf{\Phi}_{r_i}$ matrix. As far as the noise matrix, the thermal noise components are assumed to be zero-mean random processes. Each of the components are (1) statistically independent of each other, (2) statistically independent of the desired signal, and (3) statistically independent of the interference signal. This makes $E\left[n_{I_j} n_{I_j}\right] = E\left[n_{Q_j} n_{Q_j}\right] = \sigma^2$, where σ^2 is the noise power on each element [17]. The noise covariance matrix then becomes

$$\mathbf{\Phi}_{r_n} = \sigma^2 \mathbf{I}_r, \tag{6.8}$$

where $\mathbf{I}_r$ is a $2N \times 2N$ identity matrix.

Next, the reference correlation vector stems from letting the reference signal be a CW signal, correlated with the desired signal, and statistically independent of the interference signal and noise. Define it as $r(t) = R\cos\left(\omega t + \psi_d\right)$, where R is the reference signal amplitude [17]. The expression in (6.3) becomes

$$\mathbf{S}_r = E\begin{bmatrix} d_{I_1}(t)\, r(t) \\ d_{Q_1}(t)\, r(t) \\ d_{I_2}(t)\, r(t) \\ d_{Q_2}(t)\, r(t) \\ \vdots \end{bmatrix}, \tag{6.9}$$

where the elements of $\mathbf{S}_r$ include $E\left[d_{I_j}(t)\, r(t)\right] = A_d R\cos\phi_{d_j}$ and $E\left[d_{Q_j}(t)\, r(t)\right] = A_d R\sin\phi_{d_j}$. As utilized by Compton in [17], it is common when computing the results to let the ratio $A_d/R = 1$. Similarly to the earlier work in this dissertation, the covariance matrices and correlation vector will be analyzed in normalized form—normalized with respect to the noise power σ^2. Where $\xi_d = \frac{A_d^2}{\sigma^2}$ and

$\xi_i = \frac{A_i^2}{\sigma^2}$ translate into the previously discussed signal-to-noise ratio (SNR) and interference-to-noise (INR), respectively. The same numerical values apply considering a strong interference environment, i.e., SNR is equal to 0 dB and INR is equal to 40 dB.

Last, the relationship in (3.3) expressed the SINR in general form. It will be of great interest to once again use the SINR as a comparison metric for adaptive array performance. After determining the LMS weights and converting both the weights and the covariance matrices into complex form as defined in [17], the SINR can be determined with the following:

$$SINR = \frac{P_d}{P_i + P_n} = \frac{\frac{1}{2}\tilde{\mathbf{W}}^H \tilde{\mathbf{\Phi}}_d \tilde{\mathbf{W}}}{\frac{1}{2}\tilde{\mathbf{W}}^H \tilde{\mathbf{\Phi}}_i \tilde{\mathbf{W}} + \frac{1}{2}\tilde{\mathbf{W}}^H \tilde{\mathbf{\Phi}}_n \tilde{\mathbf{W}}}, \tag{6.10}$$

where the superscript *H* signifies the Hermitian and the tilde indicates the variables are in complex form. The expression states the SINR equates to the ratio of the output desired signal power to the sum of the output interference and noise power. Each power term is normalized, since the covariance matrices are normalized to the noise power σ^2 as previously defined.

7.1.2 Method Comparison: Example Plots

With all the components of (6.1) defined, the mean square error $E\left[\varepsilon^2(t)\right]$ becomes the objective function, and the goal is to minimize this function subject to the various weight constraints discussed in Chapter 6. The mean square error is already in quadratic form; i.e., a quadratic function of the weights, which makes the extremum of the function's surface a minimum. Hence, the minimization routine in Mathematica can be utilized to solve the problem without much concern in regards to the routine finding a local rather than a global minimum.

Before continuing with further analysis using the LMS algorithm in concert with Mathematica's minimization routine, it is important to graphically compare the LMS technique with the convex optimization routine. Consider the following figures.

Figure 7-1 incorporates the *no additional constraint case*, while Figure 7-2 implements the *complex conjugate constraint*. In each figure, the curves compare the LMS and convex routines. Let the particulars in each scenario equate to those in the example presented in Figure 6-9: 5 RCFG (subarray) elements in an off-broadside situation with θ_d = 45° and a small cluster of interference signals at θ_i = {120°, 121°, and 122°}.

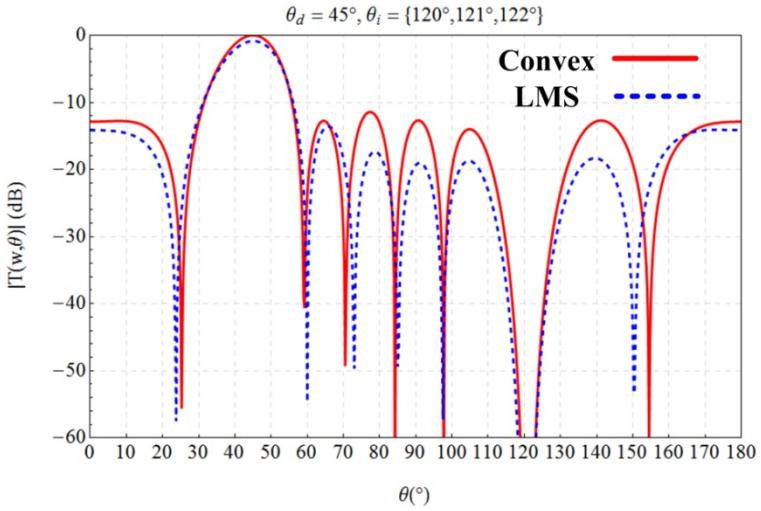

Figure 7-1: Adaptive array pattern in a scenario that encompasses a 5-element model RCFG array spaced 1.0 λ_0 apart; θ_d = 45° and θ_i = {120°, 121°, and 122°}. The graph compares the previously utilized convex optimization routine (solid curve) to the least mean square technique (dashed curve). In this case, both methods adhere to the no additional constraint on the weights and demonstrate the pattern objectives of each method.

In Figure 7-1, both methods satisfy the signal environment requirements by placing a pattern maximum along the desired signal direction and nulls along the interference signals. Even though both curves have similar trends, notice how the convex routine (solid curve) tries to establish sidelobe maximums at an equal level across the spatial range, which is part of its objective. On the other hand, the LMS routine (dashed curve)—whose objective is to satisfy the desired and interference signal requirements only—does not have equal sidelobe levels across the spatial range. Additionally, with the desired signal being incident 45° from broadside, the LMS technique provides lower sidelobe levels than the convex optimization routine.

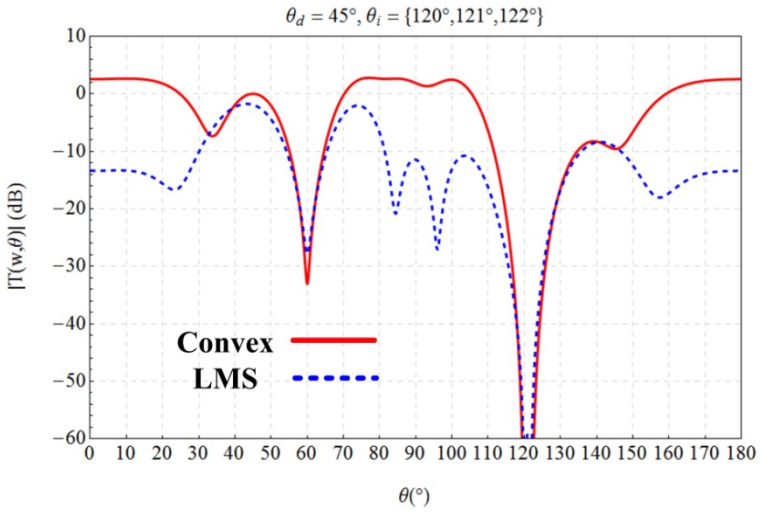

Figure 7-2: Adaptive array pattern in a scenario that encompasses a 5-element model RCFG array spaced 1.0 λ_0 apart; θ_d = 45° and θ_i = {120°, 121°, and 122°}. The graphic compares the previously utilized convex optimization routine (solid curve) to the least mean square technique (dashed curve). In this case, the weights are subject to the complex conjugate constraint; again the curves demonstrate the objectives each method aims to accomplish.

Application of the complex conjugate constraint in Figure 7-2 illustrates much more disparity between the two methods. The results confirm the decision to utilize the LMS routine in concert with the pattern reconfigurable antenna model (i.e., the subarray model in conjunction with the necessary weight constraints). Since the convex routine has tendencies to over-constrain the array problem, it does not allow a pattern maximum along θ_d. Instead, pattern regions above the target 0 dB mark ensue. Such regions are not evident in the LMS routine, which displays a true pattern maximum. The one minor caveat is that under the given signal environment and weight requirements, the LMS curve presents a main beam maximum slightly shifted from the desired signal direction (several degrees at best).

The preceding figures serve to demonstrate the effectiveness of the LMS technique over the convex optimization routine within the context of the research. It is apparent from the results that the methodology behind using the LMS technique gives the best option for effectively implementimg the subarray as a model pattern reconfigurable antenna in the adaptive array.

7.2 LMS Approach: Analysis and Results

This section evaluates the performance of the LMS approach with a variety of different scenarios. Some scenarios qualify as potential adaptive array scenarios (e.g., different signal environments), while others aim to demonstrate the effects due to changes in the adaptive array geometry (e.g., number of subarray elements or subarray spacing). In all, the different scenarios will provide the means to compare and contrast the results across the varying parameters. The figures pertaining to each analysis will include one or a combination of the following performance metrics: the SINR as defined by (6.10), the magnitude of the radiation pattern ($|T(\mathbf{w},\theta)|$) for a particular adaptive array instance, and a table listing the required beam tilt angle for each model RCFG element in the array. Recall, the beam tilts stem from the corresponding radiation pattern of the array.

Before moving on to the subsections describing each scenario, the different weight constraint cases introduced earlier in Chapter 6, which are used again here, are listed below. Note the addition of Case 5, a combination of Case 3 and Case 4 from above, which stems from the constraint implementation capabilities of Mathematica.

- Weight constraint Case 1: No additional weight constraints, essentially weight constraint free.
- Weight constraint Case 2: Complex conjugate constraint. The w_n and w_{n+1} weight of each element in each subarray are complex conjugates of each other, i.e., $w_{n+1} = w_n^*$.
- Weight constraint Case 5: Beamsteering constraint with *both* $w_n^{RE} \le 0$ and $w_n^{RE} \ge 0$, a combination of Case 3 and Case 4 from above. The allowable beam tilt for each model pattern RCFG element lies between $\pm 30°$ of broadside, i.e., $60° \le \theta_{substeer} \le 120°$.

7.2.1 Constraint Comparison: Desired Signal Within Beamsteer Range

This scenario analyses the three different constraint cases with the desired signal falling within the specified beamsteer range as defined in Case 5. Thus, let $\theta_d = 70°$ and the other parameters consist of having $N/2 = 5$ RCFG elements, $d_{Main} = 1.0\lambda_0$, and a small cluster of interference signals arriving from $\theta_{int} = \{\theta_i, 120°, \text{and } 122°\}$. Note that the inclusion of the θ_i variable in the interference listing means that the SINR will be plotted against this interference angle (i.e., SINR versus θ_i). In this scenario and the one to follow, multiple interference signals impinge on the array. Therefore, the interference angle of all incident values, except the θ_i variable, are held constant. Only the θ_i will vary over the spatial range.

Also, since the adaptive array radiation pattern corresponds to a θ_i instance, it will be plotted with the other interferers for a particular θ_i value: in this scenario $\theta_i = 60°$. The objective of this analysis is to demonstrate what effects ensue when implementing the weight constrained cases (Cases 2 and 5) versus the unconstrained case (Case 1) utilizing the LMS routine. Figure 7-3 displays the results in a three graphic configurations: (a) SINR, (b) $\left|T(\mathbf{w},\theta)\right|$, and the (c) beamsteer table.

The resulting curves for the unconstrained case in Figure 7-3(a) and (b) serve as benchmarks for the other cases. As seen, the SINR and pattern plots along with the beamsteer table for Case 2 and Case 5 are practically identical. Since the beam tilts for Case 2 fall within the beamsteer region, the revised constraint Case 5 follows suit. As always in SINR plots, the "standard null" at θ_d arises in all the curves. Even though the constrained cases do not maintain the same performance level as the unconstrained case across the θ_i spatial range (just less than 10 dB outside of the standard null region), regions of comparable performance do exist indicating the feasibility of the constrained routines. Note, the spikes occur in the SINR plot near the $\theta_i = 60°$ and 120° regions—these result from the interferer falling into a pattern null and correspond to the notion of null reconfigurability discussed in Chapter 5.

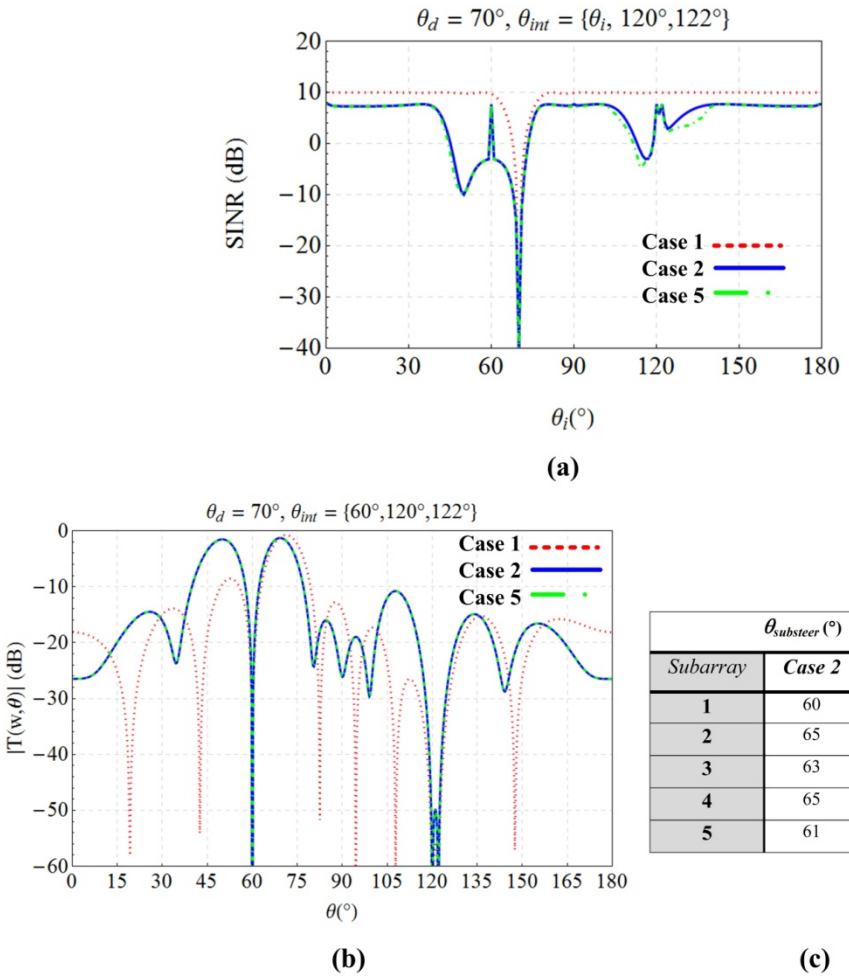

$\theta_{substeer}$ (°)		
Subarray	***Case 2***	***Case 5***
1	60	60
2	65	65
3	63	63
4	65	65
5	61	61

(c)

Figure 7-3: Adaptive array scenario encompasses a 5-element model RCFG array spaced 1.0 λ_0 apart; θ_d = 70° and θ_{int} = {θ_i, 120°, and 122°} utilizing the LMS optimization technique. The SINR vs. θ_i plot in (a) compares the performance of the three weight constraint cases: Case 1 (dotted), Case 2 (solid), and Case 5 (dot-dashed). The pattern plot in (b) does the same but with θ_i = 60°, and the $\theta_{substeer}$ table in (c) compares the beam tilt angle for each RCFG (subarray) element associated with the pattern for constraint Cases 2 and 5.

The plots in Figure 7-3(b) detail the radiation patterns for θ_i = 60°, thereby making θ_{int} = {60°, 120°, and 122°}, a multiple interference environment. The LMS algorithm accomplishes the task of maximizing at the desired signal and nulling out the interference in all three cases; hence, the high SINR value at θ_i = 60° in Figure 7-3(a). Nevertheless, the SINR and pattern variation are no doubt a product of the additional weight constraints, which is an acceptable tradeoff in order to implement pattern variability with the RCFG model.

7.2.2 Constraint Comparison: Desired Signal Outside Beamsteer Range

In comparison to the previous scenario, the one presented in this subsection differs by the desired signal arriving at an angle outside the specified beamsteer range, θ_d = 45°. All other parameters remain the same (i.e., $N/2$ = 5 RCFG elements, $d_{Main} = 1.0\lambda_0$, and θ_{int} = {θ_i, 120°, and 122°}) and the graphic representation of Figure 7-4 is similar to that of Figure 7-3. The analysis once again aims to illustrate the weight constrain effects; this time however, with the desired signal located outside the constraint region of Case 5. Figure 7-4 displays the results in three graphic configurations: (a) SINR, (b) $\left|T(\mathbf{w},\theta)\right|$, and the (c) beamsteer table. In the previous scenario, the pattern performed well in terms of establishing a main beam maximum at θ_d with θ_i being 10° away from θ_d; in this scenario, the patterns are plotted with θ_i = 40°, much closer to θ_d.

Compared to the unconstrained case, the average SINR levels in Case 2 and Case 5 perform well, only being about 5 dB below the benchmark. Small but noticeable differences exist between the two constrained cases in both the SINR and selected pattern plot. The beamsteer constraint contributes to this effect as seen in the table. The results of Case 2 place $\theta_{substeer}$ angles outside the $60° \le \theta_{substeer} \le 120°$ range, while those of Case 5 keep the results within the range. Notice the lower-than-maximum SINR values for the constrained cases near θ_i = 40°; these results correlate to the pattern curves in which the algorithm cannot place a full main beam maximum in the θ_d direction. These results further exemplify the effect of having the interference signal near the desired signal.

7.2.3 Constraint Comparison: Interference Signals Spread, Not Clustered

In the previous two scenarios, two of the non-varying interference signals were clustered together (i.e., {120°, and 122°}). This scenario simulates when these interference signals arrive spread apart from each over the spatial range (at least one on each side of the intended main beam direction). With the addition of the variable interferer, they exist as θ_{int} = {θ_i, 60°, and 30°}. Figure 7-5 presents the SINR and pattern plots along with the beamsteer table in the typical configuration scheme with the signal arriving within the specified beamsteer range, θ_d = 110°. All other parameters

remain the same (i.e., $N/2 = 5$ RCFG elements, $d_{Main} = 1.0\lambda_0$). The analysis intends to illustrate how performance is affected when the interference signals are spread over the spatial range; i.e., the performance is compared to the previous scenarios in which the angles of arrival of the interference signals were grouped closer together.

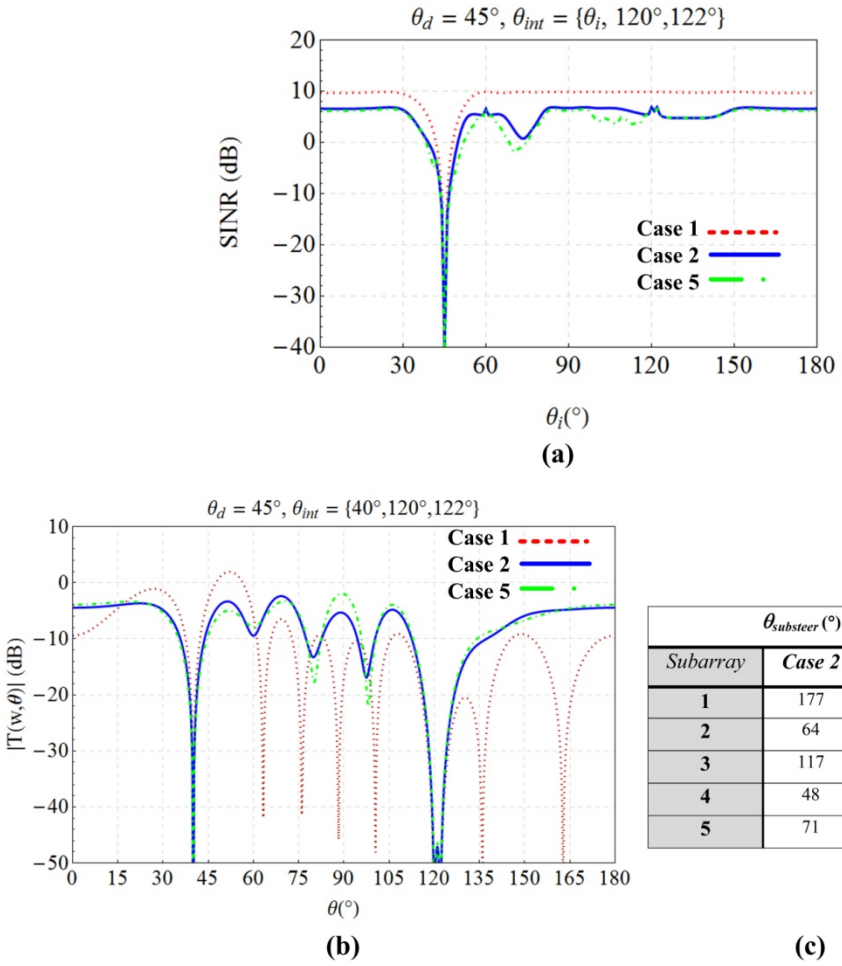

$\theta_{substeer}$ (°)		
Subarray	*Case 2*	*Case 5*
1	177	120
2	64	66
3	117	120
4	48	60
5	71	77

(c)

Figure 7-4: Adaptive array scenario encompasses a 5-element model RCFG array spaced 1.0 λ_0 apart; $\theta_d = 45°$ and $\theta_{int} = \{\theta_i, 120°, \text{and } 122°\}$ utilizing the LMS optimization technique. The SINR vs. θ_i plot in (a) compares the performance of the three weight constraint cases: Case 1 (dotted), Case 2 (solid), and Case 5 (dot-dashed). The pattern plot in (b) does the same but with $\theta_i = 40°$, and the $\theta_{substeer}$ table in (c) compares the beam tilt angle for each RCFG (subarray) element associated with the pattern for constraint Cases 2 and 5.

The constrained SINR curves in Figure 7-5(a) demonstrate that having interferers spread over the spatial range has a much greater effect compared to a clustered group. For this particular setting, the maximum SINR values are about 10 dB below the benchmark

case. The radiation patterns in Figure 7-5(b) show an interesting result seen in the convex optimization routine. When θ_i = 40°, Cases 2 and 5 reveal regions of high sidelobes that are greater than the maximum of the main beam. The algorithm places priority in nulling out the interference signals, and consequentially, high sidelobe regions result due to their spacing. One other interesting artifact to notice lies in the beamsteer table. Notice in Case 2 all values except $\theta_{substeer}$ for subarray #1 are within the beamsteer constraint range; enforcing the constraint in Case 5 pushes the beam tilts of subarray elements 1 and 3 to 60° and 120°, respectively. This case gives one illustration of how the routine compensates the beam tilting angles when implementing the beamsteer constraint.

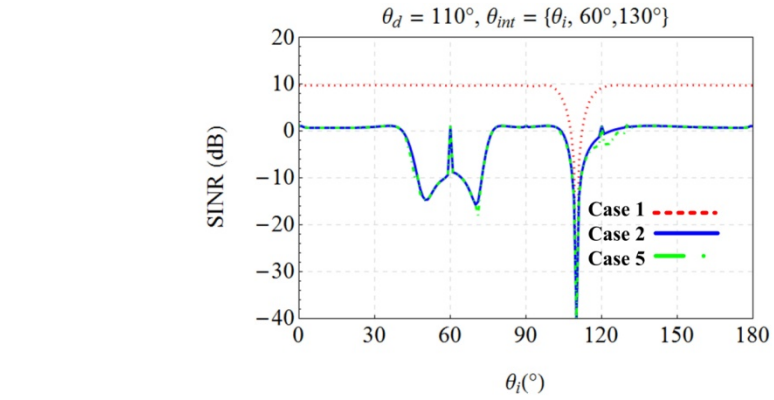

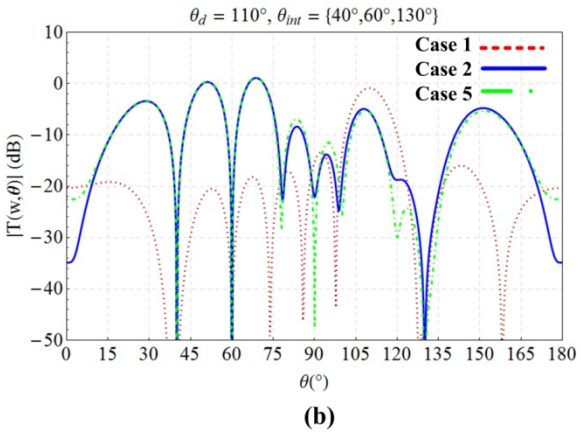

$\theta_{substeer}$ (°)		
Subarray	*Case 2*	*Case 5*
1	54	60
2	87	85
3	96	120
4	95	93
5	63	62

(c)

Figure 7-5: Adaptive array scenario encompasses a 5-element model RCFG array spaced 1.0 λ_0 apart; θ_d = 110° and θ_{int} = {θ_i, 60°, and 130°} utilizing the LMS optimization technique. The SINR vs. θ_i plot in (a) compares the performance of the three weight constraint cases: Case 1 (dotted), Case 2 (solid), and Case 5 (dot-dashed). The pattern plot in (b) does the same but with θ_i = 40°, and the $\theta_{substeer}$ table in (c) compares the beam tilt angle for each RCFG (subarray) element associated with the pattern for constraint Cases 2 and 5.

The results graphically convey the effects when multiple interferers spread over the spatial range impinge on the adaptive array. Compared to the clustered examples, the adaptive array performance in terms of SINR decreases. Even though the scenario exemplifies only three interferers, further in-depth analysis verifies further performance degradation for an increasing number of interferers. Overall, the results indicate that the constraint cases perform better when a cluster of interference signals impinges upon the array. This is an important discovery when considering the limitations and capabilities involved upon integrating a pattern reconfigurable antenna with beam tilts in the process.

7.2.4 Element Number Comparison: Larger Number of Interferes

The previous scenario provided insight into the effects on adaptive array performance in terms of the spatial distribution of the interference angles. Even though the results utilized a small number of interferers, it was mentioned that a larger number of interferers diminishes performance. Along this train of thought, this scenario will investigate performance in terms of SINR for a large number of interferers while increasing the number of the subarray elements in the array. The analysis aims to illustrate how the SINR changes with the addition of more model RCFG elements—utilizing only the complex conjugate constraint (enforcement of Case 2). It is sufficient to use this constraint because, as seen in the previous scenarios, the results of Case 5 compare well to Case 2, especially when θ_d is within the beamsteer constraint range, as will be the case here: $\theta_d = 75°$.

Furthermore, keeping the distance between model RCFGs the same (i.e., $d_{Main} = 1.0\lambda_0$) means that as the number of model RCFGs increases, the array aperture size increases. In general, this will not detract from the research's focus of having a small number of elements in the array because the number remains small compared to large scale adaptive array systems. Thus, let $N/2 = \{5, 8, 11, 15\}$ RCFG elements, a total of four cases, each represented by its own curve in the SINR plots contained within Figure 7-6. A total of seven interferers impinge on the array, Figure 7-6(a) demonstrates a spatial spread (i.e., $\theta_{int} = \{\theta_i, 30°, 45°, 60°, 110°, 125°, \text{and } 140°\}$), while Figure 7-6(b) exemplifies a cluster of two group (i.e., $\theta_{int} = \{\theta_i, 55°, 57°, 60°, 110°, 112°, \text{and } 114°\}$).

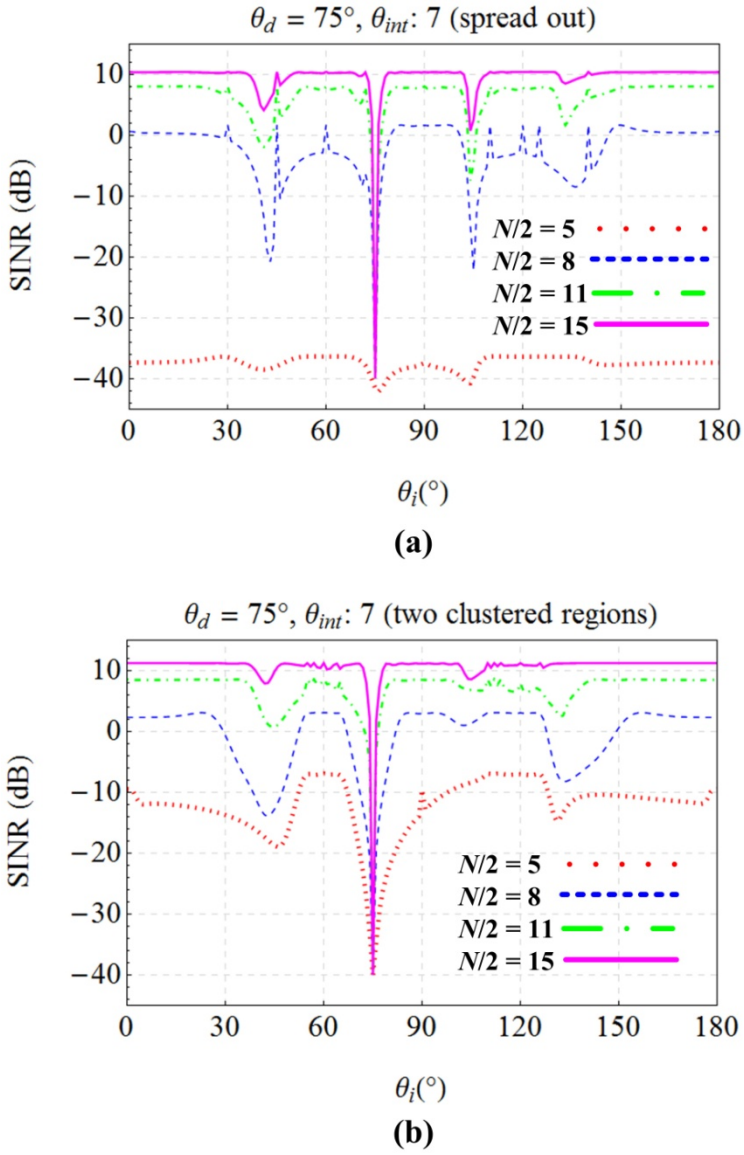

Figure 7-6: Adaptive array scenario comparing SINR vs. an increasing number of model RCFG elements ($N/2$ = {5, 8, 11, 15}) in an environment consisting of a large number of interferers. In (a) the interferers are spread about, e.g., θ_{int} = {θ_i, 30°, 45°, 60°, 110°, 125°, and 140°} and in (b) two clustered groups exist, i.e., θ_{int} = {θ_i, 55°, 57°, 60°, 110°, 112°, and 114°}. The scenario imposes constraint Case 2 in both (a) and (b).

The results in both graphs clearly show that as the number of model subarray elements increases, the effectiveness of the routine in terms of SINR increases as well. Taking the $N/2$ = 15 curve as the limiting case, the characteristics of the other curves approach this case as the number of elements increases. Note the diminishing return

effect as $N/2$ increases in terms of average gain in SINR (dB); for example, about a 10 dB increase when the maximum value of the $N/2$ curve increases from 5 to 8 (three elements), in contrast to only about a 3 dB increase when the maximum value of the $N/2$ curve increases from 11 to 15 (four elements). It is important to note the trend of the curves since increasing the elements also increases the maximum SINR value; in a situation where all the elements are isotropic, the SINR goes as $10 \log_{10} (N)$.

Also, for the same number of interferes, Figure 7-6(a) shows once again the difficulty in handling a large number of widely distributed interferers compared to a clustered group as in Figure 7-6(b). Comparing curves in each graph with the same number of subarray elements, the clustered region curves have a smoother representation and/or higher SINR values opposed to the widely distributed interference curves. The outcomes signify that under the constraints it is easier for the LMS algorithm to adapt to a local group of interferes versus interferes spread over the spatial range. Altogether, the results of this scenario indicate that in order to handle an environment consisting of a large number of interferers, more elements are required—a factor that is associated with the number of degrees of freedom offered by the array.

7.2.5 Element Separation Comparison

The last scenario characterizes the effects that occur when the spacing between model RCFG elements changes uniformly. All the results presented thus far kept d_{Main} constant at $1.0\lambda_0$, in turn leaving the edge-to-edge spacing between adjacent subarrays at $0.5\lambda_0$. It is instructive to analyze spacing effects since placing the elements in a relatively large spacing configuration is one of this dissertation's main objectives. This subsection intends to describe this effect by comparison with the scenario presented in Section 7.2.1 wherein θ_d = 70°, $N/2$ = 5 RCFG, and θ_{int} = {θ_i, 120°, and 122°}. The analysis once again imposes a complex conjugate constraint (Case 2) and the varying parameter is d_{Main}. Let d_{Main} = {$1.0\lambda_0$, $1.25\lambda_0$, $1.5\lambda_0$, and $2.0\lambda_0$}, which in turn corresponds to an edge-to-edge adjacent subarray spacing of {$0.5\lambda_0$, $0.75\lambda_0$, $1.0\lambda_0$, and $1.5\lambda_0$}, respectively. Figure 7-7 presents the SINR and pattern plots along with a beamsteer table in the

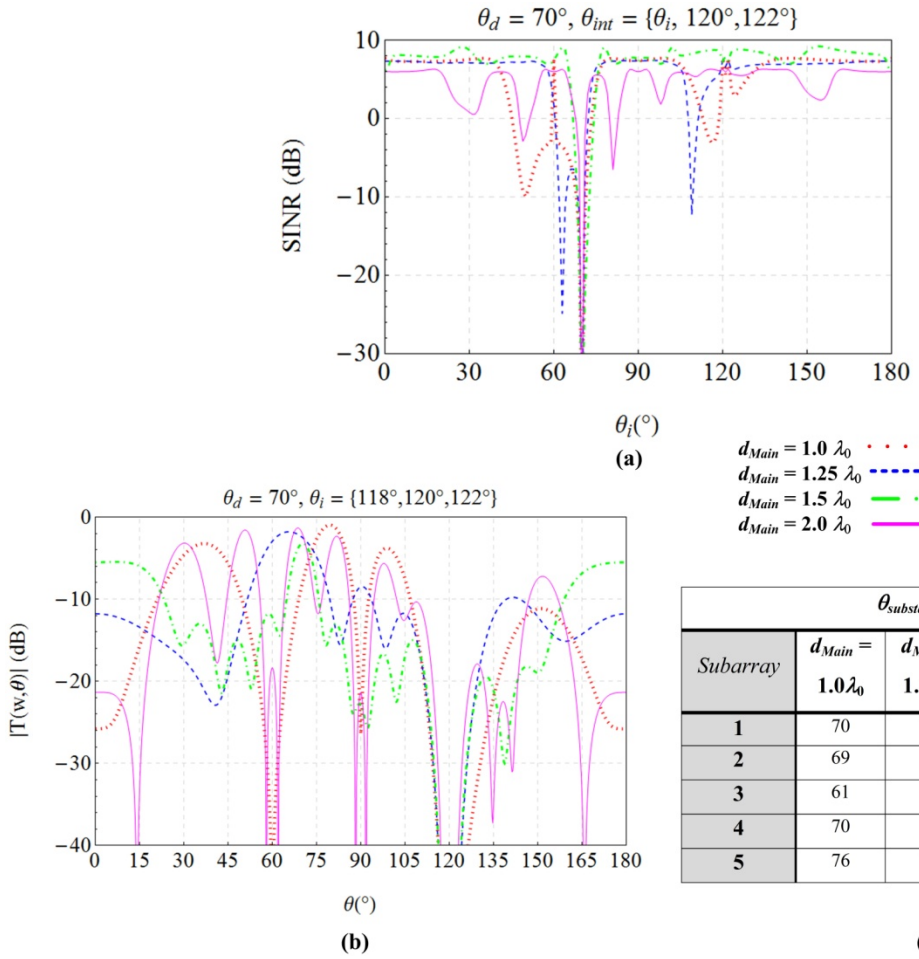

	$\theta_{substeer}$ (°)			
Subarray	d_{Main} = **1.0**λ_0	d_{Main} = **1.25**λ_0	d_{Main} = **1.5**λ_0	d_{Main} = **2.0**λ_0
1	70	135	55	60
2	69	72	62	135
3	61	45	53	66
4	70	77	69	74
5	76	106	59	53

Figure 7-7: SINR (dB) in (a), radiation pattern with θ_i = 118° in (b) and $\theta_{substeer}$ table in (c) comparing adaptive array performance vs. subarray element spacing. In this scenario d_{Main} = {1.0λ_0, 1.25λ_0, 1.5λ_0, and 2.0λ_0}, the other parameters encompass 5-element model RCFGs, θ_d = 70° and θ_{int} = {θ_i, 120°, and 122°}. The results utilize the weight constraint Case 2—the complex conjugate case.

configuration scheme used previously; each curve and table listing applies to a particular d_{Main} value.

Figure 7-7(a) demonstrates the variability in the SINR results for different subarray spacings. Interestingly, a spacing of 1.5λ_0 provides the best overall performance with close-to-maximum SINR levels across the spatial range apart from the standard null. While d_{Main} at 1.0λ_0 and 1.25λ_0 display fewer regions of lower dB level null activity, d_{Main} at 2.0λ_0 exhibits more regions of higher dB null activity. With θ_i = 118°, the interference configuration becomes a small clustered group; the LMS algorithm

handles these nulls well, as indicated in the pattern results of Figure 7-7(b) for all element spacings. The difference, which in turn affects the SINR, lies in the ability of each spacing case to line up the main beam maximum along the desired signal direction. For example, when $d_{Main} = 1.0\lambda_0$, the routine does a poor job of lining up the main beam at 70°. As a result poor, SINR performance occurs near $\theta_i = 118°$. Similarly, the $\theta_{substeer}$ values in Figure 7-7(c) show the varying nature for each d_{Main} considered. When $d_{Main} = 1.0\lambda_0$ and $1.5\lambda_0$, the required beamsteering angles do not vary much from their respective mean, while those of $1.25\lambda_0$ and $2.0\lambda_0$ vary more from their respective means.

7.2.6 Summary

This section illustrates adaptive array performance using the LMS technique under the different weight constraints for several different scenarios. Utilizing the constrained cases allows for further implementation of the pattern reconfigurable antenna model, while the unconstrained case serves as a comparison. The different scenarios entailed variations of one or more parameter while keeping the others constant. In this way, inferences (or general trends) can be made about the behavior of combinations not considered; it is not feasible to analyze every parameter combination. Nevertheless, the SINR and radiation pattern plots along with the beamsteer table allow for comparison and contrast between the varying parameters. The results for each scenario can be summarized as follows.

- Scenario 1: Highlights overall LMS performance per weight constraint case and serves as a basis for comparison of future scenarios.
    - Desired signal falls within the beamsteer range constraint case.
    - As a result, for a small cluster of interferers, the constraint cases exhibit identical performance.
    - Tradeoffs result in SINR performance when implementing the constrained cases instead of the unconstrained cases.
- Scenario 2: Direct comparison with the first scenario; this time the desired signal falls outside the beamsteer range constraint.

- Compared to imposing only complex conjugate constraints (Case 2), SINR results do not contrast much.
- Differences, however, can arise in the specified beam tilts for the pattern.
  - In general, the beamsteer constraint tries to match the results of Case 2.
  - It compensates by varying its own beam tilt parameters within the specification to obtain similar performance when Case 2 places the beamtilts outside the constraint region.

- Scenario 3: Evaluates when multiple interferers impinge on the adaptive array in a widespread formation (in contrast to a clustered group).
  - Results demonstrate better SINR output for a clustered group
  - It is more difficult for the LMS algorithm to meet maximum performance when trying to null out static interferers spread relatively far apart.
- Scenario 4: Evaluates SINR output versus an increasing number of subarray elements for a large number of interferers.
  - Results show that, in either a spatially spread or clustered section interference configuration, each additional subarray element improves SINR levels.
  - Improvements toward maximum levels increasingly diminish for an increasing number of elements over a particular threshold, which depends on the number of interference signals.
- Scenario 5: Evaluates performance effects versus various distances between model RCFG elements.
  - Output results for SINR, pattern, and associated beamsteer angles differ for separations ranging from $1.0\lambda_0$ to $2.0\lambda_0$.
  - Results for one particular spacing ($1.5\lambda_0$) provides better performance overall compared to the rest with close-to-maximum SINR levels.
  - The cause for this occurrence depends on the signal environmental, indicating that further optimization analysis is necessary to determine the best-case spacing.

7.3 Elements of Reconfigurability

The previous section illustrated, by way of a variety of scenarios, adaptive array performance using the LMS technique under different weight constraints. Among the other metrics, the total radiation pattern was one way to gauge performance. Since the goal of this work is to specify the type of element reconfigurability necessary, this section presents the individual model reconfigurable element patterns composing the full array. In other words, it evaluates what kind of pattern reconfigurability necessitates the functionality demonstrated in the previous section that utilized the subarray model.

Similarly to the presentation in Section 7.2, this section details results pertaining to several example signal environment scenarios, each in its own subsection. The analysis is set up such that the parameters related to the signal environment (e.g., θ_d, and θ_{int}) will vary and the array geometry will remain static. Changes due to geometry can be inferred from the results in Section 7.2. Therefore, in the upcoming subsections, the array is composed of $N/2 = 5$ RCFG elements, each spaced a distance $d_{Main} = 1.0\lambda_0$ apart. As before, the LMS technique utilizes the complex conjugate weight constraint case, i.e., Case 2. Each scenario will display a polar plot containing the individual model RCFG element patterns and a table with information regarding their associated beam tilts, pattern null, and phase data.

Before proceeding, a description on the general phase characteristics of each model RCFG element is in order. Due to the nature of the subarray being used to model the pattern reconfigurable element, the phase lies exactly at either 0° and 180° with a jump discontinuity at a value between them, defined as θ_{phase}. This characteristic resembles a shifted unit step function; the following expressions define it more explicitly:

$$\angle T_{sub}^{+}(\theta) = \begin{cases} 0° & \theta < \theta_{phase} \\ 180° & \theta \geq \theta_{phase} \end{cases} \tag{6.11}$$

and

$$\angle T_{sub}^{-}(\theta) = \begin{cases} 180° & \theta < \theta_{phase} \\ 0° & \theta \geq \theta_{phase} \end{cases}. \tag{6.12}$$

The expressions are defined over the spatial observation range (i.e., $0° \leq \theta \leq 180°$) and essentially state that in $\angle T_{sub}^{+}(\theta)$ the phase starts out at 0° and jumps to 180° at θ = θ_{phase}. While in $\angle T_{sub}^{-}(\theta)$, the opposite happens. A discussion on the implications on this type of phase behavior will be addressed at the conclusion of this section.

7.3.1 Signal Environment 1

In this scenario, a signal environment composed of multiple interference signals clustered together, let θ_d = 45° and θ_{int} = {118°, 120°, and 122°}. Figure 7-8 details the LMS results. Figure 7-8(a) shows the magnitude of the radiation pattern of each model RCFG element in polar form. The quantities are represented in dB, and thus the importance lies not in the absolute values of the patterns but their values relative to each other. Also note how the polar plot displays the patterns only from 0° to 180°. This display style is predicated on practical antennas in the adaptive array being planar in nature, backed by a ground plane. It is anticipated that the full array resides on a platform that renders backplane radiation to negligible amounts. For comparison, the thin light gray curve shows the total pattern of the array.

The table in Figure 7-8(b) captures supplementary information pertaining to each model RCFG element. The last three columns detail for each RCFG element the beam tilt angle $\theta_{substeer}$, the location of the null in the pattern (θ_{null}), and which phase function it adheres to, respectively. The phase characteristics can take on either one of the functions described by (6.11) and (6.12). In either case, the column also tabulates the theta value in which the phase changes, described by θ_{phase}.

The results of Figure 7-8 present some interesting findings for this scenario. As noted in the beam tilt column, $\theta_{substeer}$ for certain RCFG elements strays farther away from θ_d compared to others—an occurrence seen previously in Section 7.2. Here the individual subarray plots put this into perspective. Along the desired signal direction, the

relative value of $|T_{sub}(\theta)|$ varies for each RCFG element. The values of $|T_{sub}(\theta_d)|$ for RCFG elements 1, 2, and 3 dominate compared to RCFG elements 4 and 5. On the other hand, the nulls of each subarray pattern tend to congregate around each other. As a matter of fact, they congregate near the location of the interference signals; this is an interesting result, which indicates that the LMS algorithm is directing the nulls of individual model pattern reconfigurable elements in the direction of the interference. This in turns places the expected null region in the total pattern as shown. Note also how the point of phase change (given by θ_{phase}) matches the spatial location of the pattern null for each RCFG element.

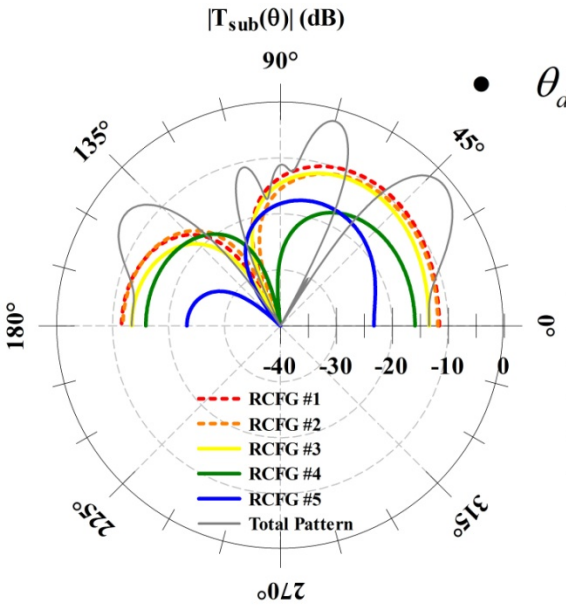

(a)

- $\theta_d = 45°, \theta_{int} = \{118°, 120°, 122°\}$

RCFG #	$\theta_{substeer}$ (°)	θ_{null} (°)	Phase function, θ_{phase} (°)
1	55	115	$\angle T^{+}_{sub}(\theta)$, 116
2	51	111	$\angle T^{+}_{sub}(\theta)$, 112
3	57	117	$\angle T^{-}_{sub}(\theta)$, 118
4	33	100	$\angle T^{-}_{sub}(\theta)$, 100
5	71	132	$\angle T^{+}_{sub}(\theta)$, 133

(b)

Figure 7-8: Model pattern reconfigurable characteristics as a result of signal environment 1 in which θ_d = 45° and θ_{int} = {118°, 120°, and 122°}. In (a) the radiation pattern of each subarray element is displayed with the total pattern (thin light gray curve), while (b) tabulates each element's beam tilt, pattern null, and phase information. The results give insight into the candidate patterns necessary for pattern reconfigurability.

7.3.2 Signal Environment 2

Here, the interference environment stays the same, i.e., θ_{int} = {118°, 120°, and 122°}, but the desired signal changes its arrival angle, θ_d = 75°. Figure 7-9 details the results in the same dual-graphic configuration. Even with a change in the desired signal

direction, the results in Figure 7-9(a) and Figure 7-9(b) emulate those in Figure 7-8. Along θ_d, RCFG elements 3, 4, and 5 this time have more dominate $\left|T_{sub}\left(\theta_d\right)\right|$ values compared to elements 1 and 2. Similarly, the nulls of the each RCFG element once again group about the θ_{int} region, overlaying the null region of the total pattern. The point of phase change follows accordingly, as indicated in the table, and as before the routine chooses the phase function, either $\angle T_{sub}^{+}\left(\theta\right)$ or $\angle T_{sub}^{-}\left(\theta\right)$, that provides the best fit to satisfy the signal environment requirements.

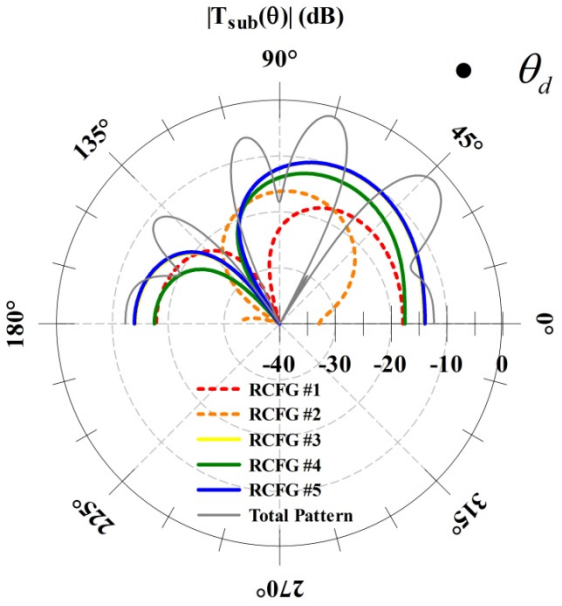

(a)

- $\theta_d = 75°, \theta_{int} = \{118°, 120°, 122°\}$

RCFG #	$\theta_{substeer}$ (°)	θ_{null} (°)	Phase function, θ_{phase} (°)
1	47	109	$\angle T_{sub}^{+}(\theta)$, 109
2	85	155	$\angle T_{sub}^{-}(\theta)$, 155
3	64	124	$\angle T_{sub}^{-}(\theta)$, 125
4	68	129	$\angle T_{sub}^{+}(\theta)$, 130
5	64	124	$\angle T_{sub}^{+}(\theta)$, 125

(b)

Figure 7-9: Model pattern reconfigurable characteristics as a result of signal environment 2 in which θ_d = 75° and θ_{int} = {118°, 120°, and 122°}. In (a) the radiation pattern of each subarray element is displayed with the total pattern (thin light gray curve), while (b) tabulates each element's beam tilt, pattern null, and phase information. The results emulate those in the previous scenario.

Comparing the magnitudes of the subarray patterns and the total pattern reveals that more information is needed in order to match the two. For example, consider a null occurrence in the total pattern. The polar plot dictates one occurrence in the interference region and another at θ = 60°. Gauging from the RCFG plots, it is apparent that the collection of nulls in each subarray near the interference region leads to a null in the overall pattern. Such is not the case for the null at θ = 60°; here the value of

$\left|T_{sub}\left(\theta = 60°\right)\right|$ varies per RCFG element. At first glance, this makes unclear the source of the total pattern null. To comprehend the reason for the null requires knowledge of the pattern phase of each RCFG element and the phase contribution due to the element spacing. At this spatial angle, deconstructive interference of the signals causes the null to occur.

7.3.3 Signal Environment 3

In this scenario, let θ_d = 110° and θ_{int} = {80°, and 140°}; this is still a multiple interference signal environment, but the two interferers are spread around the desired signal's angle of arrival (i.e., $\theta_{int} = \theta_d \pm$ 30°). Assessing the results from the analysis in subsection 7.2.3, lower performance is anticipated compared to a clustered group of interference signals. Figure 7-10 displays the results for this scenario, showing the effects on the available pattern reconfigurability.

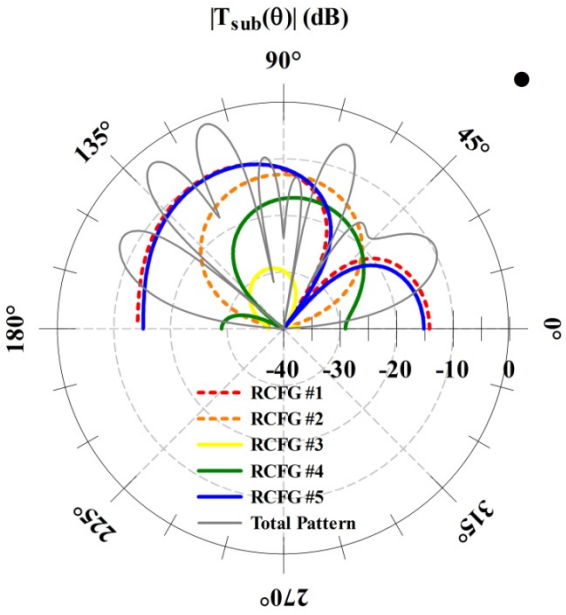

- $\theta_d = 110°, \theta_{int} = \{80°, 140°\}$

RCFG #	$\theta_{substeer}$ (°)	θ_{null} (°)	Phase function, θ_{phase} (°)
1	115	54	$\angle T_{sub}^{-}(\theta)$, 55
2	91	11	$\angle T_{sub}^{+}(\theta)$, 11
3	105	42	$\angle T_{sub}^{-}(\theta)$, 42
4	81	148	$\angle T_{sub}^{+}(\theta)$, 148
5	112	51	$\angle T_{sub}^{+}(\theta)$, 52

(b)

Figure 7-10: Model pattern reconfigurable characteristics as a result of signal environment 3 in which θ_d = 110° and θ_{int} = {80° and 140°}. In (a) the radiation pattern of each subarray element is displayed along with the total pattern (thin light gray curve), while (b) tabulates each element's beam tilt, pattern null, and phase information. In this case, the interferers are spread around the desired signal's arrival angle, and thus the results differ from the previous signal environment scenarios.

Due to the interferers being spread out, the results of this scenario differ compared to the previous scenarios in subsections 7.3.1 and 7.3.2. In this case, the nulls of the individual RCFG elements are spread out over the spatial range. Thus, the LMS technique chooses the RCFG patterns in a way such that deconstructive interference places nulls in the total pattern. This is indeed an interesting result. Since each RCFG element only has one pattern null available, the optimization routine cannot place all their nulls near a single interferer because two of them impinge on the array spread apart from each other. Instead, the routine utilizes the magnitude and phase of the pattern along with the spatial phasing to null out the interference.

7.3.4 Signal Environment 4

The last scenario demonstrates the effects on the available pattern reconfigurability when the interference signal comes close to the desired signal. Let the parameters of this signal environment correspond similarly with those in signal environment 3, i.e., $\theta_d = 75°$ and $\theta_{int} = \{80°, \text{and } 82°\}$ (the desired signal being 5° away from θ_{int}). Recall that subsection 7.2.2 highlighted a similar scenario; Figure 7-11 shows the effect on each RCFG element pattern in this scenario.

As expected, due to the close proximity of the desired signal with the interference, a main beam maximum cannot be established in the total pattern curve along θ_d in Figure 7-11(a). This occurs in spite of the $\theta_{substeer}$ of RCFG elements 2 to 5 attempting to align their main beams along the desired signal direction. Nulling out the interference takes precedence, and in turn SINR performance suffers. Additionally, the characteristics of this scenario cause θ_{null} to align themselves far from the θ_{int} region for those same RCFG elements (2 to 5). As a matter of fact, their nulls range from $120° \le \theta \le 143°$ without an emerging null in the array pattern. This is a consequence of the main beam maximum of RCFG 1 being directed toward θ = 136° and having sufficient magnitude to prevent a total pattern null from occurring. Essentially, the results of this subsection demonstrate the effects on the type of element reconfigurability when the desired and interference signals are within close proximity of each other.

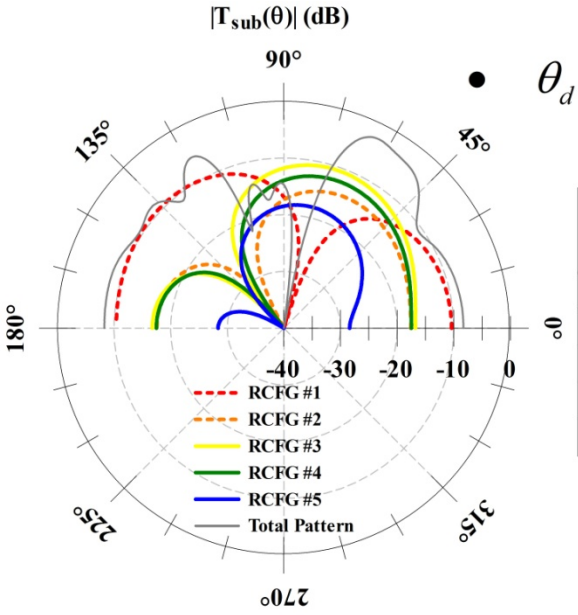

(a)

- $\theta_d = 75°, \theta_{int} = \{80°, 82°\}$

RCFG #	$\theta_{substeer}$ (°)	θ_{null} (°)	Phase function, θ_{phase} (°)
1	136	74	$\angle T^{+}_{sub}(\theta)$, 74
2	60	120	$\angle T^{+}_{sub}(\theta)$, 121
3	71	132	$\angle T^{-}_{sub}(\theta)$, 133
4	68	129	$\angle T^{+}_{sub}(\theta)$, 129
5	78	143	$\angle T^{-}_{sub}(\theta)$, 144

(b)

Figure 7-11: Model pattern reconfigurable characteristics resulting from signal environment 4 in which θ_d = 75° and θ_{int} = {80° and 82°}. In (a) the radiation pattern of each subarray element is displayed along with the total pattern (thin light gray curve), while (b) tabulates each element's beam tilt, pattern null, and phase information. In this case, the interferers are close to the desired signal's arrival angle. Close proximity of both signal types causes degradation in main beam performance of the total pattern and misalignment of the RCFG nulls with the interference region.

7.3.5 Discussion

One of the main objectives of this research includes specifying what requirements in the element design are necessary for pattern reconfigurable antennas to have an impact utilizing the adaptive array platform. The main characteristic centered on the element pattern's beam tilt, i.e., its beamsteering capability. Thus, it was initially desired to let the LMS algorithm find the optimal set of beam tilts in the array using the subarray model. In terms of the type of reconfigurability needed, the results of this section instead indicate that what is needed in pattern reconfigurable element design is a reconfigurable null and not necessarily a reconfigurable beam tilt. This concept of null reconfigurability is exactly what Chapter 5 illustrated using adaptive array scenarios to determine the pattern reconfigurable solutions.

As demonstrated in signal environment 1 and 2, the LMS selects the optimal scenario by steering the nulls of the model RCFG elements into or near the interference

region. When this happens, the interference signals are mitigated directly by the reconfigurable element pattern nulls, instead of being mitigated by the array, which utilizes the principle of deconstructive interference. The latter can be more difficult to accomplish in concert with the adaptive array hardware and may lead to fewer degrees of freedom, i.e., opportunities to formulate the null(s) over an adaptive array span.

Also note that in all of the signal environment scenarios presented, the main beam magnitudes of each subarray vary along the desired signal direction. In some instances, only two or three of the five elements have appreciable magnitudes that contribute to the main beam of the total pattern. This of course exactly happens with the appropriate phasing; in this case, the principles of constructive interference apply. Referring back to a topic discussed in Section 5.3, a greater emphasis should be put on nulling out the interference because it has a greater impact on SINR performance due to the fact that the interference effect is in the denominator of the SINR relationship. In practice, the accompanying system hardware tracks the desired signal; it can be expected that the amplitude of the signal stays relatively constant since its origins are known. On the other hand, interference signals are unknown in origin, leaving the possibility of them impinging on the adaptive array at very high amplitudes. Even with higher amplitudes, a collection of nulls in the element patterns steered toward the interference can provide the warranted mitigation.

Overall, the findings signify what kind of pattern reconfigurability is necessary to obtain the functionality offered by small adaptive array systems. The results illustrated the assorted pattern types for the various signal environments, patterns which fall within plausible bounds of what a single, planar, practical pattern reconfigurable antenna can provide: one main lobe region and a few nulls (or pattern depressions). Recall that the phase profile for each element exhibited a discontinuous jump point; in reality, this in an impractical development. Even though it would be difficult for a practical pattern reconfigurable antenna to obtain such phase characteristics, the magnitude and phase profiles provide antenna designers a goal in order realize the performance benefits reconfigurable adaptive arrays offer.

CHAPTER 8
CONCLUSION

8.1 Summary

This dissertation assesses the functional benefits of utilizing radiation reconfigurable antennas in an adaptive array setting, ultimately specifying the requirements the element design must meet in order to improve adaptive array performance.

The dissertation focused on arrays composed of a small number of relatively widely spaced elements. Such array configurations (1) mitigate the effects of mutual coupling between reconfigurable elements, thereby maximizing their individual performance potential, and (2) establish a platform for applications seeking portability and a small-scale system package as a design priority. The work extends beyond the techniques of R.T. Compton Jr. and others to demonstrate how radiation reconfigurable antennas with beam tilting capability affect adaptive array performance. Using ideal element patterns as a basis for comparison, the methodology incorporates more relevant reconfigurable antenna patterns. A diverse set of illustrations shows the resulting effects, mainly using the SINR performance index. Consequently, the analysis also sheds light on the limitations of this particular technique, specifically the requirement of constraining the additional reconfigurable element on the basis of the original set of elements in the array. The dissertation then pursued ways to overcome these limitations by fully leveraging the capabilities of the available pattern reconfigurability.

Using a systematic approach, the work integrates pattern variability directly into two different optimization routines, the convex and least mean square (LMS) algorithms. Instead of finding reconfigurable solutions by means of solutions based on *a priori* information, the present methodology uses the algorithm itself to determine the range of possible solutions. The framework behind this realization stemmed from (1) developing a pattern reconfigurable element model using isotropic radiators in a two-element subarray

topology and (2) integrating the model in the optimization routine with the appropriate element weight constraints.

While a great deal of insight was gained through implementation of the convex optimization routine, it over-constrained the problem, leading to less-than-satisfactory results. The LMS technique, on the other hand, provided satisfactory results. Utilizing the technique under the prescribed weight constraints, a number of adaptive array scenarios utilizing the LMS approach were evaluated. Each scenario varied a number of parameters related to the signal environment and the array geometry. The results demonstrate the tradeoffs that arise in terms of SINR and pattern performance and give the designer details on what to expect in each particular situation.

Drawing on these findings, the work goes into further depth and evaluates what kind of pattern reconfigurability is necessary to obtain the functionality displayed when utilizing the subarray model. In this case, however, the optimization routine leverages all the available pattern reconfigurability when selecting the element patterns. The displayed pattern profiles (patterns that fall within the capabilities of a single, planar, practical pattern reconfigurable antenna) give reconfigurable antenna designers optimum criteria that will realize the performance benefits reconfigurable adaptive arrays offer. The results point to the importance of having null reconfigurability in the element design. That is, a designer should aim for elements with null steering capabilities and not necessarily beam steering capabilities.

The implications of null reconfigurability can have a substantial impact in the implementation of future cognitive radio systems. As reported in [34], research in cognitive radio aims to develop efficient wireless communication strategies to make use of the unused allocated spectrum (e.g., white space). The challenge for antenna engineers lies in designing antennas that can learn, adapt, or reconfigure themselves (i.e., possess the elements of cognition and reconfigurability). Since sensing and detecting the RF environment is a crucial system requirement, being able to dynamically reconfigure the null of the antenna array can mitigate interference from signals that are not of interest.

8.2 Research Contributions

This dissertation research has made the following contributions:

- Investigated the utility of incorporating radiation reconfigurable antennas in an adaptive array setting.
- Established a platform for applications seeking portable system designs containing a small number of antenna elements spaced with relatively wide element spacing, thereby reducing the effects of mutual coupling and allowing additional space between array elements for supplementary RF electronics.
- Extended the early work of R.T. Compton Jr. and others in adaptive arrays by going beyond utilizing ideal, traditional, fixed-pattern antenna element patterns.
- Employed the procedures of Compton's work and assimilated element patterns more relevant to pattern reconfigurable antennas, demonstrating that a practical pattern reconfigurable element can produce results comparable to that of the ideal element (e.g., maintain good adaptive array performance and mitigate grating nulls).
- Ascertained the limitations in terms of the available solution space for this particular methodology in conjunction with pattern variability, a factor introduced by Compton's approach but not fully utilizing the available reconfigurability.
- Integrated pattern variability directly into an optimization routine, a more systematic approach that allows the algorithm to fully leverage the capabilities of the available reconfigurability and determine the range of possible solutions.
- Developed a pattern reconfigurable element model based on a two-element subarray topology in conjunction with appropriate element weight constraints.
- Established a pathway specifying the design requirements for pattern reconfigurable antennas to improve small adaptive array performance, demonstrating that designers should focus on an element's null steering capability rather than its beam tilting capacity.

8.3 Future Work

At the conclusion of this dissertation, many directions for further improvement and development present themselves. The following topics provide potential short-term and long-term directions for future work.

Additional elements in the pattern RCFG model The content of Subsection 6.2.2 briefly discussed the advantages and disadvantages of increasing the number of antenna elements in the subarray model. One such effect pertained to the additional nulls that occur in the subarray pattern. In light of this work's most recent developments, it is worth investigating the improvements in adaptive array performance for impinging interference signals spread out in the spatial range. It was determined that performance degrades when this scenario takes place. Giving the optimization routine more nulls to choose from in the subarray model could better mitigate widely spaced interferers. As mentioned, the subarray has a well-defined mainbeam and null(s) when the amplitudes are identical and the element phasing is progressive. The difficulty lies in determining a weight constraint in conjunction with an optimization routine to incorporate the mulit-element subarray model while at the same time not overstepping the bounds of practical pattern reconfigurability. Realizing these conditions would be beneficial, but at the same time, challenging task.

Subarray element model refinement The isotropic elements utilized in the subarray model dictate the patterns of each model pattern reconfigurable antenna. Placing the two elements in an array setting gives the pattern more defined pattern characteristics. Future work should look into further refining this model by incorporating windowing-type element factors into the optimization routine, that is, element factors that would be applied to each isotropic element (e.g., the model dipole element used earlier in this work). This approach may produce model patterns better suited for practical pattern reconfigurable element design. The flexibility of the optimization routines allows for implementation of this feature.

Quantifying the proximity effect between impinging signals on the array The contents of the analysis presented in Section 7.2 showed the effect on the SINR whenever the interference signal comes into close angular proximity to the desired signal. This effect results in a degradation of SINR performance. Future work should investigate quantitatively the tolerance and sensitivity of this effect, detailing the impact on the other performance metrics (e.g., array main beam alignment with the desired signal or the individual element patterns themselves). If the adaptive array system has this sort of information at its disposal, it may be able to readjust to a different configuration when realizing a particular signal environment.

Weighing the tradeoffs between null depth and null beamwidth This dissertation demonstrated the importance of a pattern reconfigurable antenna's ability to steer its null, a design requirement necessary to increase small adaptive array performance. The results in Section 7.3 detail this effect by showing how the optimal LMS solution places the null of each individual pattern RCFG element in the vicinity of the interference signal. Future work should investigate what additional benefits ensue when the interference signals arrive at large angles (e.g., angles of arrival between 10° and 45°) with respect to the incoming desired signal direction.

When this scenario presents itself, adaptive array performance can be enhanced by reducing pattern gain over a spatially wide interference region at the expense of the null depth. In other words, tradeoffs between null depth and null beamwidth should be analyzed. With the null depth relaxed to a certain performance constraint, the individual antenna elements may be able to have a wider pattern depression region to handle a larger spread of interferers. These factors should be incorporated into the optimization analysis with the performance constraint and the resulting outcome being probabilistic in nature. This approach will weigh the tradeoffs accordingly; the results can very well add another element to pattern reconfigurable antenna design.

Potential application to other synthesis techniques The pattern reconfigurable model utilized in this work has the potential to extend beyond the adaptive array platform. There exist a number of classical periodic phased array synthesis techniques that aim to meet a specified array pattern goal (e.g., sidelobe level, main beamwidth, null placement, etc.). Traditionally, the elements of choice in the analysis are isotropic, and the results return the necessary weights required to meet the desired characteristics. With the element weights being the unknown quantity of interest, the pattern reconfigurability model can be applied in a similar fashion. The added component of pattern variability may increase the functionality of the synthesis methods (e.g., being able to reconfigure to multiple pattern goals). Tradeoffs in performance will ensue compared to the static case due to weight constraints, but the task is worth pursuing; it could very well demonstrate another benefit of antenna pattern reconfigurability.

Pattern association to a set of signal environments Consider the results from any one of the signal environment scenarios in Section 7.3. Given that the set of reconfigurable antennas in the array can provide the specified pattern characteristics for each element, then, when connected to the beamformer, the adaptive weights would only require a uniform distribution in amplitude. As the signal environment changes, the system adapts and, thus, the optimal element patterns change. Future work should consider a collection of patterns that works best for an assortment of scenarios and weigh the tradeoffs between performance and the range of patterns a reconfigurable antenna can provide (e.g., a continuous versus discrete beam/null tilt range). Exchanges between the applied element weights and the magnitude and phase of the patterns can be utilized as an additional working degree of freedom.

The analysis could eventually progress to providing insight into questions regarding fault and failure effects. For example, what happens when one or more elements become dysfunctional? Since the remaining antenna elements have the means for pattern reconfigurability, can they compensate for the failed elements and maintain performance to a limited degree? Questions along these lines will address practical system-level concerns such as sensitivity and robustness.

Association with adaptive array systems This work aims to improve adaptive array functionally at the front end, i.e., the antenna array. Apart from the antenna array, a complete adaptive array system encompasses various other hardware components involving detection and estimation, gain and phase adjustment, feedback and control circuitry, etc. From a much broader perspective, future work should investigate the means of imbedding a pattern reconfigurable antenna array in such a system. As mentioned in the beginning of the dissertation, Section 2.1, a majority of pattern reconfigurable antennas utilize switching devices that allow for the available reconfigurability. The adaptive system must know what kind of reconfigurability it has available at its disposal and how to control it. Thus, a separate control system should be devised for the pattern reconfigurable elements that work hand in hand with the adaptive feedback and control system.

A step in that direction might include creating a mini-adaptive array experiment that comprises a small pattern reconfigurable antenna array with a switching network to control the pattern variability. The array would be situated in an adaptive array scenario wherein the signal environment includes a moving jammer and/or static desired signal. Previous work (e.g., [17,35]) reports on adaptive array measurements, thus providing some schemes and direction for implementation.

Optimizing element spacing for aperiodic array applications The method presented in this work concentrates on reconfigurable antenna array elements that are periodically spaced, with a fixed element distance analyzed in the optimization. The convex and LMS algorithms determined the best possible solution for the given adaptive array scenario based upon that distance. Future work should investigate any additional performance benefits when the individual element spacing between pattern reconfigurable elements is allowed to vary and thus create an aperiodic array. Since it is not feasible to reconfigure physical distance on the fly, a set configuration may work better for a select group of scenarios. As mentioned in [22], various methods can be utilized in the analysis, including particle swarm optimization. Even if the analysis

indicates increased performance in certain circumstances, tradeoffs must be weighed due to the added complexity in implementation.

LMS comparison and array reconfiguration response time This work utilizes the convex and LMS optimization routines in conjunction with the RCFG models to choose the optimal set of reconfigurable patterns associated with each antenna element in the array for a given adaptive array scenario. On one hand, the LMS technique is a gradient-based algorithm, which seeks out the minimum of the performance surface. In particular, the algorithm applies the method of steepest descent to the minimum square error performance measure to obtain a simple implementation that is well suited to continuous signal communication systems. The LMS algorithm contrasts to other algorithms that are applied to pulsed radar and sonar systems to deal with clutter and interference rejection (e.g., Howells-Applebaum adaptive processor) [18].

The results demonstrate the advantages of using LMS and its ease of implementation from an analytical point view. However, disadvantages may arise from a system-level perspective when compared to other classes of adaptation algorithms. Each has different performance characteristics that are of critical importance because the algorithm influences the speed of array reconfiguration and the complexity of the circuitry required in hardware implementation [18]. In terms on implementation, these hardware components include down converters, analog-to-digital converters, and the digital processing unit (e.g., field programmable gate arrays and a central processing unit).

Even though this dissertation focuses on the adaptive array steady-state response, another important factor worth mentioning for future work is in the system's transient behavior. For example, during a weight transient, the weight vector in an LMS algorithm is a sum of exponentials. The time constant in the argument of these exponentials depends on the eigenvalues of the covariance matrix. Thus, changes in the eigenvalues cause the array response speed to vary, and convergence speed is degraded as a result. Advanced weight control techniques exist to increase the convergence rate by reducing the eigenvalue spread. One particular version is the recursive least squares algorithm

(RLS) [17]. Despite the fact that the RLS has a faster convergence rate compared to LMS, it requires more computations. In FPGA implementation, the circuit scale and complexity increase along with the computational load, which eventually results in a lower maximum operating frequency due to the increase in overall circuit size [36]. Furthermore, it has been discussed in [37] that the eigenvalues not only depend on signal power, the number of incident signals, and the element spacing but also the element patterns. Again, since the element patterns play a role, future work should investigate the benefits that pattern variability can have in increasing the array response speed.

REFERENCES

[1] R. C. Hansen, *Phased Array Antennas*. New York, NY: John Wiley & Sons, 1998.

[2] R. J. Mailloux, *Phased Array Antenna Handbook*, 2nd ed. Boston, MA: Artech House, 2005.

[3] W. H. Kummer, "Basic array theory," *Proceedings of the IEEE*, vol. 80, no. 1, pp. 127-140, Jan. 1992.

[4] H. L. Van Trees, *Optimum Array Processing: Part IV of Detection, Estimation, and Modulation Theory*. New York, NY: John Wiley & Sons, 2002.

[5] R. J. Mailloux, "Guest editorial: Special issue on phased arrays," *IEEE Trans. Antennas Propag.*, vol. 47, no. 3, pp. 413-415, Mar. 1999.

[6] J. A. Allen, "Array radars: A survey of their potential and their limitations," *Microw. J.*, vol. v, no. 5, pp. 67-79, May 1962.

[7] L. C. Godara, "Applications of antenna arrays to mobile communications, part I," *Proceedings of the IEEE*, vol. 85, no. 7, pp. 1033-1060, Jul. 1997.

[8] L. C. Godara, "Applications of antenna arrays to mobile communications, part II," *Proceedings of the IEEE*, vol. 85, no. 8, pp. 1195-1245, Aug. 1997.

[9] J. T. Bernhard, *Reconfigurable Antennas*, 1st ed. San Rafael, CA: Morgan & Claypool Publishers, 2007.

[10] J. C. Chiao et al., "MEMS reconfigurable antennas," *Int. J. RF Microw. Comput. Aided Eng.*, vol. 11, no. 5, pp. 301-309, Sep. 2001.

[11] K. Hieptas, "Beam steering in phased arrrays using a pattern reconfigurable antenna," M.S. thesis, University of Illinois at Urbana-Champaign, 2004.

[12] S. Zhang, G. H. Huff, J. Feng, and J. T. Bernhard, "A pattern reconfigurable microstrip parastic array," *IEEE Trans. Antennas Propag.*, vol. 52, pp. 2773-2776, Oct. 2004.

[13] S. Zhang, G. H. Huff, and J. T. Bernhard, "Three variations of a pattern-

reconfigurable microstrip parasitic array," *Microw. Optical Technology Lett.*, vol. 45, no. 5, pp. 369-372, Jun. 2005.

[14] G. H. Huff and J. T. Bernhard, "Integration of packaged RF MEMS switches with radiation pattern reconfigurable square spiral microstrip antennas," *IEEE Trans. Antennas Propag.*, vol. 54, pp. 464-469, Feb. 2006.

[15] Special issue on active and adaptive antennas, *IEEE Trans. Antennas Propag.*, vol. AP-12, no. 2, Mar. 1964.

[16] Special issue on adaptive antennas, *IEEE Trans. Antennas Propag.*, vol. AP-24, no. 5, Mar. 1976.

[17] R. T. Compton Jr., *Adaptive Arrays, Concepts and Performance*. Englewood Cliffs, NJ: Prentice-Hall, 1988.

[18] R. A. Monzingo and T. W. Miller, *Introduction to Adaptive Arrays*. New York, NY: John Wiley & Sons Inc., 1980.

[19] D. S. Albert. (2000, Feb.) US Army War College. [Online]. Available: http://www.carlisle.army.mil/DIME/documents/Alberts_NCW.pdf

[20] R. T. Compton Jr., "A method of choosing element patterns in an adaptive array," *IEEE Trans. Antennas Propag.*, vol. 30, pp. 489-493, May 1982.

[21] A. Ishide and R. T. Compton Jr., "On grating nulls in adaptive arrays," *IEEE Trans. Antennas Propag.*, vol. 28, pp. 467-475, Jul. 1980.

[22] P. J. Bevelacqua and C. A. Balanis, "Minimum sidelobe levels for linear arrays," *IEEE Trans. Antennas Propag.*, vol. 55, pp. 3442-3449, Dec. 2007.

[23] P. J. Bevelacqua, "The utility of convex optimization for weight selection in arrays," in *Proc. IEEE AP-S Int. Symp.*, 2009, pp. 1-4.

[24] G. H. Huff and J. T. Bernhard, "Analysis of a radiation and frequency reconfigurable microstrip antennas," in *Proc. 2004 Antenna App. Symp.*, Monticello, IL, 2004, pp. 175-191.

[25] C. A. Balanis, *Antenna Theory: Analysis and Design*, 2nd ed. New York, NY: John Wiley & Sons, 1997.

[26] Ansoft Corporation, Pittsburgh, PA. Ansoft HFSS, Version 10.3.

[27] D. Psychoudakis, C.-C. Chen, and J. L. Volakis, "Optimizing wearable UHF antennas for on-body operation," in *Proc. IEEE AP-S Int. Symp.*, 2007, pp. 4184-4187.

[28] G. A. Conway and W. G. Scanlon, "Antennas for over-body-surface communication at 2.45 GHz," *IEEE Trans. Antennas Propag.*, vol. 57, pp. 844-855, Apr. 2009.

[29] W. F. Gabriel, "Adaptive array processing systems," *Proceedings of the IEEE*, vol. 80, no. 1, pp. 152-162, Jan. 1992.

[30] W. F. Gabriel, "Adaptive array--An introduction," *Proceedings of the IEEE*, vol. 64, no. 2, pp. 239-272, Feb. 1976.

[31] The Mathworks, Inc., Natick, MA. Matlab, R2008b.

[32] Y. T. Lo, "Aperiodic arrays," in *Antenna Handbook: Theory, Application, and Design*. New York, NY: Van Nostrand Reinhold Company Inc., 1988, ch. 14, pp. 1-37.

[33] T. L. Roach and J. T. Bernhard, "Tapering in arrays with pattern reconfigurability," *Electromagnetics*, vol. 29, no. 5, pp. 384-392, Jul. 2009.

[34] C. G. Christodoulou. (2010, Jan.) IEEE Antennas and Propagation Society. [Online]. Available: http://ieeeaps.org/pdfs/APSwebsite-Christos.pdf

[35] M. A. Halim, *Adaptive Array Measurements in Communications*. Norwood, MA: Artech House, 2001.

[36] H. Oba, M. Kim, and H. Arai, "FPGA implementation of LMS and N-LMS processor for adaptive array applications," in *Int. Symp. Intelligent Signal Processing and Communication Systems*, Tottori, Japan, 2006, pp. 485-488.

[37] R. T. Compton Jr., "On eigenvalues, SINR, and element patterns in adaptive arrays," *IEEE Trans. Antennas Propag.*, vol. 32, pp. 643-647, Jun. 1984.

AUTHOR'S BIOGRAPHY

Tyrone Lavonne Roach was born in Las Vegas, Nevada, and received his B.S. degree from the University of Nevada-Las Vegas (Magna Cum Laude) in December of 2001 and his M.S. and Ph.D. degrees from the University of Illinois at Urbana-Champaign (UIUC) in 2005 and 2010, respectively, all in Electrical and Computer Engineering (ECE). His current research interests involve antenna array reconfigurability, platform integration of phased array antenna systems with adaptive and multifunctional characteristics, and expanding small array functionality in wireless and smart sensor technology. In 2000 and 2001, he was a summer undergraduate research intern in the ECE departments at the University of Minnesota and the Georgia Institute of Technology, respectively. In the summer of 2004 he was a technical intern with Delphi Research Labs in Shelby Township, Michigan, where he worked on modeling and simulating the electromagnetic characteristics of an outdoor antenna range and antennas mounted on vehicular platforms. While at UIUC, Dr. Roach was the recipient of numerous fellowships, including the Support for Under-Represented Graduate Education (SURGE), Diversifying Faculty in Illinois (DFI), and Vodafone-Illinois Graduate Fellowships. He also was awarded the Raj Mittra Outstanding Research Award in 2010 and nominated for the Olesen Award for excellence in undergraduate instruction, also in 2010 by the ECE department.